Forschungszentrum Karlsruhe
Technik und Umwelt

Wissenschaftliche Berichte
FZKA 6368

The Cosmic Ray Muon Charge Ratio

Measurements and Calculations at Energies Relevant for the Atmospheric Neutrino Anomaly

B. Vulpescu

Institut für Kernphysik

September 1999

FORSCHUNGSZENTURM KARLSRUHE
Technik und Umwelt

Wissenschaftliche Berichte
FZKA 6368

The Cosmic Ray Muon Charge Ratio

Measurements and calculations at energies relevant for the atmospheric neutrino anomaly

Bogdan Vulpescu[1]

Institut für Kernphysik

[1] On leave from National Institute of Physics and Nuclear Engineering – Horia Hulubei, Bucharest, Romania

Forschungszentrum Karlsruhe GmbH, Karlsruhe
1999

Als Manuskript gedruckt

Forschungszentrum Karlsruhe GmbH
Postfach 3640, 76021 Karlsruhe

Mitglied der Hermann von Helmholtz-Gemeinschaft
Deutscher Forschungszentren (HGF)

ISSN 0947-8620

Abstract

The electromagnetic calorimeter set up WILLI, operated in NIPNE-HH Bucharest, has been modified for measurements of the charge ratio in the atmospheric muon flux. The experimental method is based on the observation of the reduced effective lifetime of negative muons, if stopped in matter, as compared to the lifetime of positive muons. The method which gives accurate results and avoids the difficulties and systematic errors of magnetic spectrometers and the technical procedures are studied in detail and demonstrated with developing a compact and flexible measuring device. Aluminium is used as optimal absorber material, being a compromise of maximising the reduction of the lifetime due to nuclear capture and the rate of stopped muons observed by delayed coincidences with the decay electrons. The present studies are focused to an energy range of the muons which provides important information for the discussion of the so-called atmospheric neutrino problem and for studies of the atmospheric neutrino and antineutrino fluxes. The results obtained by two measuring periods are:

$$R(\mu^+/\mu^-) = 1.30 \pm 0.05\,(\text{stat})$$

for muons of 0.86 GeV/c of vertical incidence (mean zenith angle 26^o) and

$$R(\mu^+/\mu^-) = 1.27 \pm 0.01\,(\text{stat})$$

for muons of 0.52 GeV/c of vertical incidence (mean zenith angle 19^o).

For the discussion in context with the information existing in the literature, a comprehensive data basis and survey on the "world knowledge" about muon charge ratio spectra are prepared. These results are compared with results of extensive simulation calculations using the Monte Carlo air shower simulation code CORSIKA. Various hadronic interaction models used as generator for the hadron - air interactions are scrutinised. Serious discrepancies with the model GHEISHA, generally used for calculating low energy interactions, are evidenced. Some reasons for that observation are indicated. Predictions of the VENUS and the FLUKA models are presented for an energy range of primary cosmic rays relevant for the low energy atmospheric muon flux.

Das Ladungsverhältnis der Myonen in der Kosmischen Strahlung; Messungen und theoretische Voraussagen bei Energien relevant für die atmosphärische Neutrino - Anomalie

Das elektromagnetische Kalorimeter WILLI, das im NIPNE-HH Bukarest betrieben wird, wurde geeignet modifiziert, um das Ladungsverhältnis atmosphärischer Myonen messen zu können. Die experimentelle Methode basiert auf der Beobachtung der verringerten effektiven Lebensdauer negativer Myonen, wenn sie in Materie gestoppt werden, im Vergleich zur Lebensdauer positiver Myonen. Die Methode, die genaue Ergebnisse liefert und die Schwierigkeiten und systematische Unsicherheiten magnetischer Spektrometer vermeidet, sowie die experimentelle Technik werden im Detail studiert und demonstriert mit der Vorstellung einer kompakten und flexiblen Apparatur. Als optimaler Absorber hat sich Aluminium erwiesen, als Kompromiß zwischen der Maximierung der Verringerung der effektiven Lebensdauer negativer Myonen durch Kern - Einfang und der Zerfallsrate, die mittels einer verzögerten Koinzidenz mit den Zerfallselektronen gemessen wird. Die vorgestellten Messungen betreffen einen Energiebereich der Myonen, der wichtige Information für die sogenannte atmosphärische Neutrino - Anomalie und das Studium der Neutrino - und Antineutrino - Flüsse in der Atmosphäre liefert. Die Resultate aus zwei Meßperioden sind:

$$R(\mu^+/\mu^-) = 1.30 \pm 0.05\,(\text{stat}) \quad \langle p_\mu \rangle = 0.86\ GeV/c \quad \langle \theta_\mu \rangle = 26^o$$

$$R(\mu^+/\mu^-) = 1.27 \pm 0.01\,(\text{stat}) \quad \langle p_\mu \rangle = 0.52\ GeV/c \quad \langle \theta_\mu \rangle = 19^o$$

Für eine Diskussion in der Zusammenschau mit der experimentellen Information aus der Literatur werden eine umfassende Datenbasis und eine Übersicht über die "Weltkenntnisse" zum Ladungsverhältnis atmosphärischer Myonen erstellt. Die Ergebnisse werden verglichen mit Resultaten ausgiebiger Monte Carlo Simulationen mittels des Luftschauer Simulations - Programms CORSIKA. Verschiedene hadronische Wechselwirkungsmodelle, die als Generator bei den Simulationen verwendet werden, werden überprüft. Das Programm GHEISHA, das allgemein zur Berechnung niederenergetischer hadronischer Welchselwirkungen benutzt wird, zeigt ernsthafte Diskrepanzen. Einige Gründe dafür sind verstanden. Theoretische Voraussagen der VENUS - und FLUKA - Modelle werden präsentiert für einen Energiebereich der Primärstrahlung, der für den niederenergetischen Myonfluß bestimmend ist.

CONTENTS

Motto: Fortuna Imperatrix Mundi

O Fortuna,
velut Luna,
statu variabilis...

(Carl Orff - Carmina Burana, Cantiones Profanae)

O Fortune,
like the moon
you are changeable

1. INTRODUCTION

Primary cosmic rays are an important feature of the interstellar and intergalactic medium. They bombard our Earth's atmosphere with an integral intensity of about 1000 particles per second per square meter, most abundantly protons, helium, but also heavier nuclei, significantly up to iron. The contribution of primary electrons and photons to the total flux is found to be less than 1%. The energy spectrum comprises more than 11 orders of magnitude on the energy scale up to tremendous energies of 10^{20} eV. The spectrum falls rapidly down with the energy following a power law dependence $\propto E^{-2.7}$, up to the region of the so-called "knee" where the index changes abruptly to ≈ 3. This feature has been discovered 40 years ago [1], but the origin of the phenomenon is not clarified, in particular due to the lack of experimental information about the detailed shape of the primary spectrum and the accompanied variation of the mass composition of cosmic rays. Actually due to the low intensity, this region is no more accessible to direct measurements with balloon or spacecraft borne detectors and experimental studies rely on observations of extensive air showers (EAS).

EAS are induced by interactions of high energy cosmic rays with the nuclei in the atmosphere. From 15 – 25 km in altitude they start particle avalanches by cascading multiparticle production processes, which distribute the high energy of the primary particle to millions of secondary particles, propagating as a wide disk through the atmosphere, with three main components of charged particles:

- the electron – photon component which comprises 90% of the charged particles and originates from the disintegration of the neutral pions produced in hadronic interactions

  $$\pi^0 \rightarrow \gamma + \gamma$$

  Because the particles of the electron – photon component lose continuously energy when multiplying the number of particles by pair produc-

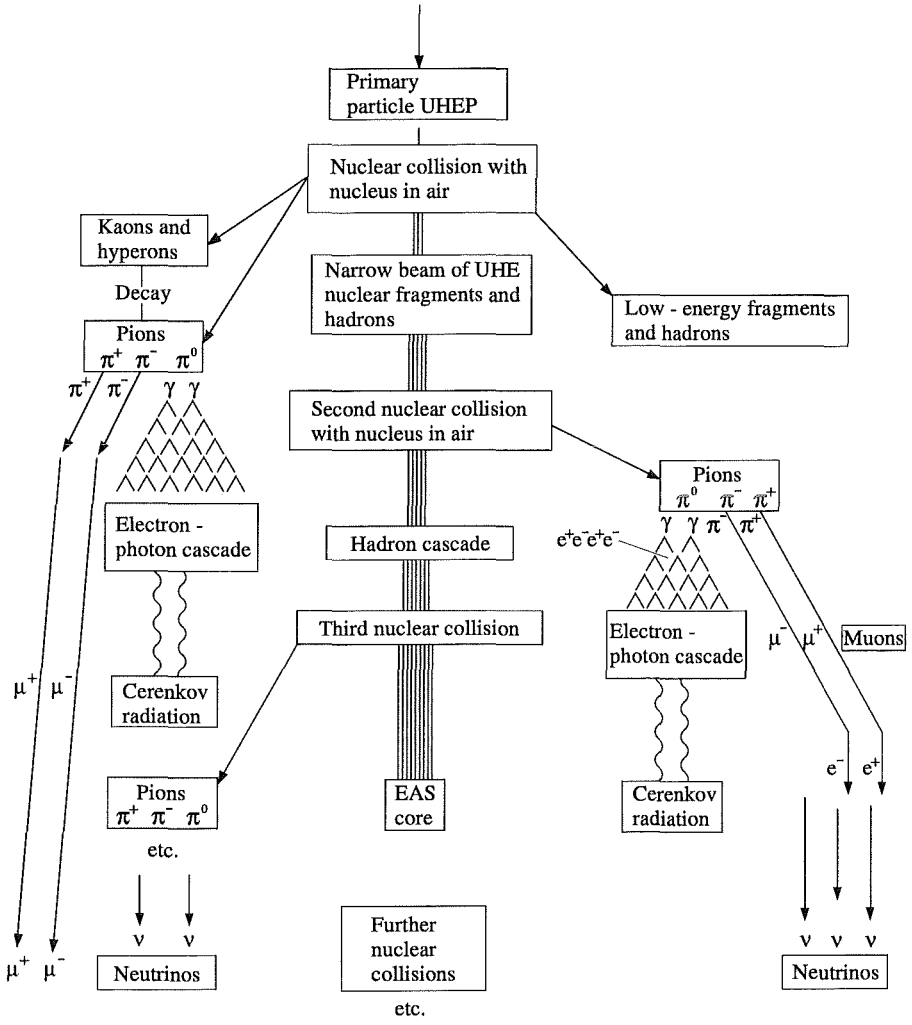

Fig. 1.1: Progeny of an Extensive Air Shower.

tion and bremsstrahlung there is an intensity maximum in the longitudinal EAS development. For instance a shower in the "knee" region has the maximum in the electromagnetic component at an atmospheric depth of 500 g/cm^2 (about 6 km in altitude) [2].

- the muon component originating from the decay of charged pions and kaons

$$\pi^{\pm} \rightarrow \mu^{\pm} + \nu_{\mu}(\overline{\nu}_{\mu})$$

$$K^{\pm} \rightarrow \mu^{\pm} + \nu_{\mu}(\overline{\nu}_{\mu})$$

which amounts to 5 – 10%. Muons form the penetrating component, since they get less absorbed and reach the ground from high altitudes. Therefore the muon component carries original information about the longitudinal EAS development [3, 4]

- the hadronic backbone of the EAS by $\approx 1\%$ of the particles.

There are a number of recent EAS observation experiments by large detector arrays at ground level focused to detailed investigations of the primary energy region of the knee [5, 6, 7, 8]. One of these experiments is KASCADE, installed in Forschungszentrum Karlsruhe, which is a multi-detector setup and approaches the topic of mass composition with a new technique, in particular by a simultaneous (event by event) observation of all three main EAS components with a large number of observables [1]

Due to the low absorption, muons from low energy showers, where the electromagnetic component "dies" at high altitudes, reach the sea level as uncorrelated particles. In the *inclusive* flux of the secondary cosmic rays the muon component is most dominant. Fig. 1.2 shows the integral momentum spectrum. The Earth's magnetic field gives rise to an azimuthal asymmetry of the muon intensity. It is mostly the low energy part that is affected to the extent to which the path lengths are different for charged particles coming from the East or West. The absorption and decay probabilities are influenced.

The zenithal dependence of the muon intensity can be described by the expression

$$I(\Theta) = I(0)\cos^{n}\Theta$$

where n proves to be a function of energy. Determinations of the value n show values around a mean of 2.0 for the integrated intensity over all momenta (see for instance [11]). A value of 2.02 ± 0.08 is reported in [12] for muons with momentum above 0.5 GeV/c. Assuming this value for the vertical intensity shown (Fig. 1.2) and integrating over the 2π solid angle, a surface of 1 m^2 will be crossed every second, on average, by 134 muons with energies above 0.5 GeV. Measurements of the behaviour of n as a function of momentum

[1] The author of the present thesis is member of the KASCADE collaboration (see Appendix D). The advanced status and actual results are displayed by the contributions to the 26th ICRC (1999) in Salt Lake City, Utah, USA. Though the present work is not based on data from KASCADE, methods applied in the context of the KASCADE experiment have inspired the analysis of the results of this work [9].

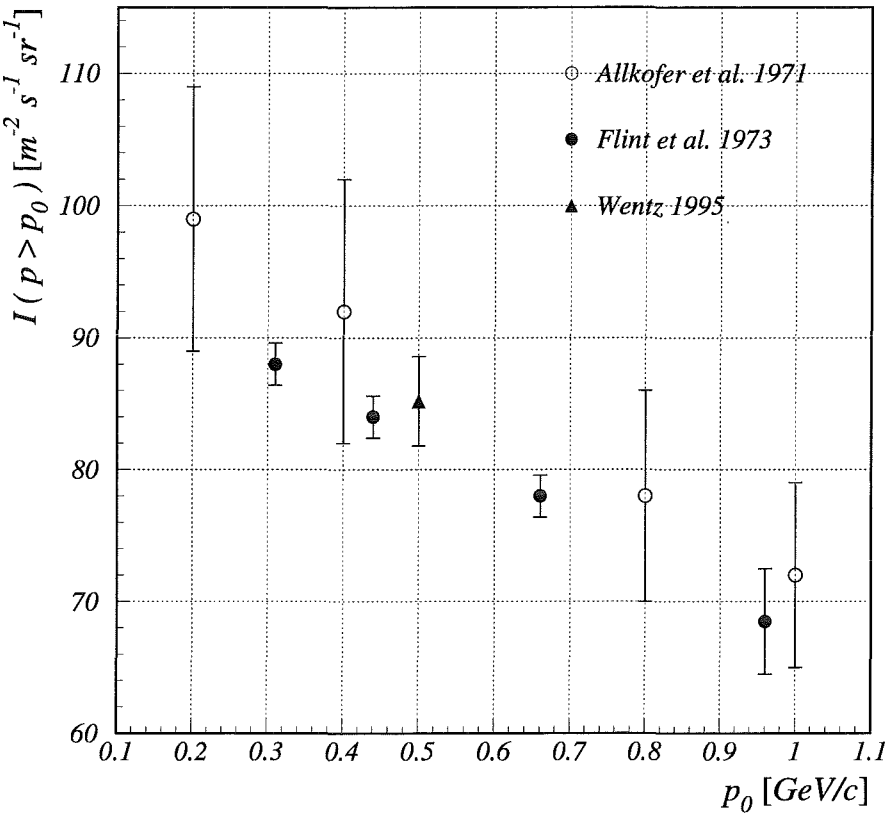

Fig. 1.2: Measurements of the integral vertical intensity of muons at low energy from [10] (Allkofer et al., Flint et al. from Fig. 2.2.2, p. 246) and [12] (Wentz).

have been subject to a number of experiments. In [13] measurements are compared with an existing calculation and show an integral exponent of 1.96 ± 0.22 and a differential value of 3.48 ± 0.07 at momenta in a narrow range around 1 GeV/c. Different exponents are found by measuring in East and West azimuthal directions.

Associated with the decay of charged pions, kaons and muons, the flux of atmospheric neutrinos is produced. The interactions of neutrinos are difficult to observe, therefore the measurement of this flux is a complicated task and is of actual interest. A knowledge of that flux (≈ 1 cm^{-2}s^{-1}) is an important issue for analysing the background of proton decay experiments [14].

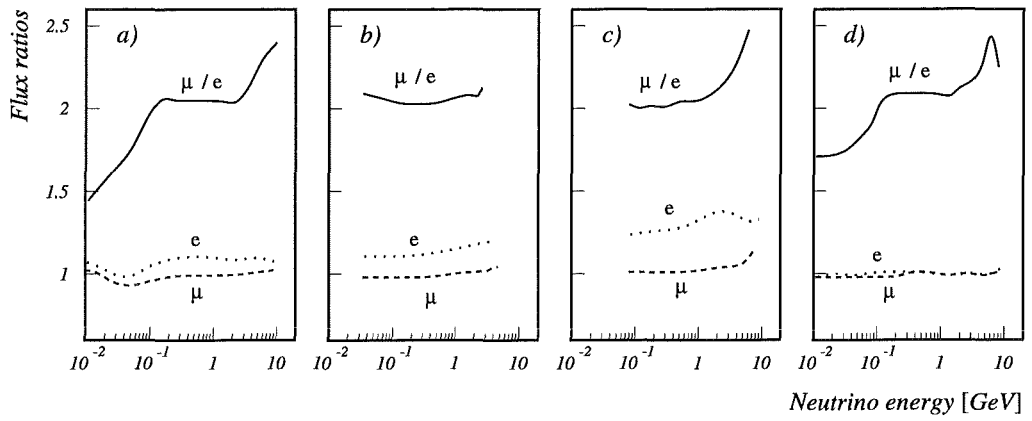

Fig. 1.3: The flux ratios of different ν flavours calculated for the Japanese KAMIOKANDE detector (μ and e denotes muon and electron neutrino, respectively). The models used in different calculations are discussed in [17].

In detail the neutrinos result from the following decay schemes

$$\begin{aligned} \pi^{\pm} \rightarrow \quad & \mu^{\pm} + \nu_{\mu}(\overline{\nu}_{\mu}) \\ & \mu^{\pm} \rightarrow e^{\pm} + \nu_e(\overline{\nu}_e) + \overline{\nu}_{\mu}(\nu_{\mu}) \end{aligned}$$

and a similar chain from kaons. From this scheme we infer for the ratios of different neutrino fluxes

$$\nu_e/\overline{\nu}_e \sim \mu^+/\mu^-$$

$$\nu_{\mu} \sim \overline{\nu}_{\mu} \sim 2\nu_e.$$

Thus it gets obvious that a knowledge of the muon charge ratio will give information about the ratio of neutrinos and antineutrinos in the atmospheric flux.

Muons in the atmospheric flux have a significant excess of positive charge. This a direct consequence of the nature of the primary cosmic radiation, dominated by positive particles (protons) and of the target consisting of oxygen, nitrogen and other nuclei in the Earth's atmosphere. This ratio is an input for a calibration of the neutrino underground detectors in terms of the neutrinos flux. Atmospheric neutrino fluxes have been calculated with

various degree of sophistication [15, 16, 17] (see Fig. 1.3). The results differ by as much as 30% in the overall flux, but the flavour ratio defined above is, however, agreed upon by all authors within 5%, except for momenta below about 0.1 GeV/c. From the experimental point of view, although the observed total event rates are consistent with the expectation for the interactions of atmospheric neutrinos, the ratio of muon-type to electron-type neutrinos is significantly lower than predicted by models [18]. By classifying the neutrino interactions according to the type of neutrinos involved and counting their relative numbers, the measured flavour ratio is compared to expectation

$$\frac{(\mu/e)_{data}}{(\mu/e)_{calculated}} = 0.67 \pm 0.04\,(\text{stat}) \pm 0.08\,(\text{sys}),$$

as it was measured by the Super - Kamiokande [2], experiment. Most recently confirmed, there is evidence in favour of the most intensively investigated physical explanation, the possibility of neutrino oscillations [19]. Oscillation is the changing of a neutrino's type as it travels through space or matter. This can occur only if the neutrino has a rest mass. The Super - Kamiokande result indicates that muon-neutrinos are disappearing into undetected tau-neutrinos or perhaps some new type of neutrinos.

The interpretation of the anomaly depends on a reliable calculation of the atmospheric neutrino fluxes, in particular on the ratio of muonic and electronic neutrinos. Unfortunately there exist a number of uncertainties arising from the hadronic models used as generators in the Monte Carlo simulations. In this situation the muon charge ratio proves to be a sensitive test quantity of the hadronic models and could help to constrain the uncertainties.

The thesis presented here aims at the experimental determination of the charge ratio in the atmospheric muon flux at low energies relevant for the atmospheric neutrino anomaly. The measurements are based on a method observing the different lifetimes of positive and negative muons when stopped in matter. The method has been worked out in detail and the experiment has been realized with a calorimeter setup (WILLI). For a precise determination of the muon charge ratio, the WILLI detector and the experimental method are shown to overcome the uncertainties of magnetic spectrometer

[2] Super - Kamiokande is a large water Cherenkov detector, consisting of a cylinder of roughly 40 m diameter and 40 m height and about 13000 very sensitive photomultiplier tubes, able to detect single photons, "looking" toward the inner volume of water.

measurements at low muon energies. A compilation of world data, mostly consisting of magnetic spectrometer experiments, is presented together with the present results, demonstrating the lack of precise measurements in this critical region. The results are considered in terms of predictions of Monte Carlo simulations, calculating muon fluxes. Muon momentum spectra and the charge ratio are compared with existing measurements up to 50 GeV/c. A discrepancy in the simulated muon charge ratio in the low momentum range, where it gives values lower than most experimental values is discussed in view of the realistic behaviour of the hadronic interaction model used.

2. EXPERIMENTAL METHOD FOR THE MEASUREMENT OF THE MUON CHARGE RATIO

2.1 Atomic and nuclear capture of negative muons

Except of the rest mass, muons and electrons have identical properties. Both belong to the family of leptons and have two charge states exhibiting weak and electromagnetic interaction. In many aspects muons can be considered as heavy electrons, however they are known to be unstable (see Table 2.1).

Particle	Mass [MeV]	Spin	Mean lifetime	Decay modes	
e^+	0.511	$\frac{1}{2}$	$> 2.7 \times 10^{23}$ yr	none	
e^-	0.511	$\frac{1}{2}$	$> 2.7 \times 10^{23}$ yr	none	
μ^+	105.6	$\frac{1}{2}$	2.19703 μs	$e^+ + \nu_e + \overline{\nu_\mu}$	$\approx 100\%$
μ^-	105.6	$\frac{1}{2}$	2.19703 μs	$e^- + \overline{\nu_e} + \nu_\mu$	$\approx 100\%$

Tab. 2.1: Properties of electrons and muons; positive and negative particles are charge conjugated (from [20]).

The main idea of the experimental method discriminating μ^+ and μ^- is based on the different behaviour of negative and positive muons after they are brought to rest in matter. While the positive muon has in matter only the possibility to decay, the negative muon is captured by the host atom forming a muonic atom. Just like electrons, negative muons fall on stable

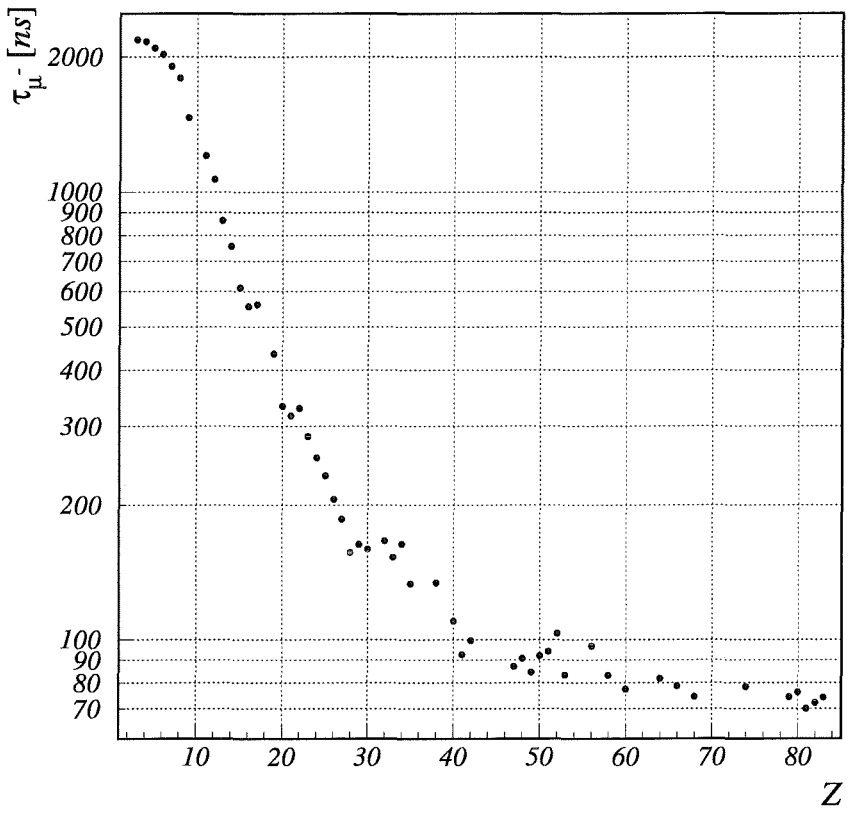

Fig. 2.1: Mean lifetime of negative muons in different materials measured in [23]. Due to its strong dependence on the nuclear volume, the lifetime shows systematic differences for some nuclei as compared to their neighbours, reflecting the odd-even variation of the nuclear radii.

Bohr levels with radius r_μ

$$r_\mu = \frac{(n\hbar)^2}{M_{\mu red} Z e^2}$$

where $M_{\mu red}$ is the reduced mass of the muon-nucleus system and Z is the atomic number of the host element. The mass of a muon is about 200 times larger than that of an electron. This results in a Bohr radius 200 times smaller than for the corresponding electron level with the same main quantum number. Due to its different flavour there is no exclusion by the Pauli

principle for the muon and within a short time (10^{-13} s) it cascades to the 1s level. In this state there is a considerable overlap of its wave function with the nucleus. The muon has now the possibility either to decay or to be captured by the nucleus.

The competition between these processes reduces the mean lifetime of the observed decay of the negative muon as compared with the free decay. Only muons not already captured are decaying in the orbit. Expressed in terms of process rates $\Lambda = 1/\tau$, the total disappearance probability is written as the sum of the capture and of the decay probabilities (either one or the other)

$$\Lambda_{total} = \Lambda_{capture} + \Lambda_{decay} \tag{2.1}$$

$$\Lambda_{decay} = Q\,\tau_{\mu^+}^{-1} \tag{2.2}$$

$$\Lambda_{total}^{-1} = \tau_{\mu^-} < \tau_{\mu^+} = 2.19703\ \mu s. \tag{2.3}$$

The inverse of the total rate gives the effective mean lifetime of the negative muons in the given material. The Huff factor Q takes into account that the normal muon decay rate is slightly reduced due to the binding of the negative muon in the atomic orbit, shrinking the phase space for the decay. The nuclear capture rate is determined by the overlap of the muonic orbit with the nucleus and it follows roughly a power law of the atomic number ($\Lambda_{capture} \sim Z^4$, [21]). This dependence is explained by the probability of nuclear capture being proportional to the overlap of the 1s muon orbit with the nuclear volume, becoming larger with smaller orbit radii ($1/Z$ dependence) and with larger nuclear volumes (approximately Z^3 behaviour). Starting with Z $\gtrsim$ 40 ($\sim$ Zirconium) the 1s Bohr radius for muonic atoms is smaller than the nuclear radius. In compounds, the nuclear capture is preferred by the nucleus with the larger nuclear capture rate, i.e. larger atomic number. For instance, in a plastic scintillator material (polyvinyl-toluol, 2-$CH_3C_6H_4CH{=}CH_2$ monomer) only the carbon capture is significant.

The capture of negative muons by nuclei via the weak interaction has been studied for many years, both theoretically and experimentally [22]. The atomic and the nuclear capture are accompanied by secondary effects. During the electromagnetic cascade down to the 1s level, photons by radiative transitions and Auger electrons are emitted. For heavy nuclei, nuclear Auger effect (neutron emission from nucleus) or prompt fission may occur also. The total capture rate is not easy to calculate as the final nucleus is excited to an unknown energy, which is the critical parameter from the theoretical point

Element	Mean lifetime [ns]	P_{decay} [%]
Carbon	2026.3 ± 1.5	92.15
Oxygen	1795.4 ± 2.	81.57
Fluoride	1462.7 ± 5.	66.48
Natrium	1204.0 ± 2.	54.61
Magnesium	1067.2 ± 2.	48.34
Aluminium	864.0 ± 1.	39.05
Silicon	756.0 ± 1.	34.14
Phosphor	611.2 ± 1.	27.57
Sulphur	554.7 ± 1.	25.00
Lead	75.4 ± 1.	2.75

Tab. 2.2: Mean lifetime and survival probability (probability of decay P_{decay}) for selected materials (from [23]).

of view. Nuclear gamma transitions, neutron evaporation or even charged particle and cluster emission can follow the muon capture.

However, from the experimental point of view the measurement is straightforward, the determination of the muon lifetime after stopping in the relevant material is simple.

A significant improvement as compared to most previous measurements has been provided by an experiment performed at TRIUMF (Vancouver, Canada [23]). It measured the lifetime of negative muons for 50 elements and 8 isotopes, with an accuracy of 2 to 3 ns for light elements (see Fig. 2.1). The mean lifetime and the decay probability after the atomic capture of negative muons for selected solid, liquid and gaseous materials are presented in Table 2.2.

2.2 The method of observing the different lifetimes of muons stopped in matter

Using the different lifetimes of muonic atoms compared with the lifetime of the positive muon, it is possible to measure the ratio of positive to negative muons in a flux, without using a magnetic spectrometer. The identification can be done by measuring the time decay curve of the muons stopped in a given material. A negative muon contribution to the flux is identified if the measured lifetime is different (smaller) than that of the free decay of 2.2 μs. In order to achieve a good accuracy, the required decay statistics and the time resolution of the experiment (width and number of time channels) depend on the chosen material. In lead the effective mean life time of the negative muon is most different but the decay probability is too small. Carbon gives too little difference to the positive muon lifetime, thus a high statistics per time channel is required. Therefore aluminium appears to be an optimum choice. Muonic atoms of aluminium have a quite different mean life time compared with the free decay of the positive muons, combined with a reasonable decay probability. Aluminium is relatively cheap, available with a high degree of purity and easy to be shaped according to the experimental requirements.

In a mixed flux of positive and negative muons, the observed decay curve cumulates decays of both positive and negative muons and even for a pure absorber it is no more one single exponential. In general, if a device detects decay electrons coming from muons stopped in different materials, the total decay curve will be a superposition of several decay laws

$$\frac{dN}{dt} = N_+ \, c_0 \, \frac{1}{\tau_0} \, exp\left(- \frac{t}{\tau_0} \right) + N_- \sum_{j=1}^{m} c_j \, \frac{1}{\tau_j} \, exp\left(- \frac{t}{\tau_j} \right) \qquad (2.4)$$

where

N_+, N_-	-	number of μ^+, μ^- which enter the detector
m	-	number of materials in the detector
c_0	-	detection efficiency for μ^+ stopped in all materials
c_j	-	detection efficiency for μ^- stopped in material j
τ_0	-	mean lifetime of μ^+ (2.19703 μs)
τ_j	-	mean lifetime of μ^- in material j

The mean life times τ_j, $j = 1, 2, \ldots m$ are taken from existing measurements [23]. The number of free parameters can be reduced further if c_0 and

c_j, $j = 1, 2, \ldots m$ are calculated theoretically. These constants express the stopping power of different detector materials and the probability that a decay electron escapes from the absorber medium and can be detected. For a simple block of material this can be calculated in some cases analytically, but more complicated modular geometries request detailed Monte-Carlo simulations. Finally, only N_+ and N_- remain to be determined. Instead of the two muon numbers, the total muon number

$$N_0 = N_+ + N_-$$

and the charge ratio

$$R(\mu^+/\mu^-) = \frac{N_+}{N_-}$$

are used, thus equation 2.4 is written as

$$\frac{dN}{dt} = \frac{N_0}{R+1}\left[R\,c_0\,\frac{1}{\tau_0}\,exp\left(-\frac{t}{\tau_0}\right) + \sum_{i=1}^{m} c_j\,\frac{1}{\tau_j}\,exp\left(-\frac{t}{\tau_j}\right)\right] \qquad (2.5)$$

This method is also called "delayed coincidences" from historical reasons (see chapter 3.5), as the signals from the decay electrons delayed in time from the incoming muon were determined by a number of electronic coincidence schemes by increasing delay values from the muon trigger.

2.3 Delayed coincidences from muon total capture

The experimental method described above assumes that the delayed particles correlated with stopped muons are only electrons from the decay of the muons while being in the nuclear orbit. If other particles accompanying the nuclear capture of the negative muon are detected, the values for the reduced mean lifetime presented above can not be used.

The nuclear capture of a negative muon is the weak absorption reaction on a proton

$$\mu^- + p \rightarrow \nu_\mu + n,$$

which becomes more complicated in the nuclear environment, for example

$$\mu^- + {}^{12}C \rightarrow \nu_\mu + {}^{13}B^*,$$

where $^{13}B^*$ has an unknown excitation energy. If particles are emitted from the excited nucleus and fake decay electrons, the effective lifetime will appear smaller than the values presented above. Following the comprehensive review mentioned above [22], the contribution of such secondary effects can be estimated.

The "mean" excitation energy in the nuclear muon capture is around 15 to 20 MeV. This is well above the nucleon emission threshold in all complex nuclei. The following capture products can appear:

- neutron emission is the preferred channel. The neutron multiplicity m has been determined experimentally by gamma-ray spectroscopy or by activation techniques. The average multiplicity $\langle m \rangle$ has the rough trend

  $$\langle m \rangle \approx 0.3A^{1/3}$$

  and has been measured for aluminium, $\langle m \rangle = 1.26 \pm 0.06$ and for lead, $\langle m \rangle = 1.71 \pm 0.07$ as well as for other elements. The energy spectra are dominated at low energies by the evaporation mechanism and by direct emission above 15 MeV.

- emission of charged particles is more probable for light nuclei than for heavy nuclei. Experimental evidence exists for the reactions $(\mu^-, \nu_\mu pxn)$ for $(x = 0-4)$. The yield per stopped muon is lower than for neutrons, because of the coulomb barrier. Alpha particles and heavier clusters can be emitted, too. The energy can reach few tens of MeV for protons and alpha.

- delayed fission can follow the weak capture reaction and becomes important for very heavy elements (actinides).

- gamma photons have energies of the order of MeV, with a spectrum decreasing from low to high energy and nuclear spectral lines.

- the radiative muon capture is the analogous in nuclei of the reaction

  $$\mu^- + p \rightarrow \nu_\mu + n + \gamma$$

  but it is rare as compared to the photonless ordinary capture.

Charged particles and clusters are difficult to be detected at the emitted energies. Experimental techniques for their investigations are based on emulsion

detectors. In conclusion, it can be said that neutrons and gammas are the only particles to be considered as source of systematic errors.

In the TRIUMF experiment the decay electrons were precisely identified. In a more complex detector, neutrons could produce secondary charged particles (for instance in organic scintillators) and the gammas have enough energy for direct electron - positron production.

3. THE DETECTOR

The WILLI detector (**W**eakly **I**onising **L**ead **L**epton **I**nteraction) is installed at the National Institute of Physics and Nuclear Engineering – Horia Hulubei (NIPNE-HH), Bucharest, Romania, located 44^o 26' N latitude and 26^o 04' E longitude, about 80 m above sea level. It was originally designed for prototype studies of electromagnetic cascades induced by the interaction of high energy cosmic ray muons in lead. The detector is a sampling calorimeter consisting of heavy absorbers (lead) between detecting elements (plastic scintillator plates inside aluminium boxes).

In case of high energy cosmic ray muons, individual interactions in the lead layers can be observed as emerging electromagnetic bursts (cascades of electrons and photons). The energy transfer in one muon interaction (δ electron, Bremsstrahlung and direct electron- positron pair production) is found in the total energy of the burst and can be measured from its longitudinal profile visualised (sampled) by the detecting elements. If the absorber is thick enough and the sampling is fine, the number of muon interactions and the energy transfers can be determined ("burst counter"). The experimental method and the theory of the "pair meter" (where direct electron - positron pair production by muons is the most important process to be taken into account) have been described first in [24]. Results of the prototype studies with this detector have been reported in [25, 26], but the actual size of the calorimeter seems to be below the necessary minimum number of radiation lengths, in order to have sufficient interaction statistics for a single muon and making a reasonable spectroscopy (as shown by simulation calculations in [27], with the MUONLM statistic analysis program in [28]).

Fig. 3.1 shows the initial sampling calorimeter configuration, further referred as WILLI-97. The detector consists of 20 lead plates 1 m^2 large and 1 cm ($\simeq$ 2 r.l.) thick and of 20 active modules. All is arranged in a vertical stack about 2 m high and on the top of the apparatus a 10 cm lead shield is placed. The shield is intended to absorb the soft component, i.e. electrons and gammas, in the case of spectrometer measurements. For low

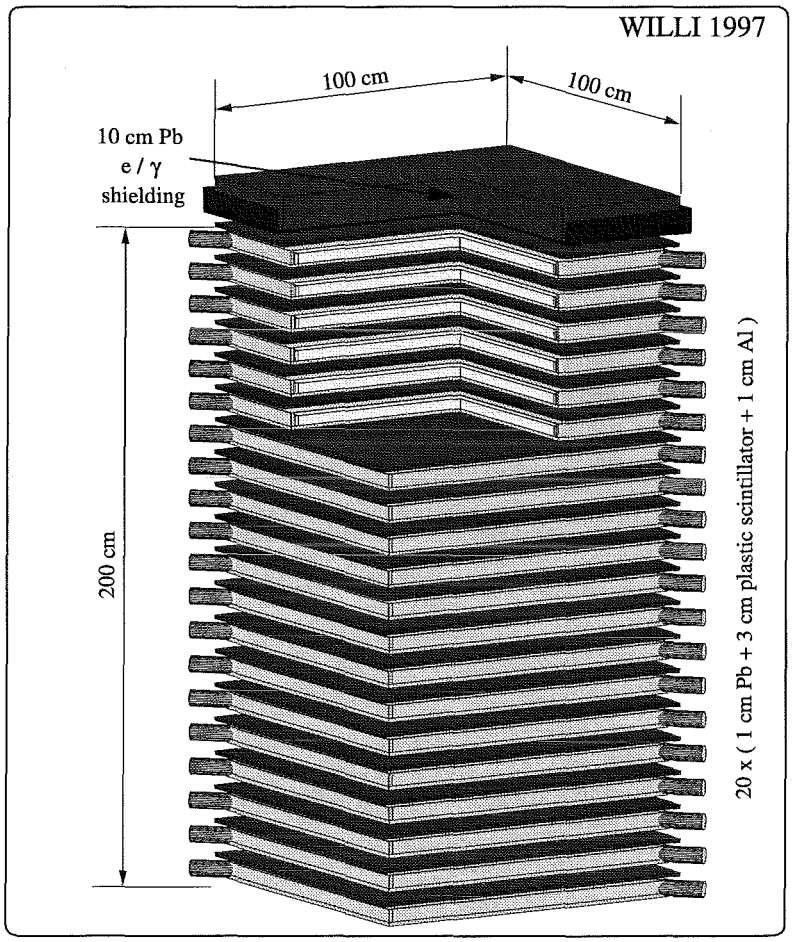

Fig. 3.1: The sampling calorimeter configuration of the WILLI detector.

energy muons it defines the energy threshold of the incoming particles which are afterwards stopped in the detector.

The detection modules are made of 90×90 cm^2 large area plastic scintillators (Fig. 3.2). The light is collected from the sides of the scintillator plate by wave length shifters (WLS), connected two by two to photomultipliers placed in opposite corners. Thin plastic threads are wrapped around the scintillator, so there is a small air gap between the scintillator and the WLS. The WLS material is a plastic with a small concentration of colour centres which absorb the scintillation light coming from the scintillator plate (with a spectral

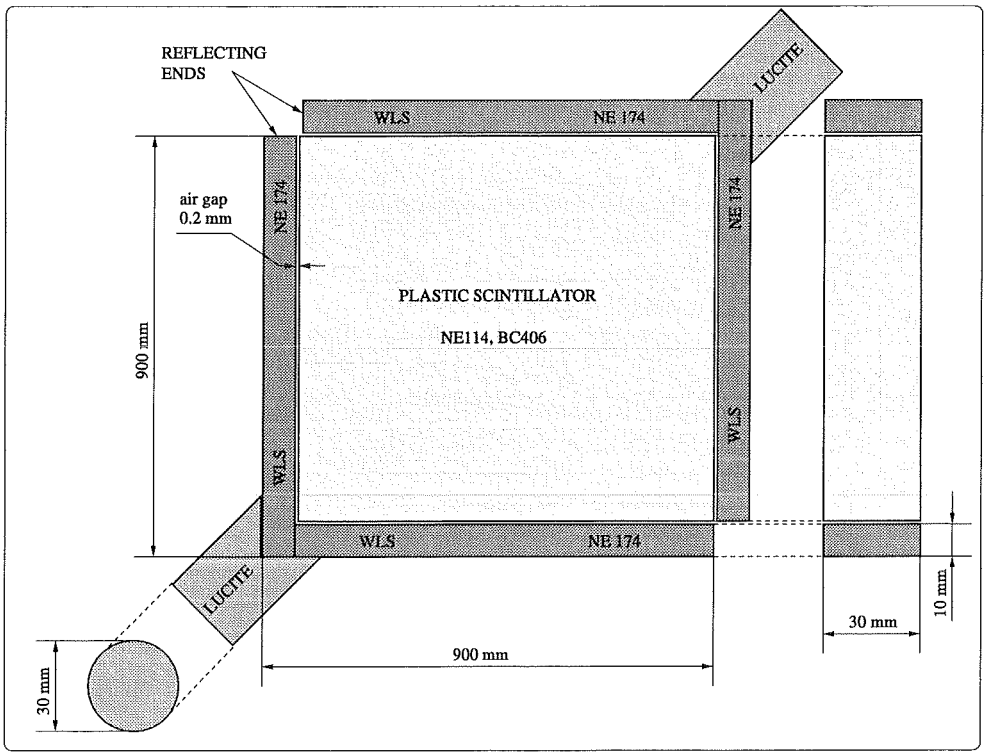

Fig. 3.2: The scintillator and the light collecting system inside one detection module.

distribution in the region of blue/ultra-violet) and then emit it again isotropically in the green region, where the WLS is practically transparent. The air gap increases the collecting efficiency by reducing the scattering of light back to the scintillator due to the total reflection. A lucite light guide adapts the geometry to the photomultiplier. The small area of the photo-cathode is then optically adapted to the light collecting area. The WLS technique improves very much the light collected from the large area scintillator, when only a small area photomultiplier is used. In the described geometry, the light collection is improved by a factor of 10, leading to a higher homogeneity of the light output in different points of the detector. With this geometry and modern fast materials like NE174 (short time constant), the dispersion of the time signal remains negligible compared with the time resolution of the electronic. The scintillator together with the light collecting system are

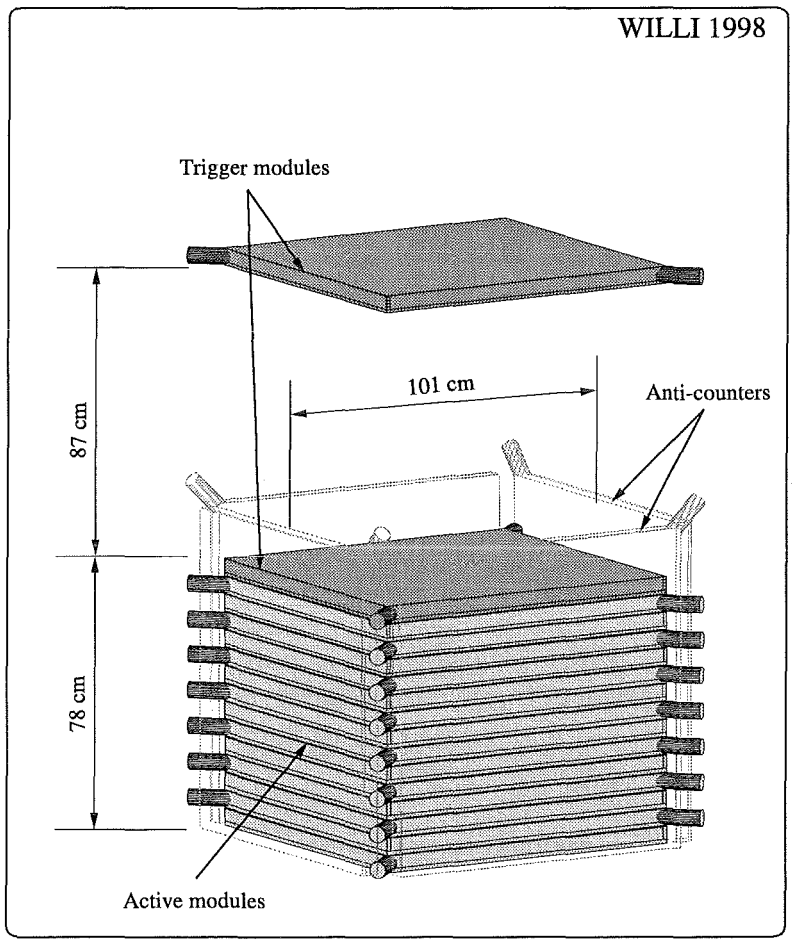

Fig. 3.3: The second configuration of the WILLI detector.

wrapped in reflecting foil and then closed in an aluminium box (1 cm thick lateral walls and bottom and 1 mm cover) on which the probes containing the photomultipliers are mounted.

In its second configuration the detector is dedicated for muon charge ratio measurements (Fig. 3.3 for WILLI-98). The lead plates have been eliminated and the geometry has been improved in order to have a background rejection with anti-counters. Four detector modules are placed in vertical position to cover the sides of the stack, with only one photomultiplier left for each plate. One detector module is elevated and makes a telescope trigger geometry,

restricting the solid angle around the vertical direction. The 10 cm lead shielding has been removed, in order to lower the energy range of the detected muons for the charge ratio measurements.

This arrangement insures that the signature of a muon decay event can not be fulfilled by two incident particles, one leaving the detector on the side and a second entering at the same layer.

The detector is situated in a laboratory at the basement of the Department of Experimental Fundamental Physics at NIPNE-HH. The building floors above contribute to the energy threshold in vertical direction with $\approx$ 60 cm reinforced concrete.

In the same building there is located the TANDEM accelerator, about 4 m above and 20 m lateral from the detector, but no significant additional background has been observed in the data during TANDEM operation.

3.1 The Data Acquisition System

Fig. 3.4 shows how the acquisition system is built, from the photomultipliers to the computer bus, where the acquisition program takes control of the data. The detector is equipped with 40 photomultipliers, each mounted in a probe containing

- the high voltage divider (from 10 quadruple power supply units, adjustable in the range 1100$\div$1600 V, in NIM standard),
- one preamplified output from the anode (A),
- one preamplified output from the third dynode, counted from the anode side (D); signals A and D are used for amplitude measurements,
- one preamplified output from the first dynode (T) used for time measurements.

All are connected with coaxial cables (of equal length in case of the time channels) to the rack with the electronics. The second energy measurement by using the dynode signal is necessary when high energy is deposited in the scintillator (as in the spectrometer prototype studies) and the anode saturates. The ratio between the anode and the dynode signal is adjusted at values $\approx$ 10.

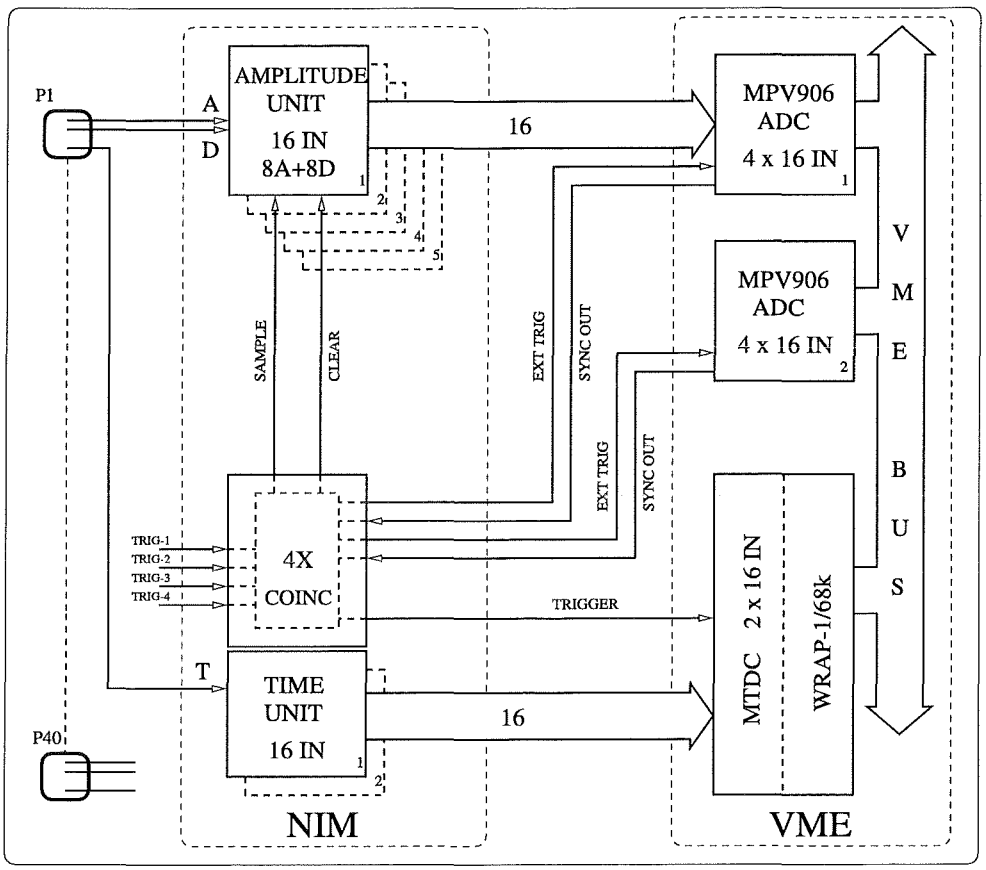

Fig. 3.4: The block diagram and signals of the acquisition system.

In its full configuration, the detector provides in total 120 signals to be processed for each event, carrying energy deposit (amplitude) and time information. A VME system links together the data peripherals, the CPU running the program under the OS/9 operating system and the storage media. This section describes the general configuration, the function of each part of the acquisition system, how one event is built, read out and written under the appropriate data format.

The signal processing is done by

- 5 modules, indicated as "AMPLITUDE UNIT" 1 to 5, each with 16 entries, for the 40 anode + 40 dynode signals (amplitude measurements),

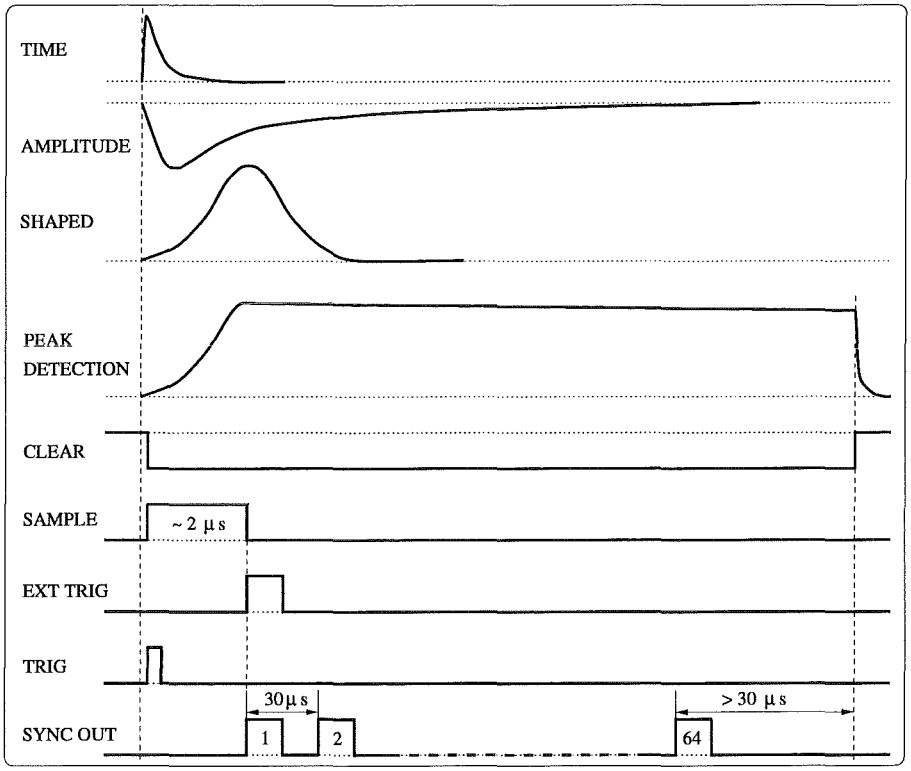

Fig. 3.5: The time diagram of the ADC conversion cycle.

- 2 discriminators, denoted "TIME UNIT" 1 and 2, each with 16 entries, for 32 signals selected from the 40 available (time measurements),
- one coincidences block "4x COINC" which supplies a trigger starting out of four TRIG signals within a window of 50 ns,

all built in NIM standard. The 80 amplitude processed signals are converted to digital values by two ADC modules (MPV906 1 and 2). One MPV906 Analog Input Board has 64 single-ended (or 32 differential) analog input channels and makes a digital conversion with 12 bit resolution. An input voltage in a range 0 – 10 V on one channel is converted into an integer from 0 to 4096. The time pattern is built and stored by a prototype module (the Multiple Time Digital Converter – MTDC) interfaced to the computer through the WRAP-1/68k module, described in more detail later. All interface modules are VME standard.

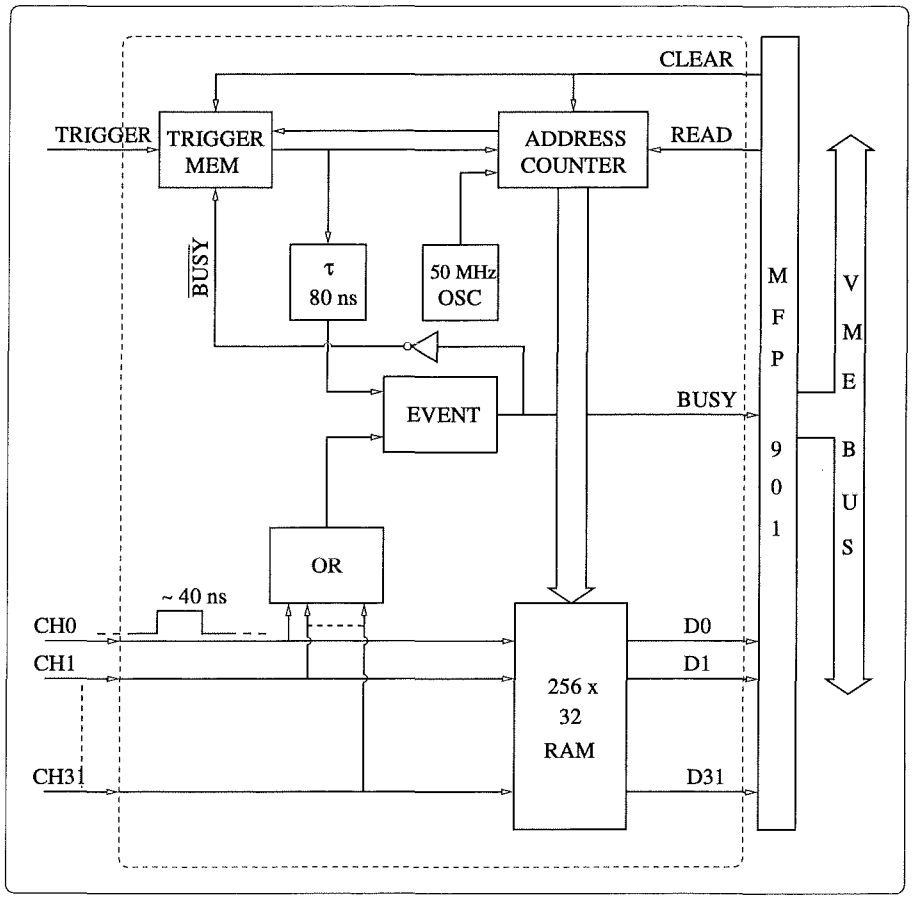

Fig. 3.6: The MTDC prototype.

Fig. 3.5 shows the time diagram of one ADC conversion of the amplitude signals, starting from the trigger signal TRIG. The AMPLITUDE signal coming from the photomultiplier is SHAPED in the AMPLITUDE UNIT module to a pseudo-Gaussian with fixed FWHM of about 4 μs and maximum value proportional to the integrated area of the initial signal, thus to the energy deposit. The ADC conversion is started with EXT TRIG and each input channel conversion is confirmed back to the trigger module by the SYNC OUT signals. When the conversion is finished (no more SYNC OUT), CLEAR returns to its state before the whole cycle and a new trigger event can be processed.

The 32 input channels for the TIME UNIT are selected according to the desired experimental configuration from the 40 probes available. These signals, stretched to $\approx$ 40 ns, are sent to the MTDC module, whose task is to record the time history of the event in a finite time window (Fig. 3.6). This is done in a 256 $\times$ 32 bit RAM memory with a resolution of 20 ns (by incrementing at 50 MHz the ADDRESS COUNTER), where the states of the time channels CH0 to CH31 are stored. After a cycle of 256 $\times$ 20 ns = 5.12 μs is completed, if decided, the RAM is read (D0 to D31) and 32 bit words are transferred to the VME BUS. In order to skip events from reading, where no delayed signal occurred in the time window of 5.12 μs, any signal delayed more than 80 ns to the TRIGGER sets the BUSY flag to inform both the acquisition program (the event is worth to be read) and the TRIGGER MEM module to reject any subsequent trigger signal. The CLEAR signal sent by the program prepares the module for a new event.

The acquisition program is briefly described in Fig. 3.7. It is written in the C programming language and has a main cycle which checks the status of the ADC module, noticing any conversion of existing input data, corresponding to a trigger. After the ADC data have been read, the BUSY flag of the MTDC module is checked for the existence of a delayed signal, in order to decide if the MDTC has to be readout. After the ADC is reset, the detector system is ready for the next event. The loop is closed after the program executes internal data processing and software filters and stores data in raw format on a disk file. An option is introduced in the program for runs where no MTDC information is needed (no MTDC delay validation and no MTDC read), for instance in the case of calibration acquisition described in section 3.2.

3.2 Data taking in two experiments on μ^+/μ^-

Data are stored on the VME hard disk in a binary (raw) format and then transfered to PC Linux machines from where they are written on 4 mm magnetic DAT tapes. One event consists of two blocks of information in the raw data, the ADC block and the MTDC block. Fig. 3.8 shows the structure of one event block in the raw data. Anode and dynode quantities are integers from 0 to 4096, corresponding to the 12 bit resolution of the analog converter and all 80 values are written for each event. Instead of writing the image of the MTDC RAM memory with a total size of 1 kB per event, the acquisition program does a zero suppression of the data and

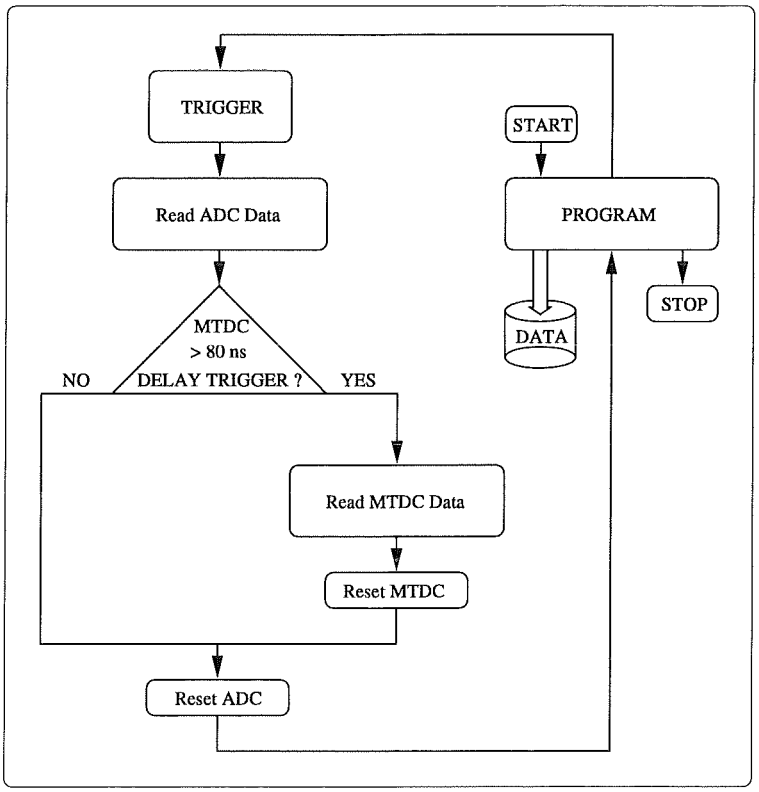

Fig. 3.7: The flow chart of the acquisition program.

extracts for the time channels only the number of hits and the corresponding positions, in the time window of 5.12 μs, expressed in numbers from 0 to 255. Thus, the MTDC block has a variable length which is generally less than 100 bytes.

With the WILLI-97 configuration of the detector, the experiment has been run for detecting the charge ratio of muons during 5 $\frac{1}{2}$ months in 1997. Fig. 3.9 shows for 60 runs, two different rates: the "ADC rate" is the rate at which ADC conversion cycles occurred and the "EVENT rate" is given by the data reduction using selection rules which will be described in the next chapter. For the WILLI-98 experiment the "MTDC rate" is shown too (the total run time was 3 months), given by the frequency at which the MTDC tags the ADC events with delayed signals in any of the 32 time channels in the given time window. The displayed "EVENT rate" is further

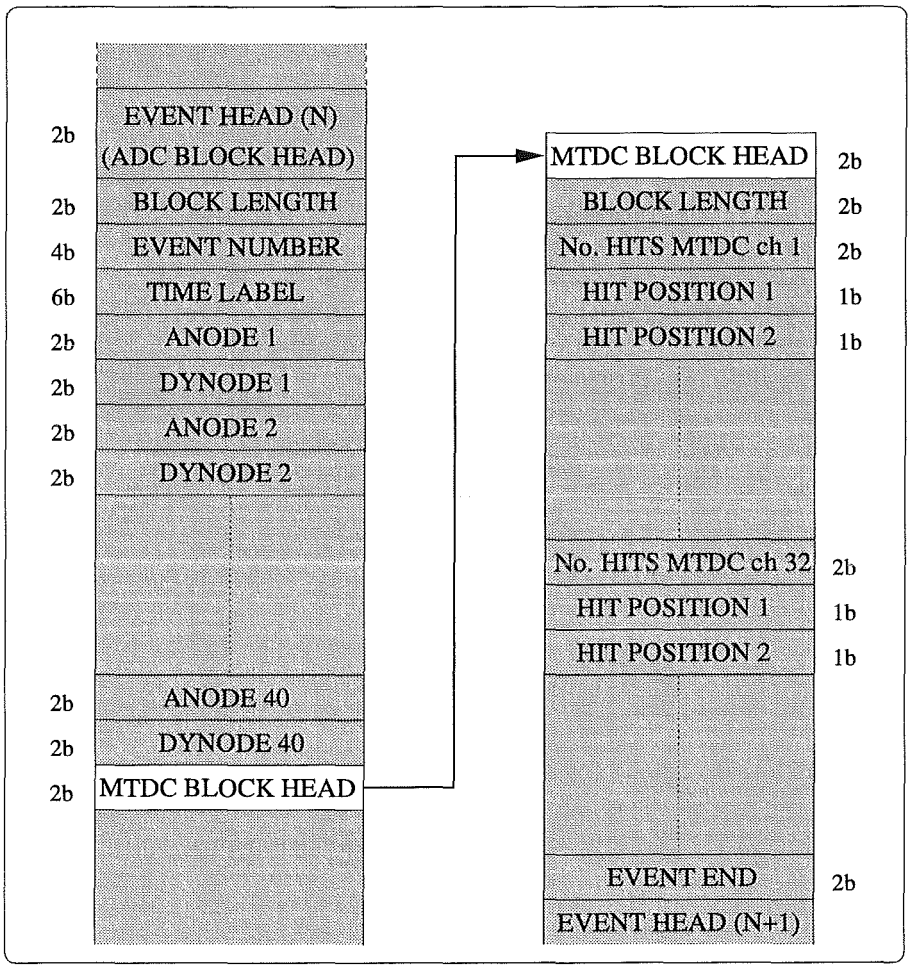

Fig. 3.8: Event block with ADC and MTDC information in raw data. The size of each field of information is given in bytes.

reduced by the background rejection. The difference between the two rates is mainly given by the change in the total stopping power of the detector (with or without lead plates) and in the angular acceptance determined by the trigger geometry. For one experiment, different runs correspond to a "start-stop" operation and have different data sizes. From one run to another, electronic adjustments have been sometimes made, or even the experiment was powered-off. Already investigated sources of rate difference are the slow

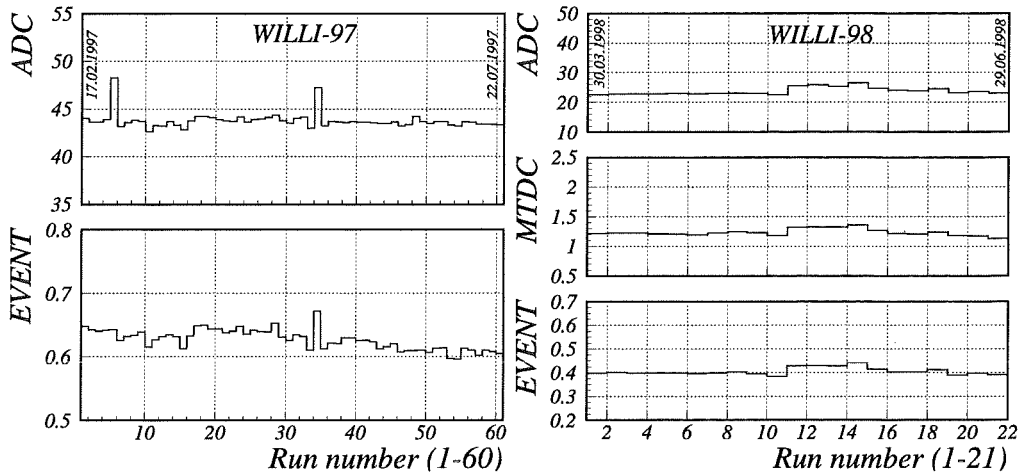

Fig. 3.9: Detection rates in the 1997 and 1998 experiments in events per second: ADC- trigger events, MTDC- trigger events with delayed signals and EVENT- selected events for the analysis.

drift of the high voltage applied to the photomultipliers over long periods of time (weeks, months), electronic noise in the time channels or problems with the high voltage connectors. In the latest version of the experiment normal runs are alternated with calibration ones in order to check the ADC signals status. For the simplicity of the data interpretation it is better to keep the calibration parameters constant during one experiment (see section 3.2).

For the offline data analysis, a program developed for a Linux machine with a Graphic User Interface facility for event-by-event and different spectra displays is used to analyse the data. Fig. 3.10 shows a typical image of the event display, where a muon has crossed the first 6 active modules from the top of the detector, possibly stopped and the decay electron has been detected about 2 μs later in the same layer where the muon has been "seen" for the last time. The absence of VETO signals in coincidence with the suppositional decay electron excludes the possibility of a background event, where a particle from outside penetrates one of the anti-counters, while the muon is absorbed without any further decay or the decay electron is not detected. In Appendix A other event patterns are shown from the graphical display and discussed in the view of the criteria for event selection presented in the next sections.

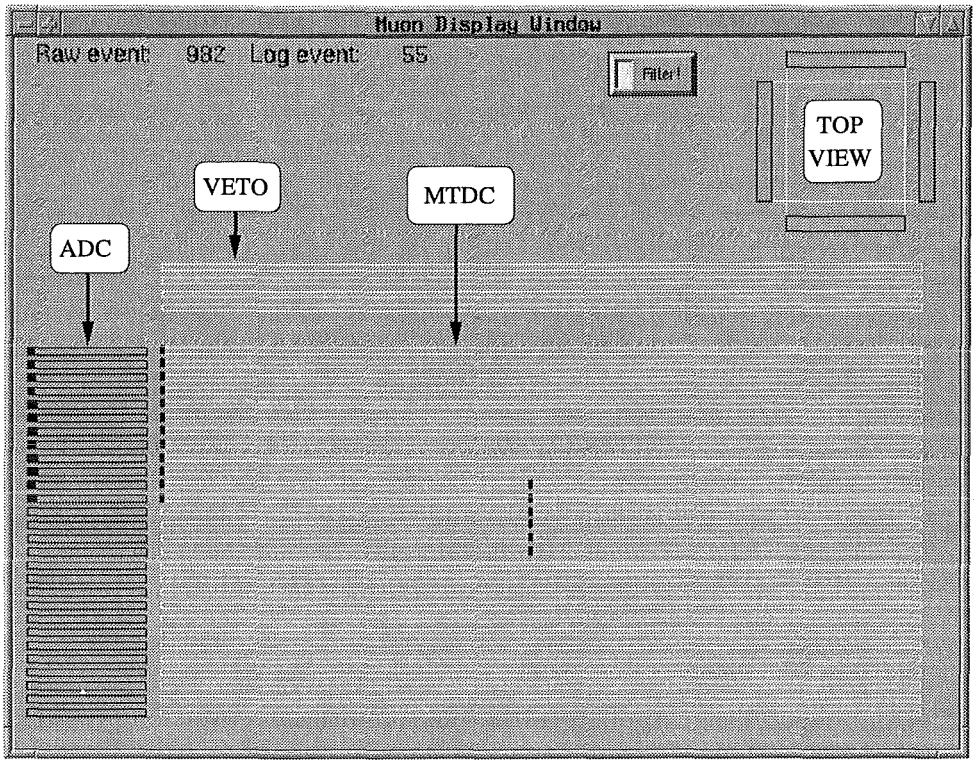

Fig. 3.10: The graphical offline display of one event (WILLI-98 experiment). The 28 ADC and MTDC signals corresponding to the 14 active layers are shown on a horizontal scale. The left scale shows in arbitrary units the anode amplitudes. The time signals are displayed as pixels set on a 256 scale. VETO time channels are shown shifted above the active channels. On the TOP VIEW the geometry of the VETO counters is specified and the amplitude signals are shown. The ADC signals from the 2 trigger modules are not shown. The passage of the muon which triggered the event is recorded by 12 amplitude signals and 12 time signals at the origin of the time scale. The decay electron generated 6 delayed time signals corresponding to 3 layers, starting from the layer where the muon was "seen" for the last time. In channels where only the decay electron is observed after the ADC conversion is finished, no ADC signals can be measured (see also Appendix A).

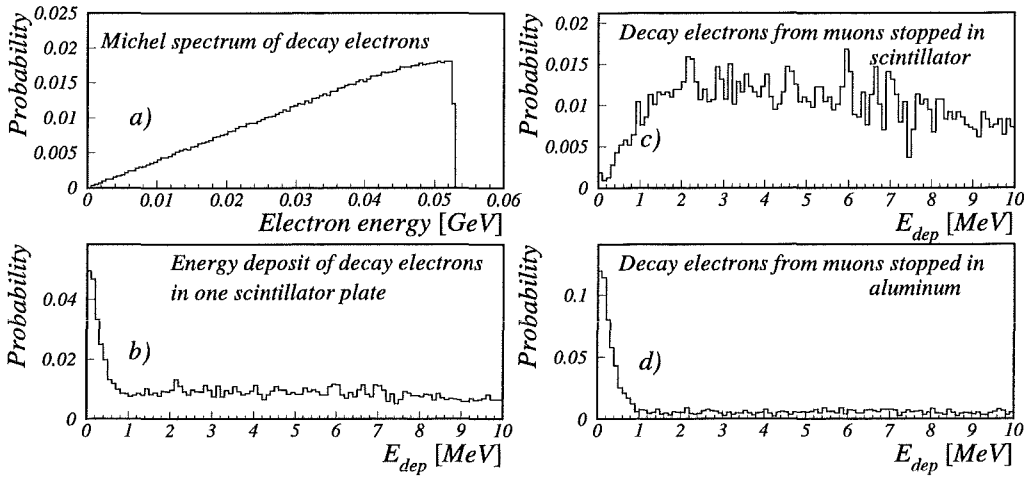

Fig. 3.11: The energy deposit of the decay electrons in the scintillator from Monte Carlo simulations (b) when muons stop in scintillator (c) or in aluminium (d). The energy spectrum of the decay electrons (a).

3.3 Detector calibration and efficiency calculations

The experimental method presented, requests some parameters of the detector to be determined. In order to investigate the correct contribution of each stopping material (aluminium or scintillator) to the experimental decay curve, the appropriate efficiencies have to be calculated. For the detector description and as Monte Carlo simulation tool, the GEANT 3.21 package is used [29]. The total shielding due to the building where the detector is installed is considered to be given by a 60 cm cumulated concrete in the vertical direction above the apparatus (standard shielding reinforced concrete [20]). As input data for the simulations, the muon energy spectrum above the concrete shielding has been generated according to measurements reported in [30], taking into account a distribution of the zenith angle $I(\Theta) = I(0)\cos^2\Theta$ and uniform distribution in the azimuth angle.

The GEANT package treats decay of unpolarised muons (isotropic decay).

The spectrum of electrons and positrons emitted in all directions is given by

$$N(x)\,dx \sim x^2 dx\left[(1-x)+\frac{2}{9}\rho(4x-3)\right]$$

with $\rho = 0.741$, the Michel parameter, where $x = E/E_0$ is the electron energy divided by maximum electron energy $E_0 \simeq 53$ MeV (Fig. 3.11a).

The efficiency for detecting a decay electron is defined by two conditions. First, electrons not produced in the scintillator must reach the active material. Second, the efficiency depends on the discrimination of the time pulses (proportional with the energies deposited in the scintillators) in the TIME UNIT, where certain thresholds have been set in order to eliminate noise. It is seen in Fig. 3.11b, taken from Monte Carlo calculation, that the energy deposited by electrons, if cut below a few MeV, appreciably reduces the number of decay electrons detected. This cut is different when electrons come from muons stopped in scintillator or in aluminium, due to the different absorbing material (Fig. 3.11c, d) which determines the residual energy of the electron entering the active material. These thresholds are slightly different from one module to another and must be determined by comparison between data and simulations, therefore a calibration of the deposited energy in each active module is performed.

In order to obtain a sufficient number of data points for the energy calibration, a special acquisition runs. Using a simple coincidence between the first and the last layer of the detector, single muons are detected at high frequencies. Due to the lead in the WILLI-97 configuration (shield and plates), practically all events in such a calibration run are single through going muons, which undergo minimum ionisation in each layer. In the WILLI-98 configuration, there is a small probability that other charged particles are detected.

Fig. 3.12 shows results of a 2×10^5 events calibration run in the WILLI-98 configuration for one active module. One anode signal distribution has the shape of a Landau distribution, given approximately by

$$f(x) = C\ e^{-(x_1+e^{-x_1})/2} \tag{3.1}$$

where

$x_1 = \dfrac{x-x_0}{s}$, with x_0 - most probable value and s - straggling parameter.

The symmetric combination of the two anode signals of one layer $(A_1 - A_2)/(A_1 + A_2)$ shows the effect of the position dependence of the signals

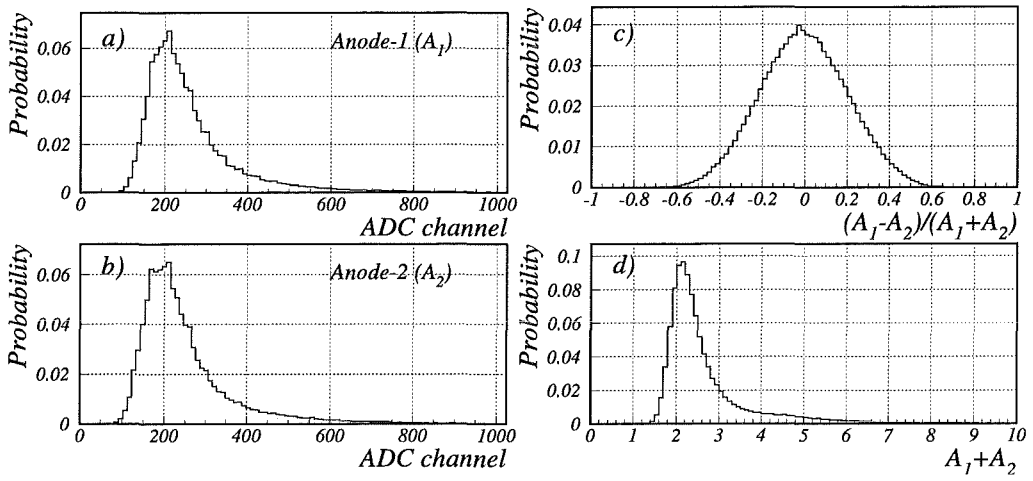

Fig. 3.12: Anodes ADC spectra in the calibration data (a,b). The symmetric combination of the two anode signals (c) and the sum of them as it appears in the calibration relation (d).

in such a large area scintillator, due to different attenuation of the light collected by the two photomultipliers. In Fig. 3.12c, d, the anode signals have been normalised to the most probable value (determined from a local fit with equation 3.1), in order to compensate different amplifications along the ADC channels. The energy deposit can be reconstructed from the calibration data, event by event, with the relation

$$E_{dep}^{exp}[MeV] = \alpha_1(A_1 + A_2)\ exp\left(- \alpha_2 \left| \frac{A_1 - A_2}{A_1 + A_2} \right| \right), \tag{3.2}$$

and the experimental resolution can be taken into account by applying

$$\sigma_E = \alpha_3 \sqrt{E_{dep}^{sim}[MeV]}, \tag{3.3}$$

to the energy deposit value obtained in simulations, before comparing it with E_{dep}^{exp}. The three parameters, α_1, α_2 and α_3, have been determined for each scintillator plate from the active modules by minimising the difference between the data and the simulation spectra. The exponential factor multiplying the anode sum accounts for the position sensitivity of the detection in

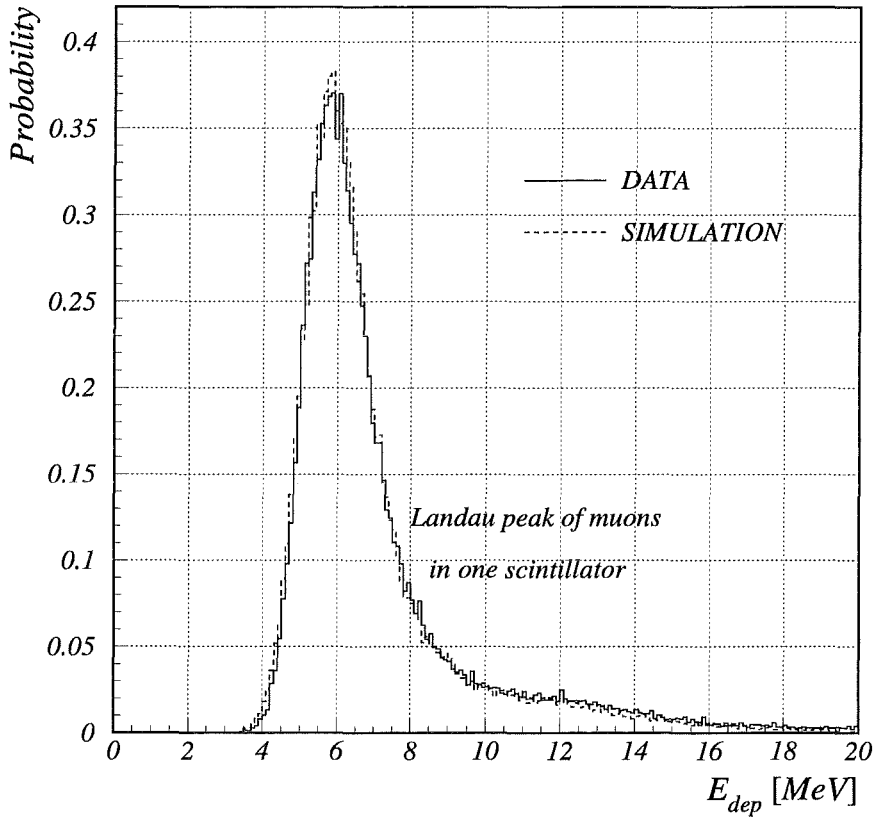

Fig. 3.13: Energy deposit in the scintillator of one calibrated active module.

the scintillator plate, its form is empirically deduced from the behaviour of the asymmetry expression shown in Fig. 3.12 and the exponential character of the light attenuation in the scintillator. Fig. 3.13 shows the result of the calibration for one active module. For instance, the parameters α_1, α_2 and α_3 for the calibration of the WILLI-98 detector configuration take values in the ranges $2.5 - 2.9$, $0.0 - 0.4$ and $20\% - 40\%$, respectively, for different active modules. An acceptable error for the determination of the thresholds must be less than 1 MeV (see below), which corresponds to about 40 ADC channels. The changes in the total gain of the ADC chains are monitored in order to keep them around stable values (see section 3.1).

The shape of the energy threshold is then obtained by dividing the corresponding energy deposit distribution from data and simulations. In Fig. 3.14

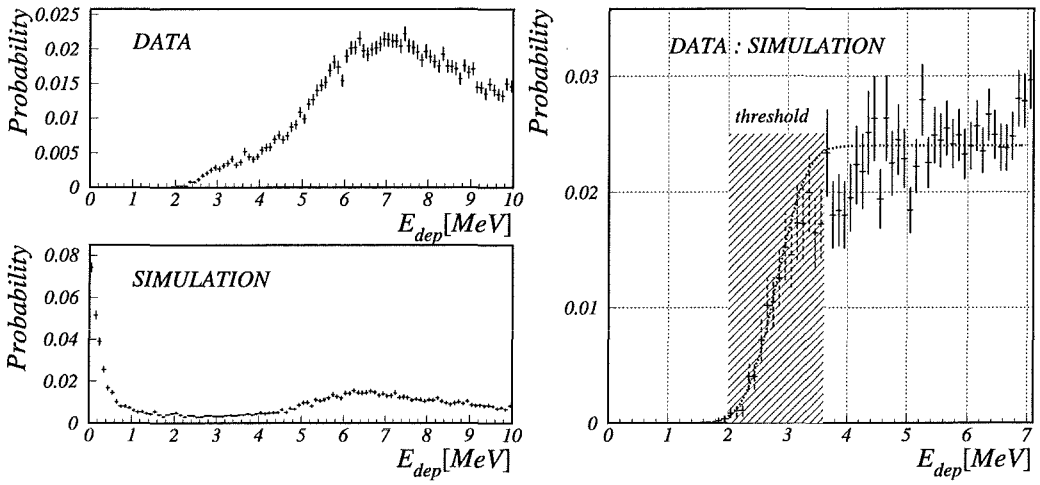

Fig. 3.14: Energy deposit in one scintillator from data and simulation and the determination of the threshold; a Gaussian distribution if assumed for the shape, with $E_{thr} = 2.8$ MeV and $\sigma_{thr} = 0.4$ MeV.

this step is shown for one module. The behaviour of the leading edge discriminators applied to the time signals results in a fluctuating cut of the energy deposit, as seen in Fig. 3.14c. A "normal frequency function"

$$\text{Freq}\,(x) = \int_{-\infty}^{x} G(x')\; dx'$$

where $G(x)$ is a Gauss distribution, can be used to approximate the behaviour of the threshold. The thresholds for different active modules have mean values in the range 2.4−4.3 MeV and they are introduced in the simulations as fluctuating around this mean value with a Gaussian variance of 0.3−0.6 MeV.

An alternative method is based on measurements of the electrical pulses going from the photomultipliers to the AMPLITUDE UNITS and to the TIME UNITS (discriminators). Once the ratio between the energy and time signals is determined, each voltage threshold of the 32 discriminators can be translated in an ADC threshold for the corresponding photomultiplier

$$A^i_{thr}[\text{ADC channel}] = 0.4096\;\frac{V^i_{thr}[\text{mV}]}{\rho_i}$$

where ρ_i, the signal ratio, is determined with a double beam synchroscope

over several measurements and taking the mean value. The constant multiplying the fraction results from dividing the number of ADC conversion channels, 4096 by the ADC input analog signal range, 10 V expressed in millivolts. The measured distribution of the ratio of the two photomultiplier signals in one plate (Fig. 3.12c) is used for sampling the position dependence of the two signals. Together with the energy calibration relation from equation 3.2, this allows to express one value of the deposited energy in one scintillator plate, obtained in the simulations, by the corresponding ADC values of the two photomultipliers connected to that plate. The A^i_{thr} measured thresholds can be applied to the simulated ADC signals. The results of these two methods appear in fair agreement. The difference comes from the fact that the cut of a leading edge discriminator depends on the shape of the pulse (from the integration) and is therefore not precisely proportional with the amplitude of the pulse.

3.4 Event selection and total decay spectrum analysis

A muon decay event is identified by a "signature" like in Fig. 3.10, but the patterns are generally more complicated and are affected by noise, background and missing detector efficiency. The following cuts are applied to data and to simulations, in order to filter events which fulfil the signature of a decay:

- the two time signals from one scintillator plate must occur coincident in time;
- only events with two clearly subsequent particles are accepted for each MTDC channel;
- the muon track ("zero" signal of each MTDC channel) must be continuous from the first active module down to the "stopping layer";
- there is one coincident delay of a particle which starts around the same layer where the muon stopped. For WILLI-97 the electron is seen in maximum 2 layers with reasonable frequency, because even a 53 MeV electron is stopped fast in lead. For WILLI-98 the number of possible patterns increased together with the length of the track of the electron which can now be seen in up to 3 layers.

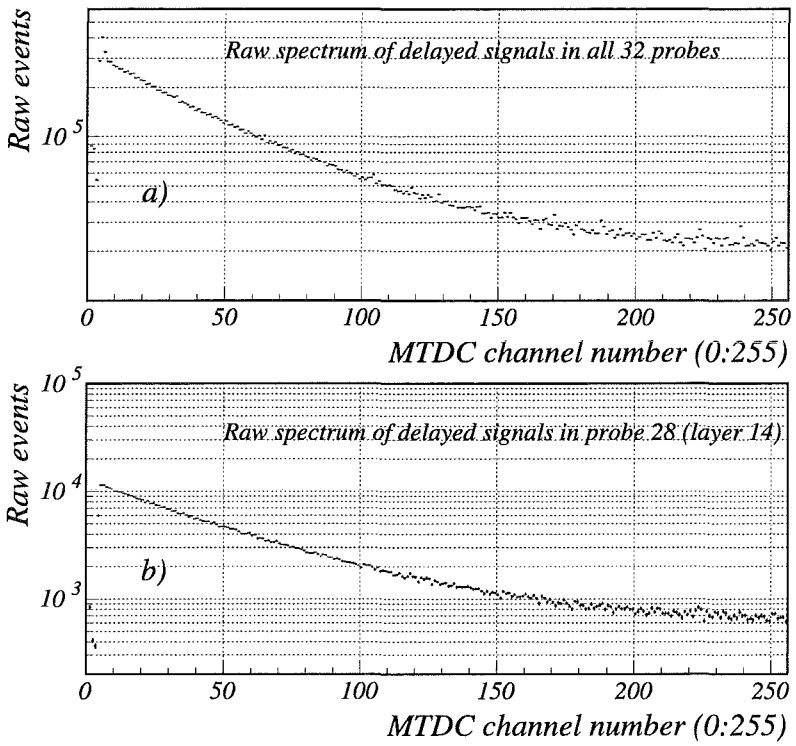

Fig. 3.15: Raw time spectra of delayed signals collected from all active layers (a) and for a single probe (b).

These cuts are quite restrictive and a considerable number of decay events are lost, but the cuts result in a maximum signal to background ratio, essential for the further analysis. The exponential character of the measured decay curves is not influenced, positive and negative muons being lost with equal probability.

Fig. 3.15 shows the raw spectra of the delayed MTDC signals for all 32 channels (a) and separate for one probe belonging to the first active layer after the trigger telescope (b). After applying the cuts to the data, 8 classes of patterns are identified with a reasonable frequency of occurrence in the WILLI-98 experiment. In Fig. 3.16 the MTDC channels around the stopping layer are shown as horizontal lines, with the muon "track" at the left and the decay electron seen in 1, 2 or 3 layers. In the WILLI-97 configuration only the first 5 classes are relevant.

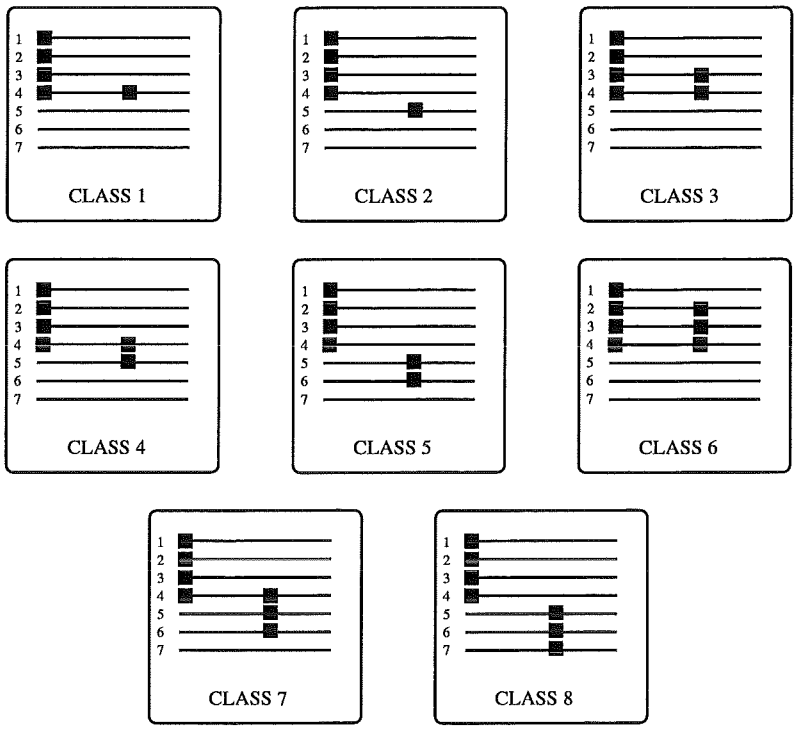

Fig. 3.16: Patterns of the MTDC information for muon decay events.

As mentioned in section 2.2, there is the possibility that also captured muons give a delayed response in the detector, which could pass all filters described above. In order to investigate this source of systematic errors, in the experimental analysis, a version of the simulation program has been modified to include other branches except normal decay, after the muon is stopped (WILLI-97): emission of neutrons from an evaporation energy spectrum with temperatures and multiplicities mentioned in [22] and gammas from a decreasing energy spectrum up to a few MeV. Due to the production (conversion) of ionising particles in the detector modules, both neutrons and gamma could fulfil in a small fraction the "track" continuity conditions. In Appendix A patterns in the data suitable to such an interpretation are presented. This effect is seen as slightly different value of the mean lifetime of the negative muons used in the analysis of the time decay spectrum. Because of insufficient knowledge of these processes, this was not introduced in the final analysis.

In the WILLI-98 configuration further data reduction is made, by selecting contained events (along the axis of the detector) with the conditions:

- there is no signal in any of the 4 anti-counters on the sides, in the whole time window;
- in the top active module (below the trigger module) only the signal of the muon is seen (also in WILLI-97);
- the bottom active module gives no signal.

These three conditions practically define a complete anti-counter. Even with all selections, there is still some residual background of very low level coming from the following possible sources:

- neutral particles converting to ionising particles within the fiducial volume,
- radioactive decay of materials inside the detector,
- the anti-counters cover less than 4π around the fiducial volume ($\simeq$ 96.7 %).

The background suppression by anti-counters and the residual background are analysed for the WILLI-98 experimental configuration with a run using a 5 MHz clock, thus a total time window of 51.2 μs. The spectrum collected over few weeks data acquisition shows a well defined background after 20 μs, whose value is determined by fitting with a constant function (in fact the random background is an exponential with the slope given by the inverse of the secondary cosmic ray flux, thus of the order of tens of milliseconds!). Fig. 3.17 shows how the background events are distributed over the stopping layers, with a large contribution in the upper active module (number 7) which is eliminated from the modules containing delayed signals (see conditions to filter events). The excess in the bottom layers could be explained by an increased noise in the photomultipliers or by the natural radioactivity of the concrete floor (^{40}K at 1446 keV). The right graphs show the subsequent effects of applying the fiducial volume and the anti-counter filters.

In Fig. 3.18 the results of the simulations are used to illustrate the decay exponentials given by decay electrons from muonic atoms in different materials, i.e. their contribution to the total decay curve, measured by the experiment (in the simulations equal numbers of positive and negative muons are

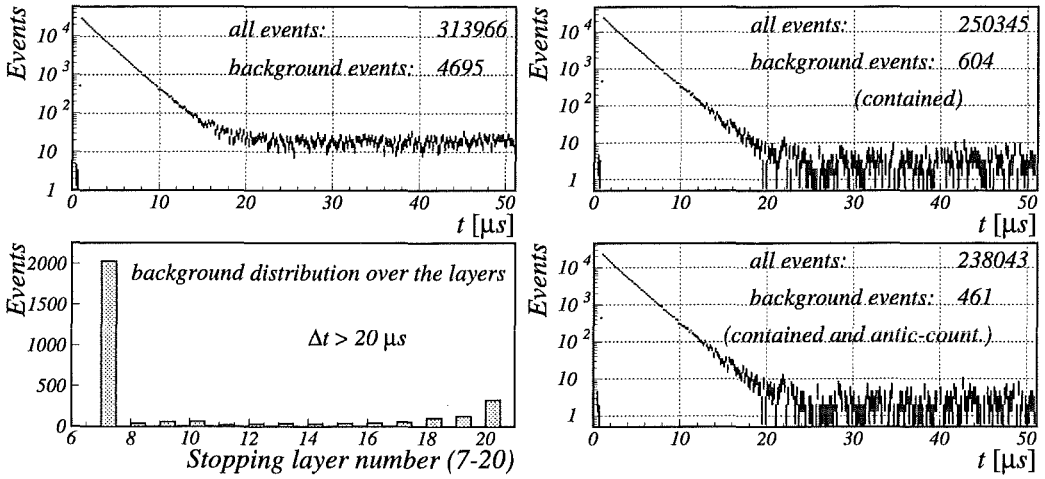

Fig. 3.17: Background measurements in a 51.2 μs time window.

assumed). The measured decay curves of the two experiments have statistics of 5.3×10^6 and 2.3×10^6 events, for the WILLI-97 and the WILLI-98 experiment, respectively. It can be seen that the lead brings no useful information, due to the large probability of negative muon nuclear capture. The doubled time window of the WILLI-98 experiment (10.67 μs instead of 5.12 μs) and the double efficiency in detecting electrons from aluminium (no lead in between) improve the separation of the different exponentials. Even with half total statistics, WILLI-98 provides a more accurate experimental result.

By comparing how the stopped muons are distributed over different layers and the relative frequencies of different event classes between the Monte Carlo simulation and the experiment, a check of the simulation is done (Fig. 3.19). While the event classes are well reproduced, there is a systematic difference in the distributions of the stopping layers between experiment and simulations. This distribution results from the correlated distributions in energy, the zenith angle of the incoming muons and the stopping power of the detector. The sensitivity in muon energy for this configuration is in the range of few hundred MeV, where few reliable measurements of the muon spectrum exist (required as input for Monte Carlo simulations), due to considerable difficulties in the spectrometer experiments. At this low energies, any absorber introduces a strong correlation between the large angular scattering and the

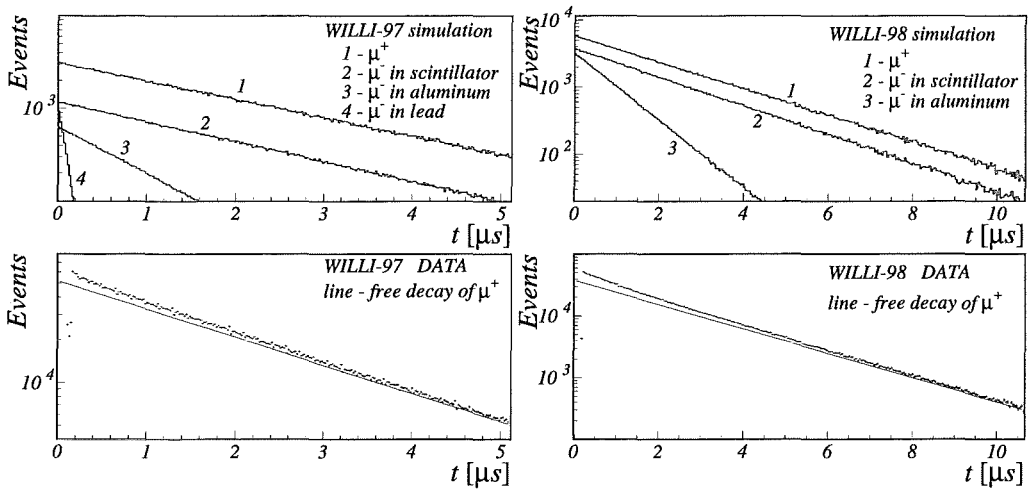

Fig. 3.18: Monte Carlo simulation results on different material contribution to the total decay curve and the experimental data decay curve compared with the free decay of positive muons ($\tau = 2.2$ μs).

attenuation in energy, thus a simulation of the concrete environment of the building, better than the approximation made by the 60 cm concrete uniform shielding, might be necessary. In Fig. 3.19 the dotted line displays the distribution of the stopping layer when another muon energy spectrum is assumed in the simulations for the incoming muon above the concrete shielding with the same configuration. This muon spectrum from an air shower simulation code (CORSIKA, see next chapter) results in more low energy muons which stop in upper active modules and a systematic shift of all distribution is noticed, nevertheless not enough to have complete agreement with data.

3.5 Results

The equation 2.5 from section 2.1 becomes for the decay events accumulated in the experimental histograms

$$\Delta N(t_i \pm \Delta t/2) = \frac{N_0}{R+1}\left\{R\ c_0\ \delta_0\ \exp\left(-\frac{t_i}{\tau_0}\right) + \left[\sum_{j=1}^{m} c_j\ \delta_j\ \exp\left(-\frac{t_i}{\tau_j}\right)\right]\right\}$$

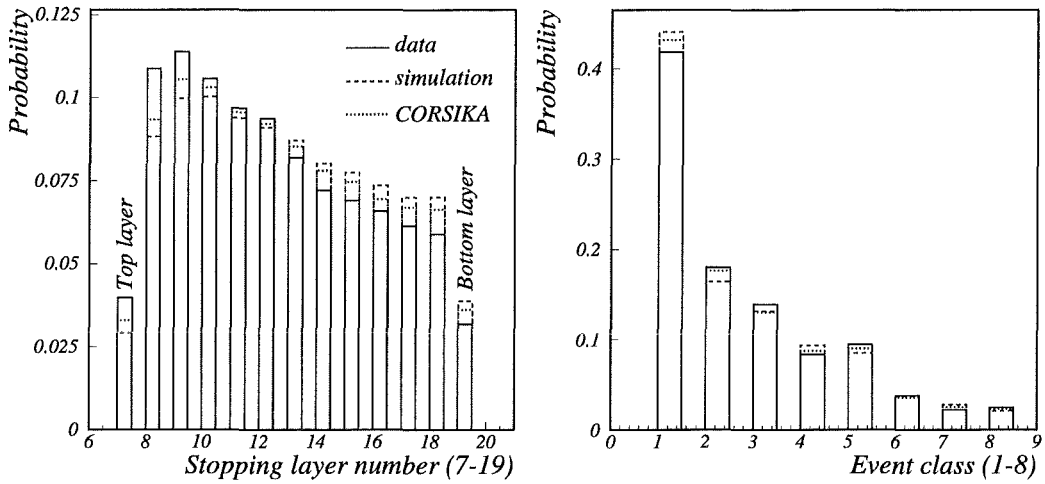

Fig. 3.19: WILLI-98 comparison of data with simulation: the distribution of the muons stopped in the detector and the relative frequency of different event classes ("simulation" is the Monte Carlo calculation based on the experimental flux of muons, while "CORSIKA" means that the flux of muons is a result of the CORSIKA code).

with $m = 3$ for the WILLI-97 experiment (aluminium, lead and scintillator) and $m = 2$ for the WILLI-98 experiment (aluminium and scintillator). Because GEANT 3.21 does not include handling of nuclear capture, the detection probabilities for negative muons are split in

$$c_j = c_j^* \; p_{decay}^j \qquad j = 1,\ 2,\ 3, \tag{3.4}$$

where only c_j^* have to be determined from the simulation and the decay probabilities p_{decay}^j are taken from [23]. The corrections

$$\delta_k = \left[\exp\left(\frac{\Delta t}{2\tau_k}\right) - \exp\left(-\frac{\Delta t}{2\tau_k}\right)\right]$$

$$k = 0, 1 \text{ to } m, \qquad \Delta t = \frac{1}{f} \qquad f = \text{oscillator frequency}$$

result from the integration over the time bin and t_i takes 256 values from the centre of the Δt time bins. The oscillator frequency is $f = 50$ MHz for

Fit range [μs]	R(μ^+/μ^-)	ΔR	χ^2/F	NP
0.3 – 10.4	1.27	0.01	1.18	244
0.8 – 10.4	1.27	0.02	1.15	231
2.0 – 10.4	1.28	0.05	1.03	201
0.4 – 8.8	1.27	0.02	1.29	201
1.6 – 6.2	1.27	0.05	1.27	111
2.0 – 6.2	1.30	0.07	1.26	101
6.7 – 10.4	1.13	0.49	0.73	91

Tab. 3.1: Results of the WILLI-98 data fit in different time intervals of the decay curve. The error ΔR is taken from the MINUIT [31] error of the corresponding fit parameter, NP is the number of points of the fit in each range and F is the number of degrees of freedom (NP $-$ 1).

the WILLI-97 experiment ($\Delta t = 20$ ns) and $f = 24$ MHz for the WILLI-98 experiment ($\Delta t = 41.67$ ns).

Additionally, the background estimated in the previous section is added to the exponential sum as a constant. Indirectly, another approach has been used for the analysis of both 97 and 98 experiments. Although the lifetime of the muons is recorded from $\approx$ 0.–5.12 μs there should be no systematic difference when fitting the decay curve only in parts of the time range (see also [32]). For instance, one could fix the end point of the fit at channel 128 in the time spectrum and shift the first point of the fit in the positive direction of the time axis, starting from channel 10 (400 ns). Without background subtraction, a systematic increase in the charge ratio R(μ^+/μ^-) is noticed. This can be related to the decreasing signal/noise ratio. A constant background (slope zero) in all the time range will force the fit to "look for" those components which participate in the total spectrum with smaller slopes, therefore the number of positive muons (largest mean lifetime, i.e. smallest slope) will be overestimated compared to that of negative muons. The "stability" for different fit intervals has been the criterion for choosing the value of the con-

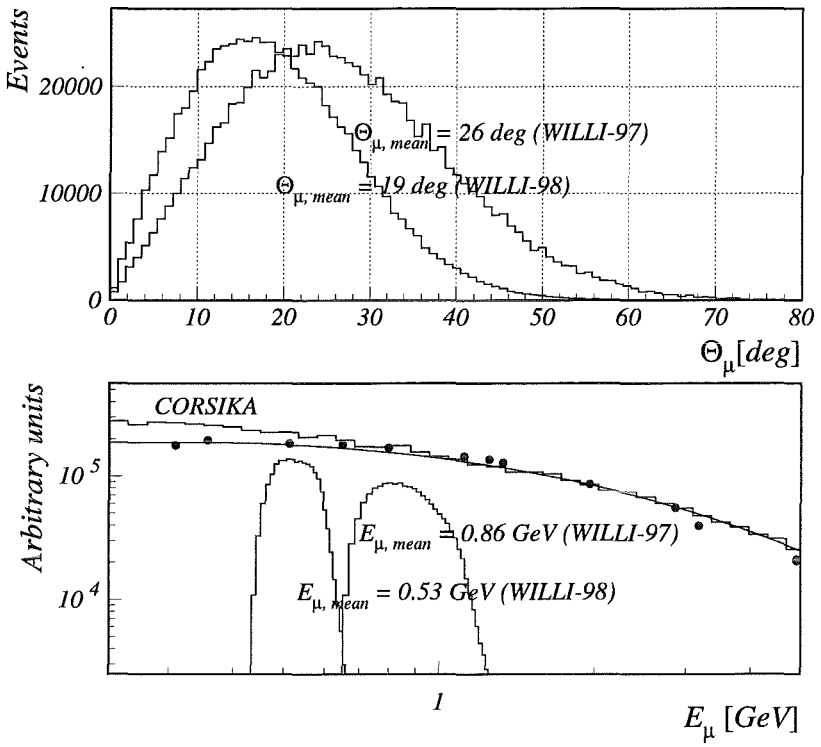

Fig. 3.20: Momentum and zenith angle distributions of accepted events. The measured intensity of the vertical muon flux used as input for the simulations is shown for comparison [30].

stant background. The background determined in this way is not far from the estimation by the 5 MHz measurements. In Table 3.1 results of the fit in different intervals for the WILLI-98 experiment are presented.

Once stability has been proved, the fit result using the maximum experimental information is taken, i.e. from the fit range 0.3 – 10.4 μs and the fit error is considered as statistical error of the measurement

$$R(\mu^+/\mu^-) = 1.27 \pm 0.01\,(\text{stat}) \qquad (\text{WILLI-98}).$$

The zenith angle and total energy of the muons above the building where the detector is located (the 60 cm shielding concrete) are taken from the simulation results to define the energy and zenith angle range (see Fig. 3.20).

In the WILLI-97 experiment [33, 34, 35], due to the stopping power of the additional absorbing material (lead plates and shielding), the measurement of

the muon charge ratio was done at a mean muon momentum of 0.86 GeV/c. The trigger geometry selected an acceptance solid angle with a mean zenith angle of 26°. The result of the fit was

$$R(\mu^+/\mu^-) = 1.30 \pm 0.05\,(\text{stat}) \qquad \text{(WILLI-97)}.$$

The experimental result depends strongly on the precision in calculating the efficiencies c_0, c_j. Therefore in the GEANT simulations the electromagnetic processes (Bremsstrahlung and δ-ray production by muons and electrons) have been simulated down to very low thresholds (100 keV), in order to have the right fluctuations and secondary particle yield. Muons and electrons have been tracked down to the same low energies. The agreement in the relative frequency of different event classes (see Fig. 3.19) sustains the correctness of these parameters.

The detector efficiencies calculated separately for each active module (selected by the stopping layer) are different. It has been shown in Fig. 3.19 that the simulated distribution of the stopping layer position is slightly different from the experimental one, this could induce a change in the calculated overall detector efficiency. Nevertheless, the main problem remains the precise calculation of the absorption and straggling in the environing building which houses the detector.

4. OVERVIEW ON MEASUREMENTS OF THE MUON CHARGE RATIO

Many experiments detecting muon intensities and the muon charge ratio have been performed over the last 5 decades. Most of them have been done in sites close to the sea level and only few ones at mountain altitudes [36, 37, 38]. In the last years compact balloon borne detector devices, developed originally for the detection of the primary cosmic ray, have been used to detect the muon spectrum during the rise and the descend of the balloon.

In most experiments the separation of positive and negative particles was performed by means of a magnetic field, historically first by solid iron magnetic lenses: two blocks of magnetised iron with opposite polarity orientation joined together, forming at their common frontier a magnetic lense which focuses alternatively positive and negative muons on a counter. Other experiments used cloud chambers in a magnetic field to measure the momentum of the particle [39]; the trigger was given by Geiger - Müller (GM) tubes for particles penetrating 10–15 cm of lead, in order to separate muons from the soft component. The tracking system has been improved by the development of new detector techniques and neon flash tubes or spark chambers were used to determine the deviation of the particle in the magnetic field, from the track pictures taken with stereoscopic cameras. Scintillators replaced the GM tubes in the trigger system and have been used for Time - of - Flight (TOF) and dE/dx measurements. Drift chambers and Multi - Wire - Proportional - Chambers (MWPC) replaced the photographic track determination and the identification of the particle has been improved by adding threshold detectors like Cherenkov counters or sampling calorimeters (for detecting electromagnetic showers induced by electrons).

The major problem of the measurements at low energies is the screening of the magnet iron core and the identification of the particle. The δ-ray production by muons and scattering in the magnet core are other sources of uncertainties. In modern detectors superconducting electromagnets are used,

where a strong magnetic field is obtained by a simple coil, with high intensity within a large volume. Depending on the spectrometer acceptance, values of the charge ratio can be obtained with such methods by measuring few hundreds of muons of each sign, during few hours or days. Measurements at different orientations are possible if the spectrometer is mounted in a mechanical device capable of rotation in vertical plane or both in the vertical and horizontal plane.

The other known method is the observation of the decay electrons from muons stopped in different materials as described in the previous chapters. Due to its simplicity it was used in early experiments, although at much lower performance than in recent arrangements. The main advantage compared to magnetic devices is the precise identification of the muon by its decay.

Magnetic spectrometers set a lower threshold in the detected particle momentum due to the size of the deflecting volume and a higher limit due to the precision in tracking. Results are generally reported by grouping muons in this range into several intervals of momentum. Experiments observing the change in the mean lifetime of muons stopped in matter define the range in the muon momentum only by the stopping power, proportional to the material and the volume of the absorber. This can be eventually shifted by placing a screening absorber on top of the detector, or by transporting it deep underground for high energy measurements.

A list of some experiments involving different methods is presented next. Each item shows the location of the experiment, a brief description of the detector (improved over the years from one experiment to another), the direction and the energy range of the detected muons. The name of the experiments and the year of the publication refers to the tables presented in Appendix B, where complementary information is presented (numerical values of the experimental points and of the geomagnetic cutoff - from the geomagnetic coordinates of the location [40]).

1. Chicago (USA); magnet cloud chamber, GM tubes, 10.2 cm lead shield; vertical; 0.17 – 10 GeV/c; Jones 1939 [39].

2. Chicago (USA); delayed coincidences, GM tubes, lead, graphite and sulphur absorbers, 15.2 cm lead shield; vertical; 0.28 – 0.39 GeV/c; Conversi 1950 [41].

3. Manchester (UK); magnet cloud chamber, GM tubes; vertical; 1 – 12 GeV/c, 5 – 1000 GeV/c; Owen 1951 [42] (Fig. 4.1), Holmes 1961 [43].

4. Melbourne (Australia); magnet, trays of GM tubes for tracking; EAST-WEST plane; 0.24 – 58 GeV/c; Moroney 1954 [11] (Fig. 4.1, 4.3).

5. Osaka (Japan); magnet cloud chamber, GM tubes; vertical; 0.24 – 22 GeV/c; Fukui 1955 [44] (Fig. 4.1).

6. Durham (UK); magnet, GM tubes, neon flash tubes for tracking; vertical; 5 – 1000 GeV/c, 10 – 450 GeV/c; Hayman 1962 [45], Ayre 1973 [62].

7. Nottingham (UK); magnet, GM tubes, neon flash tubes; EAST-WEST plane; 0.7 – 30 GeV/c, 2.34 – 360 GeV/c, 0.7 – 100 GeV/c, 3 – 360 GeV/c, 3 – 1000 GeV/c, 4 – 2000 GeV/c; Coates 1962 [47], Rastin 1965 [48], Judge 1965 [13] (Fig. 4.3), Baber 1968 [49], Appleton 1971 [50], Rastin 1984 [51] (Fig. 4.2).

8. Nagoya (Japan); magnet, scintillators, neon flash tubes; horizontal; 6.2 – 170 GeV/c; Kawaguchi 1965 [52].

9. Brookhaven (USA); magnet, scintillators, spark chambers for tracking; horizontal; 2 – 950 GeV/c; Kasha 1968 [54].

10. Kiel (Germany); magnet, GM tubes (later scintillators), spark chambers; EAST-WEST plane; 0.2 – 20 GeV/c, 0.3 – 25 GeV/c, 0.2 – 30 GeV/c, 0.3 – 26 GeV/c; Allkofer 1967 [55] (Fig. 4.3), Allkofer 1968 [56] (on the research vessel "Meteor", measurements at the Equator and at northern latitudes), Allkofer 1970 [57] (Fig. 4.2), Allkofer 1972 [58].

11. San Diego (USA); magnet, scintillators, wire spark chambers for tracking; EAST-WEST plane; 10 GeV/c –1.5 TeV/c; Burnett 1973 [59].

12. College Station (USA); magnet, scintillators, spark chambers; WEST, vertical; 2 – 50 GeV/c, 2 –1000 GeV/c; Bateman 1973 [60] (Fig. 4.4), Abdel-Monem 1973 [61].

13. Ahmedabad (India); delayed coincidences, scintillators, lead and graphite absorbers; vertical; 0.2 – 0.8 GeV/c; Singhal 1983 [63] (Fig. 4.2).

14. Palestine (USA); superconducting magnet, Cherenkov threshold detector, scintillators, MWPC, sampling calorimeter (lead and scintillator); vertical; 0.8 – 120 GeV/c; Stephens 1987 [64] (Fig. 4.2).

15. Kamioka (Japan), KAMIOKANDE (underground neutrino experiment); delayed coincidences, 2140 tons of ultrapure water as Cherenkov detector, 948 photomultipliers; all muons from 0^o to 90^o zenith angle; 1.2 TeV; Yamada 1991 [65].

16. Prince Albert (Canada); superconducting magnet, Cherenkov threshold detector, TOF system with scintillators, sampling calorimeter (brass and streamer tubes); vertical; 0.250 – 100 GeV/c; De Pascale 1993 [66] (Fig. 4.2).

17. Ft. Sumner (USA), Lynn Lake (Canada), HEAT (High Energy Antimatter Telescope), balloon borne; superconducting magnet, Transition - Radiation - Detectors (TRD), TOF system, drift tubes, sampling calorimeter (lead and scintillator); vertical; 0.3 – 0.9 GeV/c; Schneider 1995 [67], Tarlé 1997 [68].

18. Lynn Lake (Canada), IMAX (Isotope Matter Antimatter eXperiment), balloon borne; superconducting magnet, Cherenkov detectors, TOF, dE/dx scintillators, drift chambers, MWPC; vertical; 0.42 – 0.47 GeV/c; Krizmanic 1995 [69].

19. Ft. Sumner (USA), MASS2 (Matter-Antimatter Spectrometer System), balloon borne; superconducting magnet, Cherenkov detector, TOF system, drift chambers, MWPC, sampling calorimeter (brass and streamer tubes); vertical; 0.33 – 40 GeV/c; Basini 1995 [70] (Fig. 4.2).

20. Oxford (UK), KARMEN (neutrino experiment); delayed coincidences, 56 m^3 liquid scintillator, 2048 photomultipliers; predominantly vertical muons; 5.1 GeV/c; Grandegger 1993 [32], Jannakos 1995 [71].

21. Okayama (Japan); magnet, scintillators, MWPC; 0^o – 40^o zenith angle, 0^o – 360^o azimuth angle; 1.5 – 250 GeV/c; Tsuji 1998 [72] (Fig. 4.6).

Fig. 4.1 and 4.2 show results from experiments which measured several points below 10 GeV/c. Some experiments suggest that the charge ratio drops below 1 GeV/c (except De Pascale 1993 which has, nevertheless, very low errors).

In Fig. 4.3 results from measurements in the EAST - WEST plane are shown. The spectrometers were mounted in mechanical devices rotating around the geomagnetic NORTH - SOUTH direction, measuring the effect of

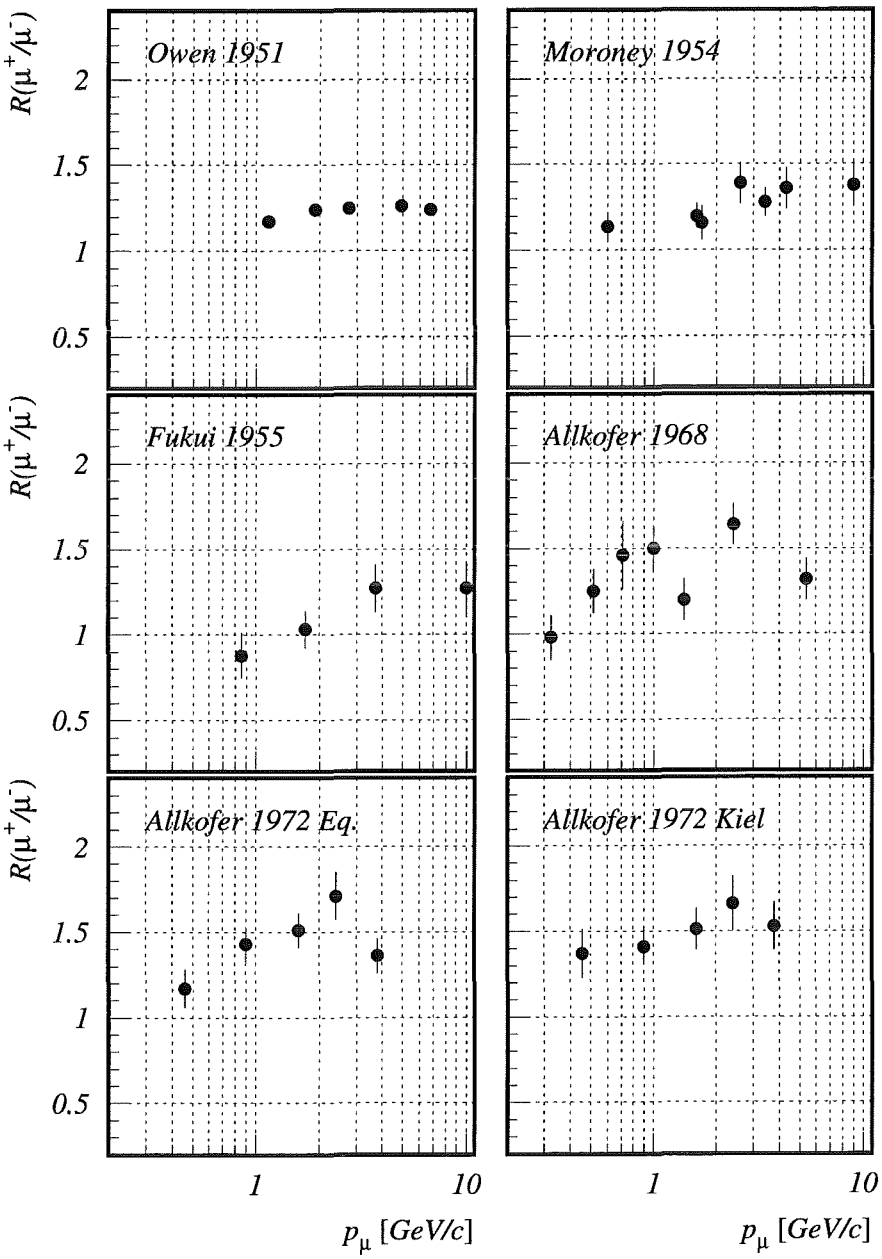

Fig. 4.1: Magnetic spectrometer measurements of the vertical muons charge ratio below 10 GeV/c. "Owen 1951" and "Fukui 1955" are cloud chamber experiments (from [11, 42, 44, 56, 58]).

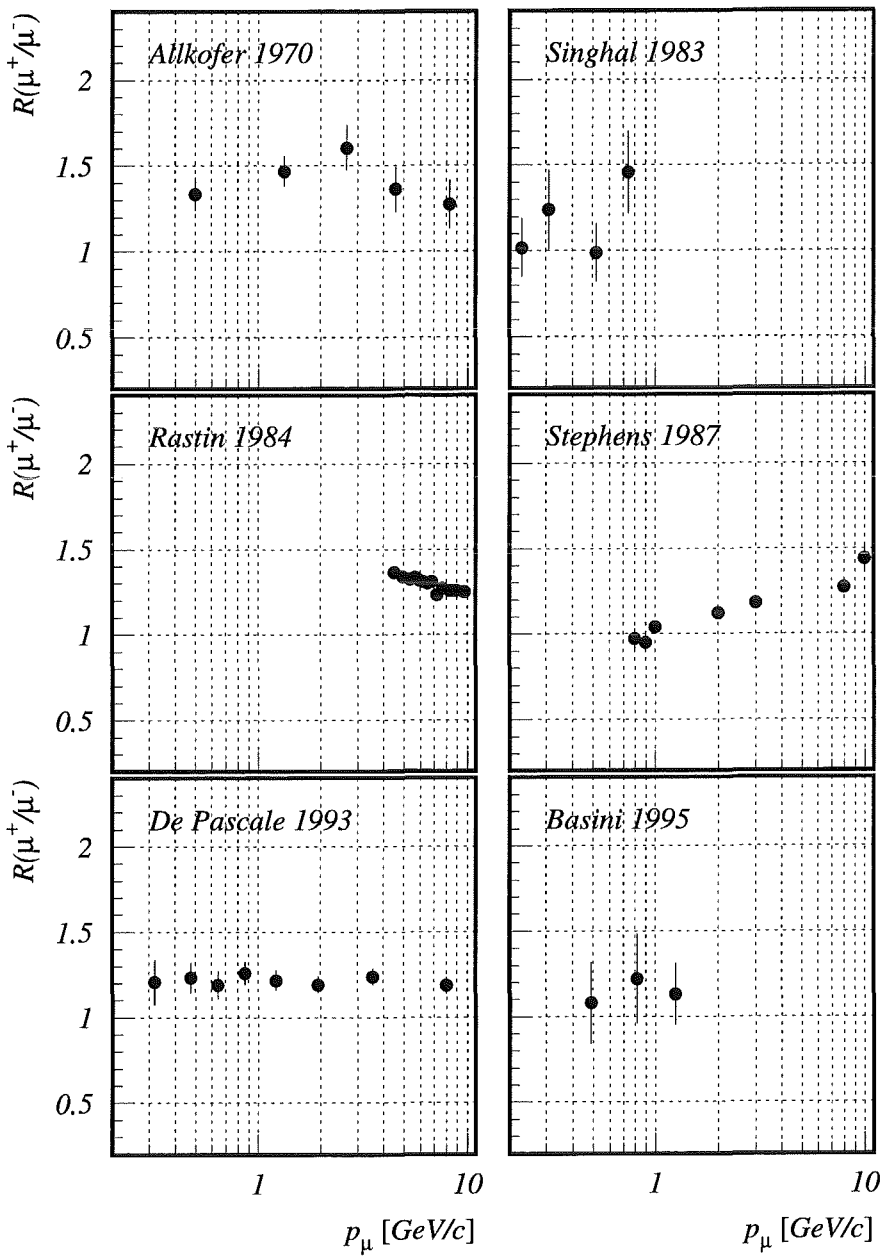

Fig. 4.2: Magnetic spectrometer measurements of the vertical muons charge ratio below 10 GeV/c. "Singhal 1983" is a delayed coincidences experiment (from [51, 57, 63, 64, 66, 70]).

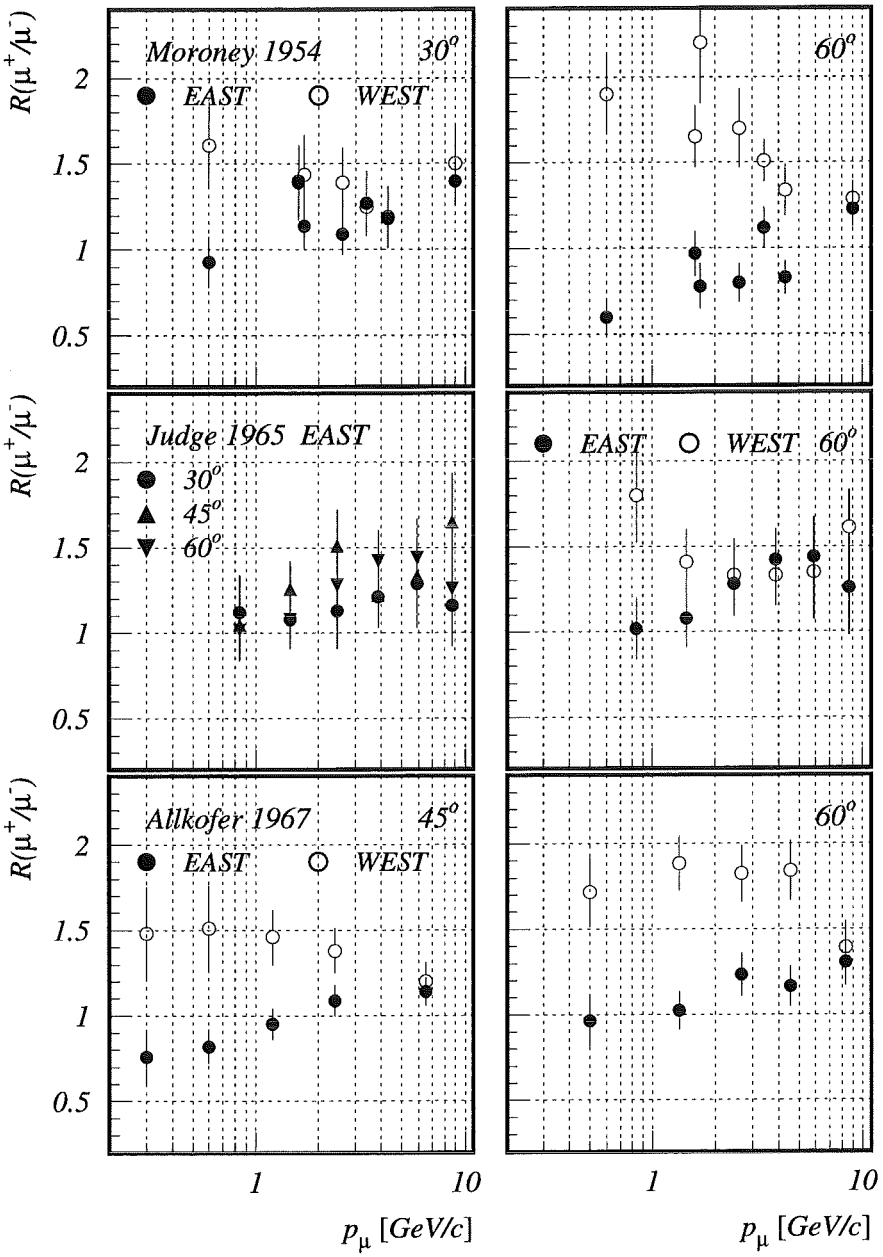

Fig. 4.3: Magnetic spectrometer measurements in the EAST - WEST plane at different zenith angles (from [11, 13, 55]).

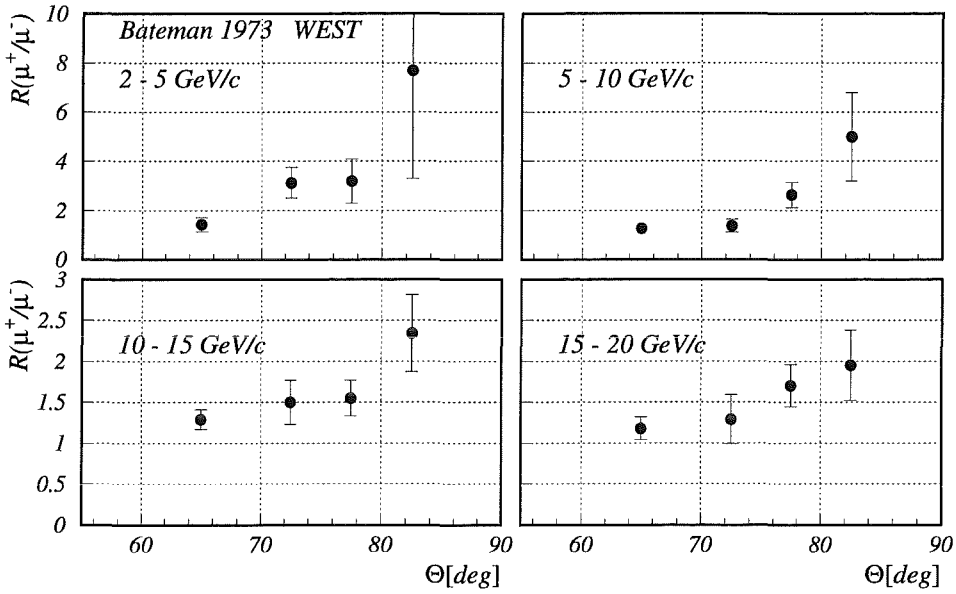

Fig. 4.4: Magnetic spectrometer measurements towards WEST at four zenith angles in the momentum range 2.5 – 3.5 GeV/c (from [60]).

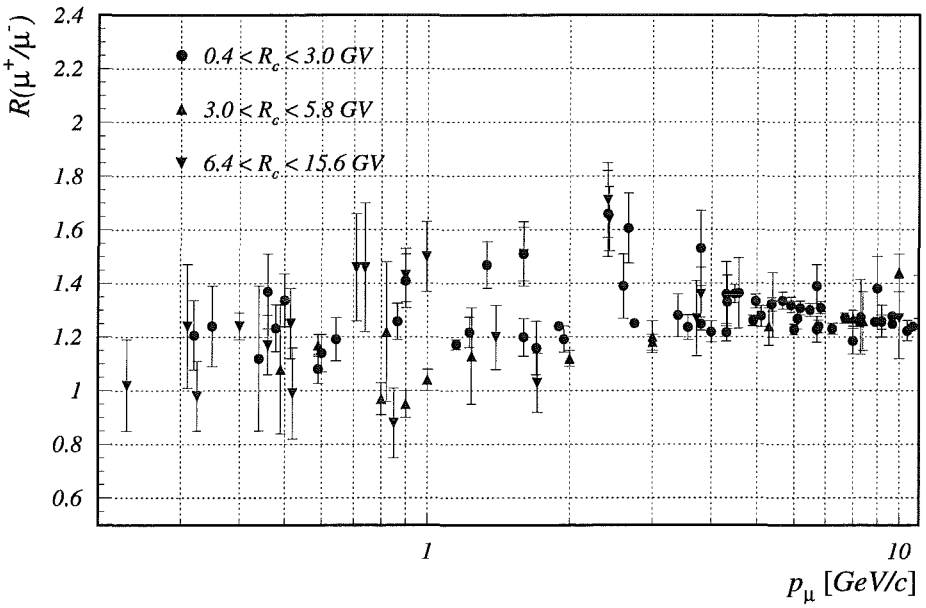

Fig. 4.5: Measurements of the vertical muons charge ratio classified after the geomagnetic cutoff of the experiment location (see list of references in Appendix B Table B.1).

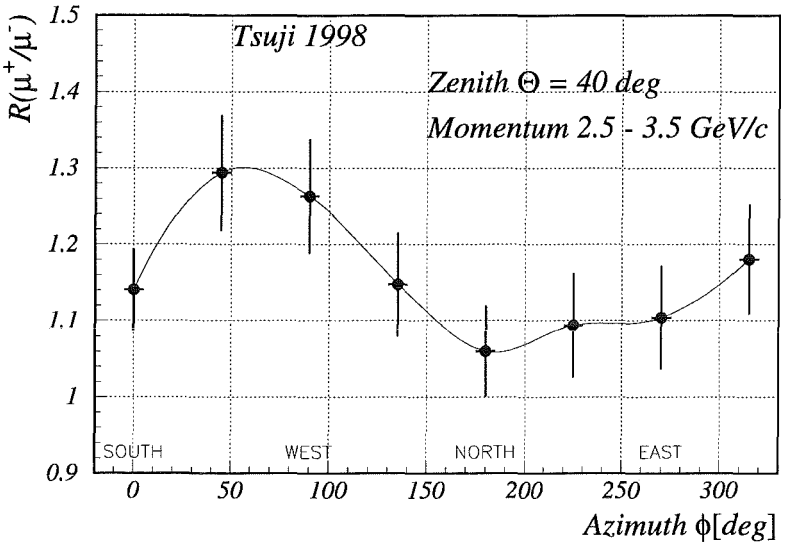

Fig. 4.6: Measurements with the OKAYAMA cosmic ray telescope [72] at fixed zenith angle and covering 360^o of azimuth.

the geomagnetic field on the positive and negative muons along their tracks. This results in observing a different charge ratio, the effect increases for lower muon momentum and for larger zenith inclination. The experiment "Allkofer 1967" shows very clearly the splitting point in the charge ratio at few GeV muon momentum.

Results from measurements of the charge ratio in four ranges of momentum and at four zenith angles towards the WEST direction are shown in Fig. 4.4. This experiment shows that the charge ratio increases for a fixed muon momentum with the zenith angle and this is more evident for low momentum muons.

Because of the geomagnetic influence, it is of interest to know the behaviour of muon spectra and charge ratio at different geomagnetic cutoff values. As can be seen in Fig. 4.5, the systematic errors between different measurements are larger than a possible sign of dependency on the geomagnetic cutoff. In one early experiment [41], measurements with a delayed coincidences device have been carried out near sea level and in an aircraft flying at different altitudes and latitudes. Another experiment ("Allkofer 1972" in Fig. 4.1) measured the charge ratio during a sea voyage at Equator

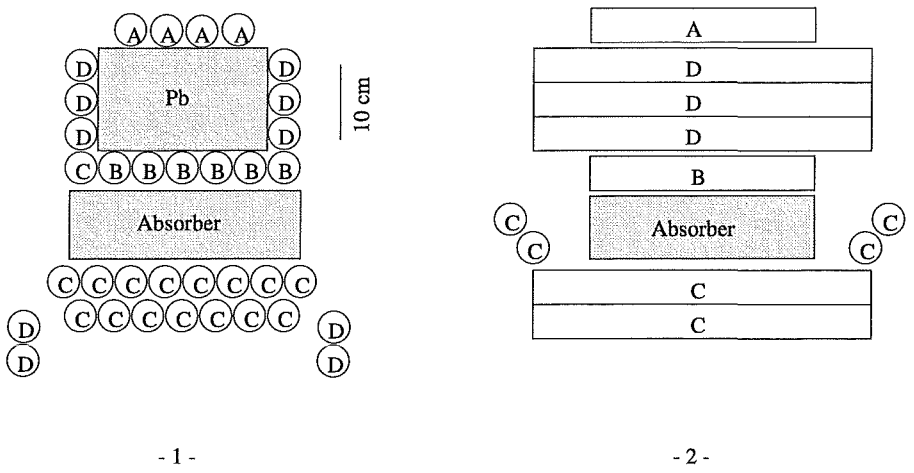

Fig. 4.7: Early experimental setup from the experiments of Conversi [41], using the delayed coincidences method. A, B, C, D are GM tubes. The absorber used was carbon or sulphur.

and at northern latitudes (Kiel).

Recent results from a magnetic spectrometer experiment have been reported (see Fig. 4.6), using data accumulated during 5 years, with muon fluxes and charge ratio azimuthal angular dependence, for the zenith angular range $0^o - 81^o$.

Historically the name of "delayed coincidences" has its origin in the conventional coincidence circuits used in the early experiments. Such a setup is show in Fig. 4.7 and was used by Conversi [41] in the late forties. The absorber was either graphite or sulphur. The delayed coincidences were registered by four channels, with time width of 2.8 μs and distance between of 0.98 μs. The minimum delay recorded was 1.15 μs. Measurements were performed in Rome, Chicago, at China Lake in California and on board of an B-29 aircraft in two expeditions from China Lake to Lima, Peru and to Fairbanks, Alaska. Different energy ranges were obtained by adding brass or concrete shieldings. In a practically unchanged configuration (except that the GM tubes were replaced by plastic scintillators) the experiment was remade by Singhal in 1983 [63].

The neutrino experiment KAMIOKANDE [65] measured the charge ratio of muons of 1.2 TeV/c (the detector is placed 1000 m underground) from the

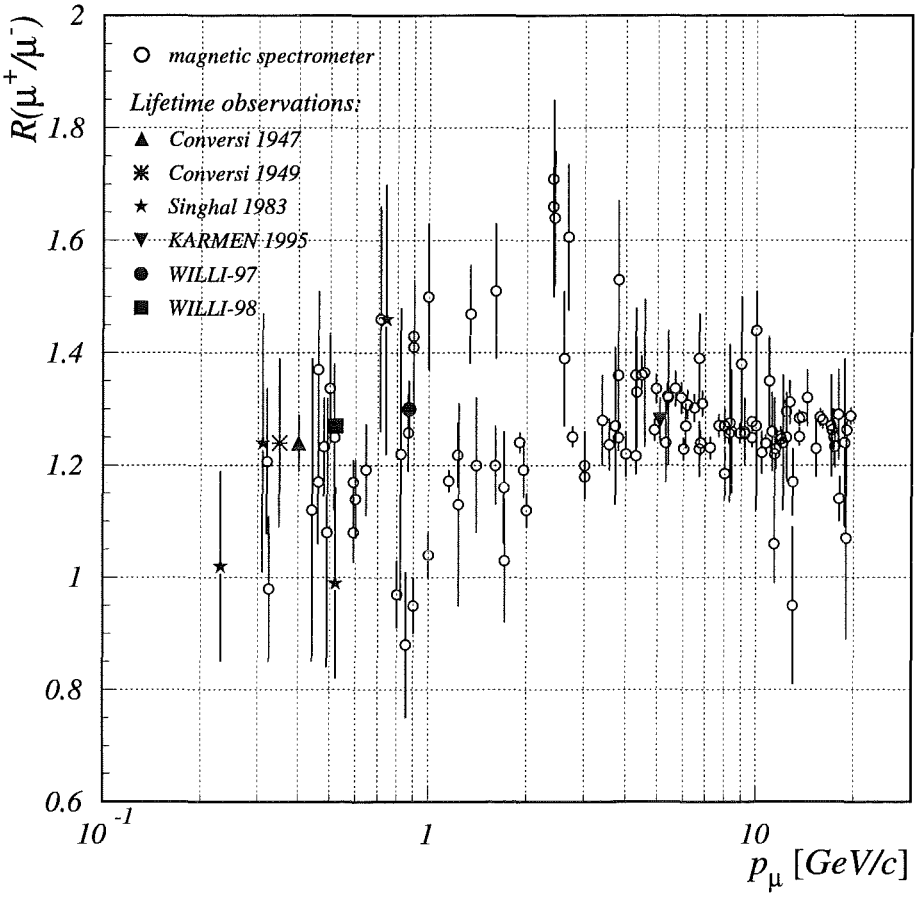

Fig. 4.8: Compilation of results on the charge ratio of vertical muons in the momentum range up to 20 GeV/c. Full symbols are results from delayed coincidences experiments (from [35, 41, 63, 71] and WILLI-98).

difference of the negative muons lifetime in oxygen (from the water Cherenkov detector). The data of 978 days of live detector time have been recorded in a time window from 0.9 to 20 μs with a time bin of 20 ns. The charge ratio was found to be $1.37 \pm 0.06(\text{stat}) \pm 0.01(\text{syst})$ for muons passing through the rock and arriving from a 2π solid angle. The KARMEN neutrino detector at the ISIS proton synchrotron (Rutherford Appleton Laboratory) used the negative muon capture in carbon (liquid scintillator) to determine the charge

ratio [32, 71]. The fit interval for the decay curve was 2 – 20 μs, with a time bin of 250 ns. The difference between the mean lifetime of negative muons and that of the positive muons is 402 ns in case of KAMIOKANDE and 171 ns for KARMEN. The corresponding difference of aluminium in the WILLI experiment is 1333 ns.

Fig. 4.8 compiles results of the muon charge ratio up to 20 GeV/c, but there are also measurements in the higher momentum range up to 10^5 GeV/c. While around 10 GeV/c the data appear in fair agreement, the picture is not clear below 4 GeV/c. Some measurements indicate that the ratio may drop below 1 at very low energies. This data collection as well as some individual experiments show a maximum between 2$\sim$3 GeV/c. Nevertheless the errors remain large for most of the measurements around 1 GeV/c and below. For magnetic spectrometers the statistical error of the result is given by the number of muons of both signs detected and measured and the acquisition time is proportional to the geometric acceptance of the spectrometer. This acceptance can be increased with the cost of powerful magnets (superconducting) but it remains many times smaller than that attainable with less expensive resources for a delayed coincidences detector.

The WILLI-97,98 results show within the limits of statistical errors a possible tendency in decreasing of the charge ratio towards lower energy, as some other experiments have already suggested. Nevertheless, further measurements with the same apparatus are necessary for lower energy at comparable statistics in order to decide on the behaviour of the charge ratio with the muon energy.

5. SIMULATIONS OF THE FLUX OF COSMIC RAY MUONS WITH THE MONTE-CARLO CODE CORSIKA

Calculations of the fluxes of cosmic ray particles in the atmosphere can be done in two ways:
- by solving a system of coupled diffusion equations (for different components) with primary cosmic flux parameters as boundary conditions on top of the atmosphere
- by Monte Carlo simulation of the "tree" of an extensive air shower (Fig. 1.1).
The identification of hadronic interaction effects requires a detailed modelling of the shower development by Monte Carlo methods, following each individual particle from production to destruction, decay or passage through the plane of observation and displaying the fluctuations arising from stochastic processes. CORSIKA (COsmic Ray SImulations for KAscade) simulates EAS initiated by photons, protons, nuclei or any other particle [73]. Different hadronic interaction models are available in CORSIKA. Present results have been obtained by coupling in CORSIKA (version 5.6) the low energy model GHEISHA [74] (interaction of hadrons below 80 GeV in air, laboratory energy) and the high energy model VENUS [75].

Primary cosmic ray spectra from recent measurements at the top of the atmosphere (Fig. 5.1) have been used in the energy range from 3 GeV to $\simeq$ 20 TeV, protons and neutrons, with incidence from vertical to $\theta = 70^o$. For nuclei heavier than protons, a superposition has been assumed. A total number of $5 \cdot 10^6$ primary protons and $5 \cdot 10^6$ neutrons have been simulated, in order to reproduce the fluxes of light and medium cosmic rays (p, α and the C,N,O group) and isotropic distribution of the incoming particles at the top of the atmosphere has been assumed. A constant magnetic field is considered when tracking the particles in the atmosphere. This field has the values set in CORSIKA as specified in the user manual [83] from a cited

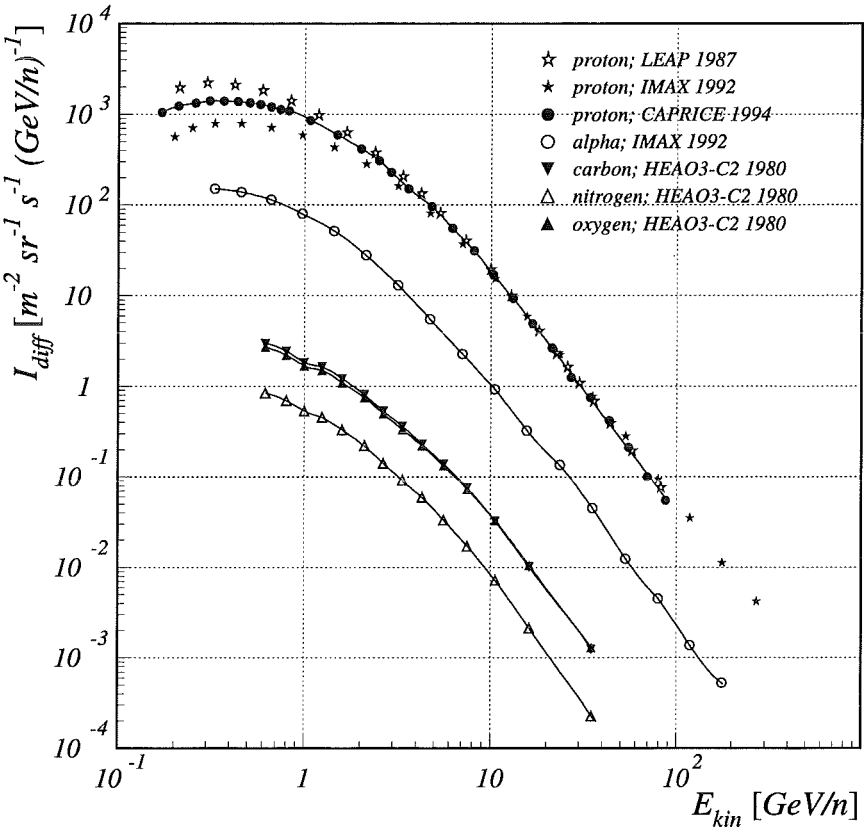

Fig. 5.1: Differential energy spectra of primary cosmic particles measured on top of the atmosphere by HEAO3 [76], CAPRICE [77], IMAX [78] and LEAP [79] experiments. Three measurements of the proton flux at different solar epochs are shown; solar modulation is seen at the lower part of the spectrum (< 3 GeV). Above the highest measured energy a decreasing power with index -2.7 is considered.

source. Calculations show for the location of the WILLI experiment values of the magnetic field components close to those for the KASCADE location.

The maximum muon yield is somewhere between 20 and 30 GeV/nucleon in the primary spectrum (Fig. 5.2). The muons for analysis have been collected in the momentum range 0.23 to 1000 GeV/c. The zenith angular dependence of the muon intensity is in good agreement with $\cos^2\theta$ down to

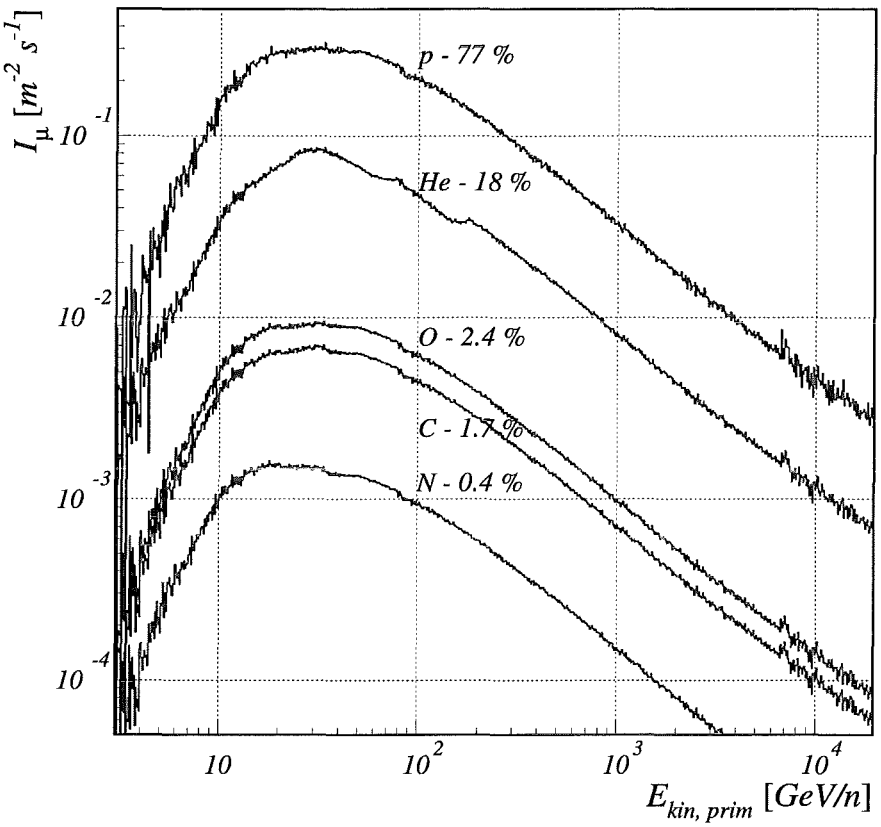

Fig. 5.2: Muon yield (in flux value I) from different primary particles. The maximum yield is between 20 and 30 GeV/nucleon. Percentage from the total muon flux is shown.

$\theta = 60^o$ (Fig. 5.3). For more horizontal calculations the effect of the curvature of the Earth becomes important. In order to compare the simulations with vertical measurements, muons with θ from 0^o to 10^o have been selected (Fig. 5.4). In case of inclined measurements, muons from the simulations have been collected inside a solid angle defined by $\pm 5^o$ both in the zenith and azimuth plane, around 30^o, 45^o and 60^o zenith angle (Fig. 5.5 and 5.6). Because in the maximum muon yield range of the energy per nucleon only a small percentage of the primary particles produces enough muons to be recorded at the observation level, the various simulated spectra show rather large fluctuations, especially in the low energy part.

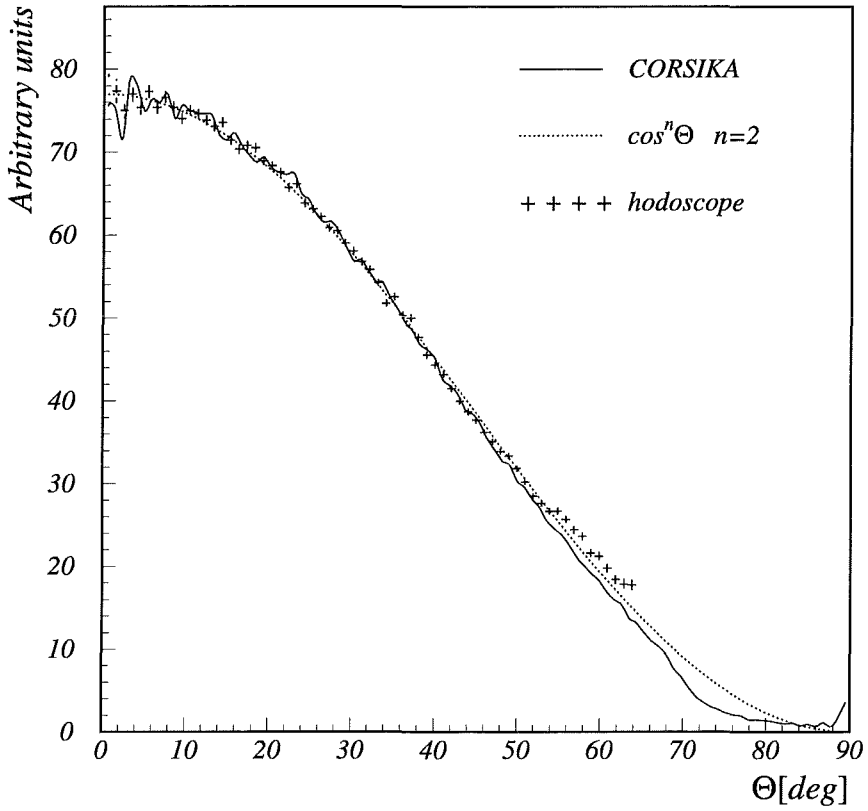

Fig. 5.3: Directional intensity of muons simulated with CORSIKA (plane atmosphere model) compared with a $\cos^2(\theta)$- distribution and a measurement with a MWPC hodoscope [12].

The charge ratio is obtained by dividing the positive and the negative muon spectra. Due to the poor statistics, the fluctuations become even larger. Fig. 5.7 shows the calculated charge ratio, which is obviously below most of the experimental points at low energy. CORSIKA handles the tracking in the Earth's magnetic field, therefore the EAST-WEST effect is well reproduced (Fig. 5.8), although data belong to experiments performed on locations with different geomagnetic cutoff.

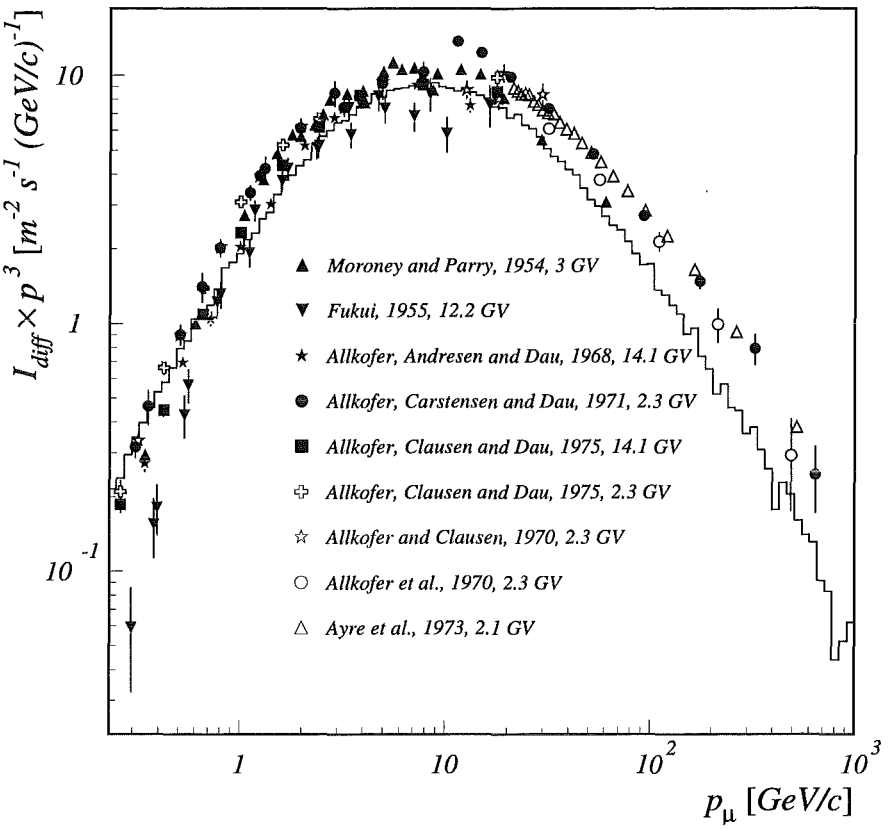

Fig. 5.4: Vertical intensity of muons simulated with CORSIKA (histogram) compared with measurements with magnetic spectrometers [11, 30, 44, 46, 56, 57, 80, 81] (local geomagnetic cutoffs in vertical direction are shown in GV). The intensity values are multiplied by p^3 in order to distinguish better different experimental points. At higher energies the muon deficit in the simulations is due to the limit of 20 TeV in primary particle energy range for the calculations.

5.1 Hadronic interaction models for muon simulations

The simulated muon fluxes presented above are the sum of the positive and negative muons. Their values are calculated absolutely by the model from the input primary flux. Therefore, a too low pion production could be compensated by a higher primary flux. The muon charge ratio is more sensitive to

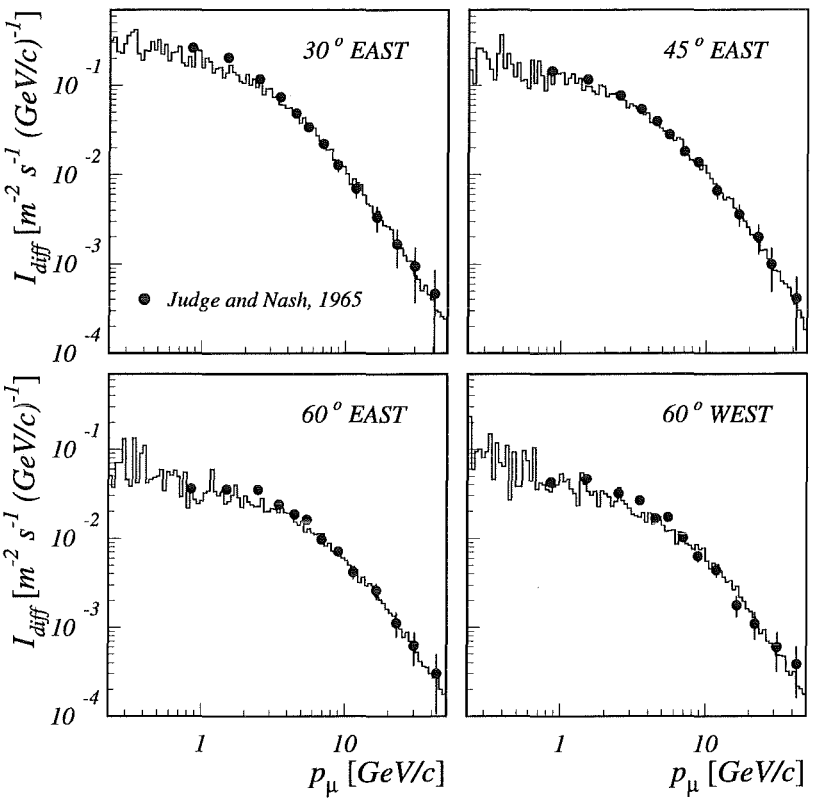

Fig. 5.5: Inclined intensity of muons simulated with CORSIKA (histogram) compared with measurements with magnetic spectrometers [13].

the details of the hadronic interaction model, when it is propagated through the EAS down to the observation level and it is less subject to the primary flux scaling.

In the propagation of an EAS, the energy of the primary particle is distributed in each step over a number of secondaries, therefore a particle starting in the range where the high energy hadronic interaction model treats the collision with air nuclei produces after some interactions secondary hadrons with energies below the limit set between the two models. When the energy per nucleon of the primary particles is limited to an upper value of 80 GeV, the low-energy interaction features are selected only. Such analysis shows that the low-energy model (GHEISHA) has problems in simulating the right

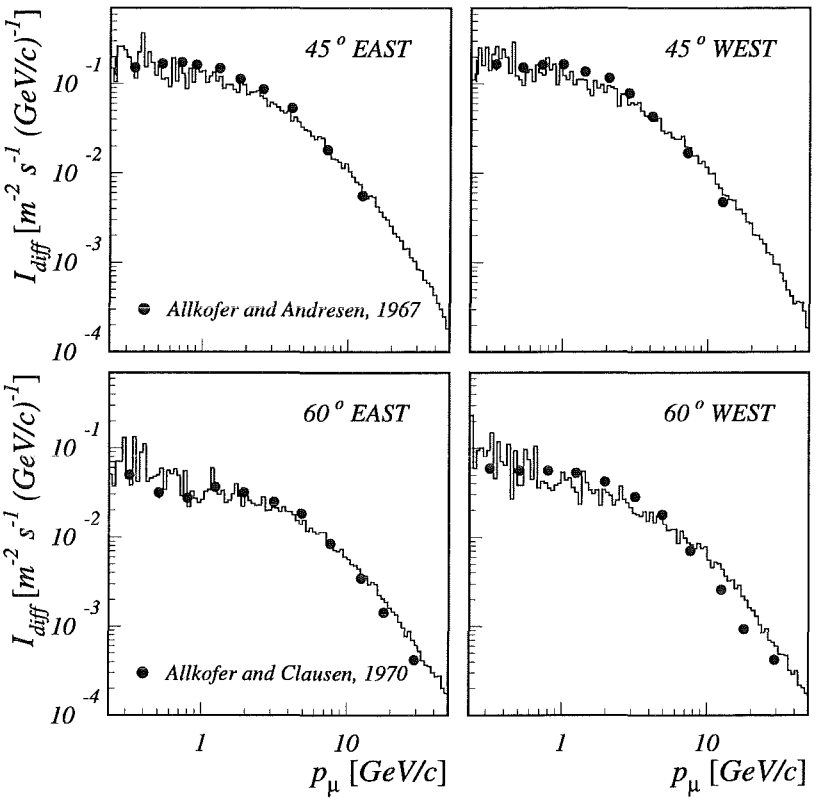

Fig. 5.6: Inclined intensity of muons simulated with CORSIKA (histogram) compared with measurements with magnetic spectrometers [55, 57].

muon charge ratio and possibly the absolute value of the muon flux in the frame of an EAS simulation code (low energy muon detector multiplicity disagreement has been reported by groups in KASCADE). Using CORSIKA it is not possible to isolate in the same way the high energy part (VENUS) of the hadronic interactions in an EAS. A comparison can be made if an interaction test version is used to investigate one single interaction at a time.

In [82] the GEANT versions of GHEISHA and FLUKA are compared in many aspects. A comparison of GHEISHA and VENUS, using an interaction test version of CORSIKA, shows completely unphysical behaviour of GHEISHA and serious problems in charge conservation. GHEISHA is a non-microscopic code, it does not try to simulate the physical processes that

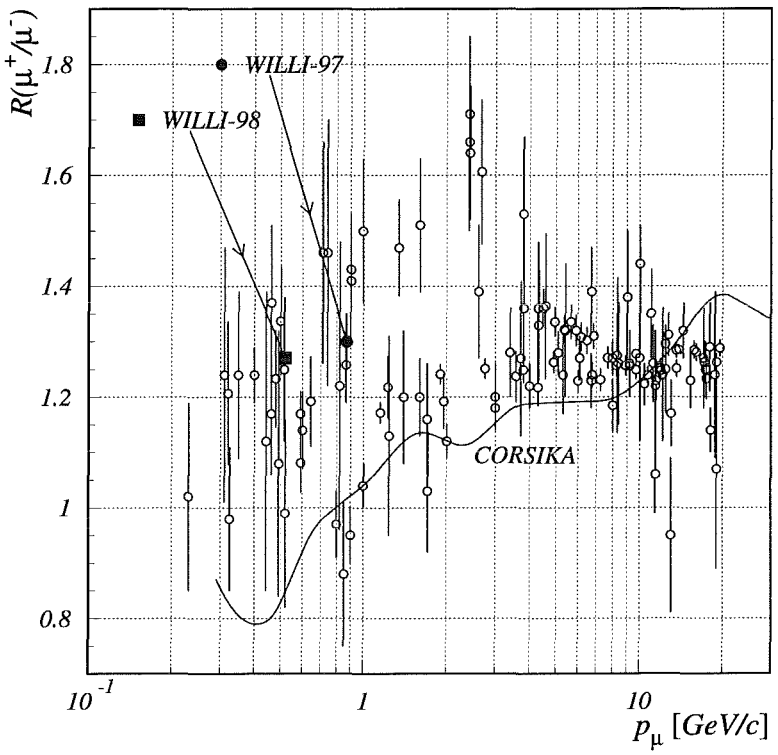

Fig. 5.7: The muon charge ratio in the vertical direction from measurements (see previous chapter) and calculated by using CORSIKA (continuous line).

determine the hadron-nucleon or hadron-nucleus reaction dynamics, it tries instead to reproduce directly the outcome of the reaction. Such a model generates secondary particles by hadron-nucleus interactions in order to satisfy scaling laws, symmetry requirements and to reproduce experimental inclusive distributions and calorimetric data. VENUS is a microscopic model and FLUKA uses a QCD inspired parametrisation, where the incident nucleon produces an intranuclear cascade of secondary particles which reinteract inside the nuclear matter. The models differ in the way hadron-hadron scattering is described (the Dual Parton Model in FLUKA and the Pomeron exchange in VENUS).

The next figures show results from tests at fixed energy with VENUS

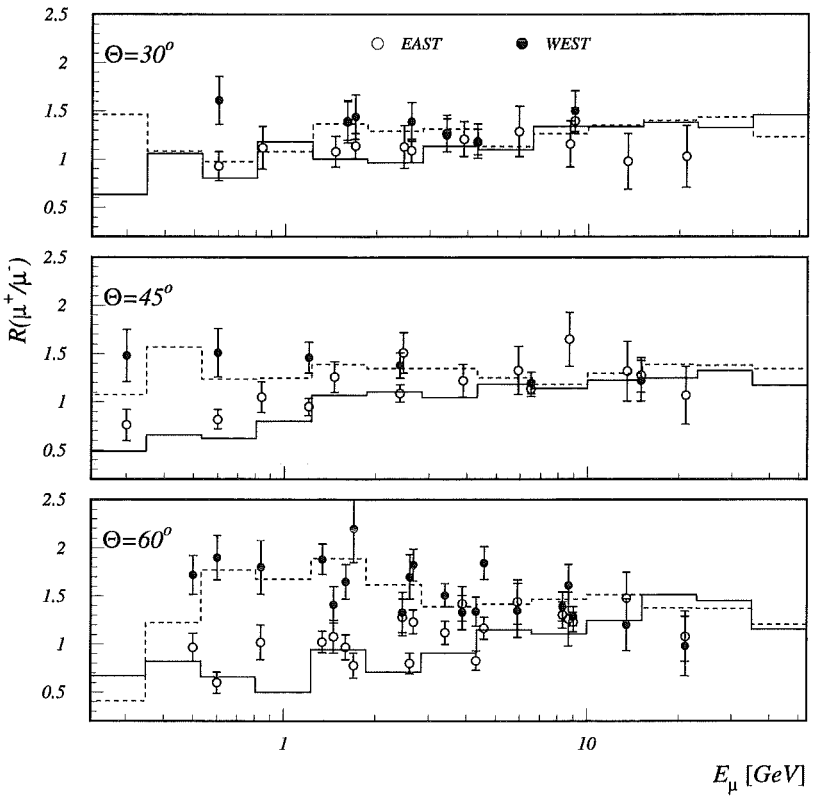

Fig. 5.8: The muon charge ratio at 30^o, 45^o and 60^o. The splitting effect (EAST-WEST) is well reproduced by the CORSIKA simulations (histogram) as compared with the experimental points [11, 13, 55, 57].

(from CORSIKA) and FLUKA (from GEANT). The two programs are initialised as follows:

1. GEANT

   - the FLUKA package is selected for tracking hadrons,
   - protons and neutrons of 80 GeV (laboratory) are targeted in a volume filled with air,
   - after the first hadronic interaction the tracking stops,

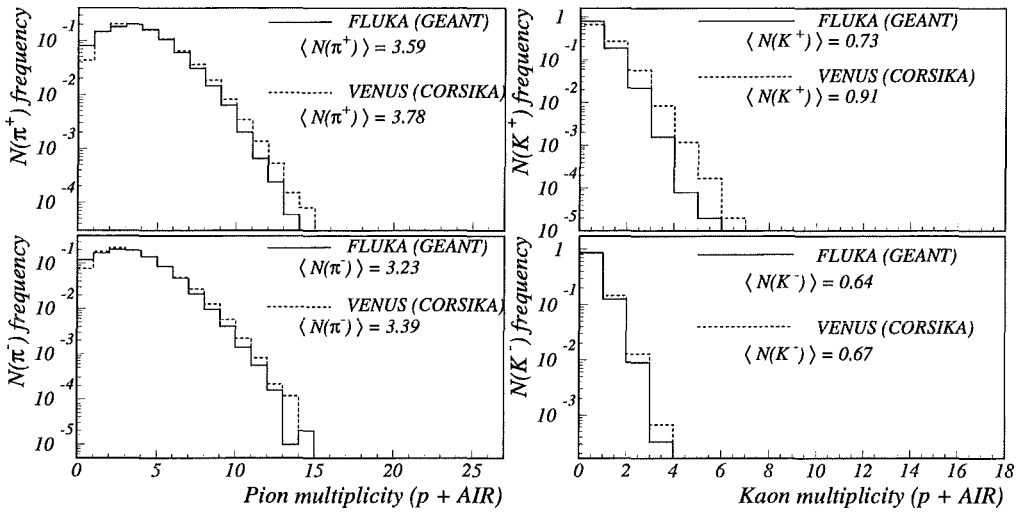

Fig. 5.9: Positive and negative pions and kaons multiplicity distributions in $(p + Air)$ collisions, from FLUKA and VENUS tests using GEANT and CORSIKA, at 80 GeV laboratory energy. The mean value of the multiplicity is indicated.

- low energy cuts are set to 3 MeV for electrons and photons and 50 MeV for muons and hadrons,
- only secondary particles from the forward hemisphere are written out.

2. CORSIKA (see the user manual [83])

   - protons and neutrons of 80 GeV (laboratory) are used,
   - the high-to-low energy border in the CORSIKA code is changed to 79 GeV, for the high energy model VENUS to treat the collision, or to 81 GeV, when the projectile energy falls in the low-energy range treated by GHEISHA,
   - the first interaction point is forced at the upper boundary of the atmosphere,
   - the observation level is placed 1 cm below the interaction point; in this limit only one interaction of the projectile with an air nuclei occurs,

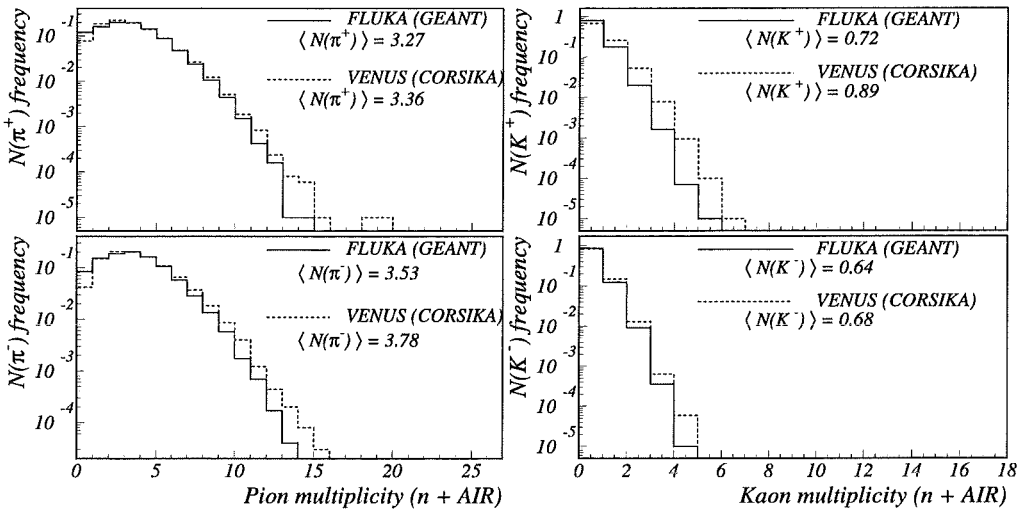

Fig. 5.10: Positive and negative pions and kaons multiplicity distributions in $(n+Air)$ collisions, from FLUKA and VENUS tests using GEANT and CORSIKA, at 80 GeV laboratory energy. The mean value of the multiplicity is indicated.

- energy cuts have the same values as in the GEANT simulations.

For each model 10^5 protons and 10^5 neutrons have been simulated. All kinematic parameters of the secondary particles were stored. Fig. 5.9, 5.10, 5.11, 5.12 and 5.13 show multiplicity, energy spectrum of positive and negative pions and kaons and their charge ratio. It is noticed that in FLUKA the production of each meson charge is done with multiplicities slightly lower than in VENUS. The mean charge excess (the difference between the number of positive and negative mesons produced in one collision) has the values

	FLUKA	VENUS
$p + Air \rightarrow \pi$	0.88	0.89
$n + Air \rightarrow \pi$	0.22	0.07
$p + Air \rightarrow K$	0.84	1.11
$n + Air \rightarrow K$	0.81	1.06

The positive charge excess seen in this interaction test propagates in the atmosphere and gives a muon charge ratio larger than unity. At this fixed

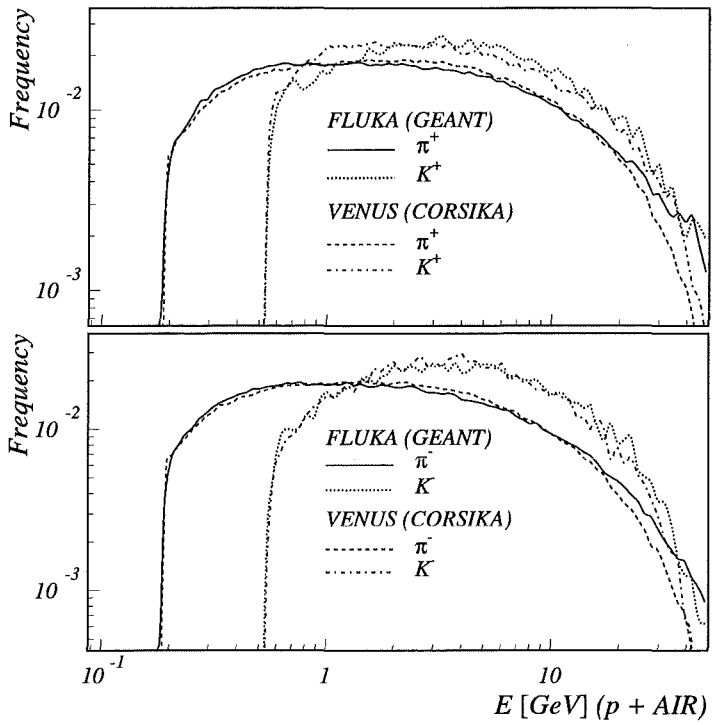

Fig. 5.11: Energy spectrum (kinetic energy) of positive and negative pions and kaons produced in $(p + Air)$ collisions from FLUKA and VENUS tests using GEANT and CORSIKA, at 80 GeV laboratory energy.

energy the total number of kaons in the simulations set is about 10 times smaller than the number of pions.

By dividing the energy spectra from Fig. 5.11 and 5.12, the charge ratio spectra of pions and kaons are obtained in Fig. 5.13. There is a good agreement between the two models in the pion charge ratio, but FLUKA produces a lower kaon charge ratio, although higher than one. The pion production is charge symmetric at lower energy (the charge ratio is one) and it becomes asymmetric as the energy increases, towards values greater than one for incident protons and smaller than one for neutrons, respectively.

This brief analysis supports the idea of coupling the two interaction models (FLUKA for low energy and VENUS for high energy) in a simulation code

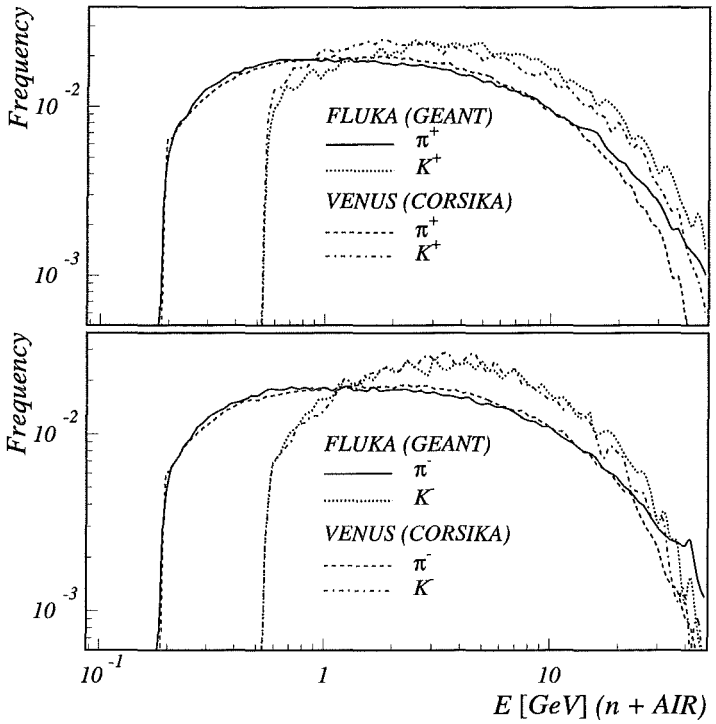

Fig. 5.12: Energy spectrum (kinetic energy) of positive and negative pions and kaons produced in $(n + Air)$ collisions from FLUKA and VENUS tests using GEANT and CORSIKA, at 80 GeV laboratory energy.

like CORSIKA, where the WILLI results can be used for a calibration of the simulations. Atmospheric neutrino calculations can be made further, for the purposes presented in the introduction, on the basis of a good reproduction of the cosmic ray muon data.

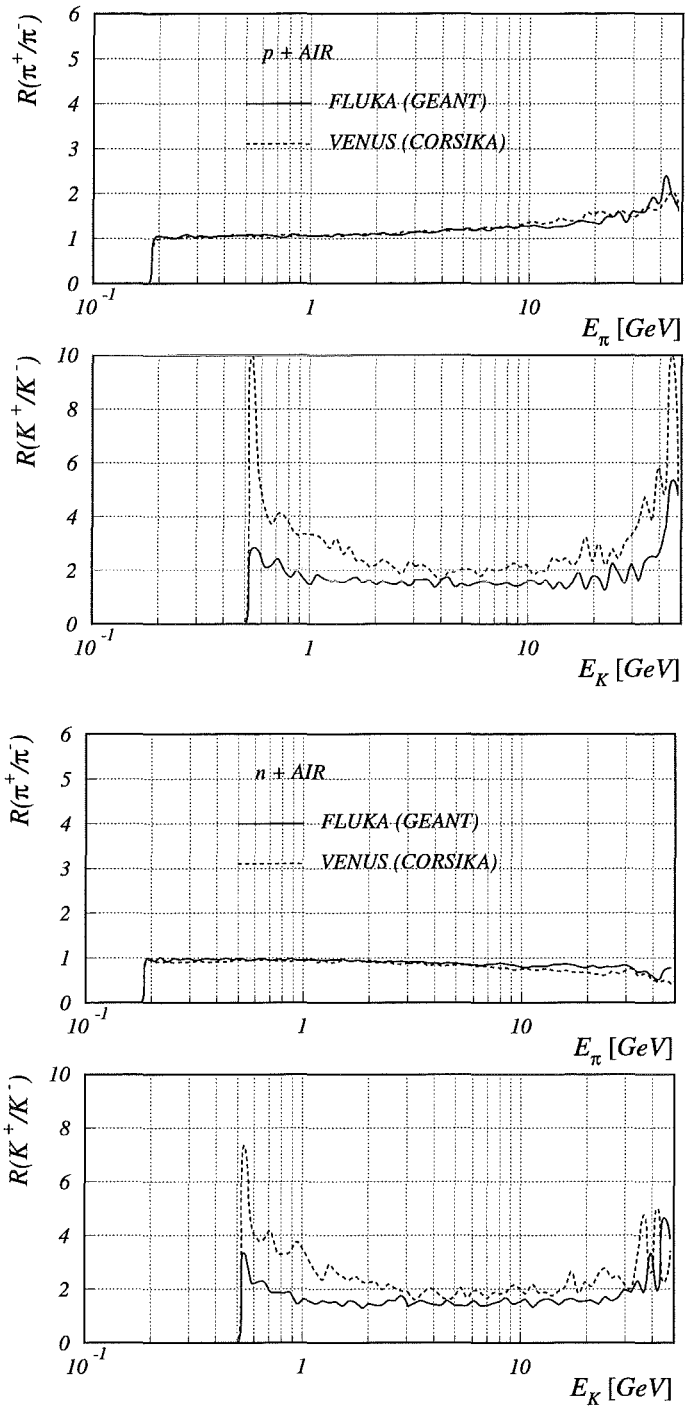

Fig. 5.13: Charge ratio of pions and kaons produced in $(p + Air)$ and $(n + Air)$ collisions from FLUKA and VENUS tests using GEANT and CORSIKA, at 80 GeV laboratory energy.

6. CONCLUSIONS

In the present work a method for the determination of the charge ratio in the atmospheric muon flux by observing the different lifetimes of negative and positive muons stopped in matter has been experimentally worked out, with setting up and studying the performance of a compact muon calorimeter (WILLI). Due to the nuclear capture, negative muons stopped in the absorber material (finally using aluminium as optimal absorber) appear with a considerably reduced effective lifetime as compared to the free decay of positive muons. The average life time of muons in the flux which contains both charges is observed with simple timing electronics detecting the delayed decay electrons. The method and the detector device avoid various difficulties of methods using large (and expensive) magnetic spectrometers, which suffer from small acceptances and uncertainties of the different efficiencies for positive and negative muon detection and leads to accurate results. Methodical aspects and the technical design of the apparatus have been already published [35].

In two measurement runs: WILLI-97 and WILLI-98 the charge ratio has been determined at two different muon momenta below 1 GeV/c:

$$R(\mu^+/\mu^-) = 1.30 \pm 0.05\,(\text{stat})$$

for muons of 0.86 GeV/c of vertical incidence (mean zenith angle 26^o) and

$$R(\mu^+/\mu^-) = 1.27 \pm 0.01\,(\text{stat})$$

for muons of 0.52 GeV/c of vertical incidence (mean zenith angle 19^o).

Experimental information about the atmospheric muon fluxes and their charge ratio, especially in the low energy region, for which reliable data are scarce, is of interest due to the relation to the atmospheric neutrino anomaly [84], verified recently by the results of the Super - Kamiokande experiment [85] and currently considered as clear evidence for neutrino oscillations. The muon charge ratio reflects directly the ratio of electronic neutrinos and an-

tineutrinos. Since the (charged current) interactions of neutrinos and antineutrinos with matter are different, the efficiency of neutrino detectors installed in underground laboratories have to be correspondingly calibrated.

In addition, as detailed calculations show, the muon charge ratio is a sensitive test quantity for controlling the hadronic interaction models which are used as generators for Monte Carlo simulations of the neutrino fluxes, whose predictions establish the observed atmospheric neutrino anomaly and play the central role in resolving the oscillation puzzle, i.e. what flavour is the partner for the muonic neutrino.

Under these aspects the existing experimental data have been analysed by calculations of the muon fluxes and of their charge ratio, using the simulation code CORSIKA, comparing various hadronic interaction models currently en vogue for many studies and included in the worldwide used detector simulation package GEANT (version 3.21) of the CERN library. The study of the phenomenological approach GHEISHA, applied for lower primary energies, reveals major problems in the physical description of the hadronic interaction observables and there are obvious disagreements between data and simulations. An alternative interaction model FLUKA is based on QCD inspired descriptions of the interaction variables. With an accessible version it has been compared with the VENUS model for single (p+air) and (n+air) interactions at 80 GeV laboratory energy (interaction test). The pion and kaon multiplicity distributions, the mean charge excess, energy spectra and the muon charge ratio show a good agreement of the two models. Actually FLUKA has not been used as generator of the Monte Carlo code CORSIKA, with which the quality of the model could be further tested by means of the muon charge ratio. The presented results, however, have specified the deficiencies of the used hadronic interaction models at low energies. Such problems in the range of accelerator energies, just revealed by the muon charge ratio data, appear in fact slightly surprising and there is an urgent need for clarification with respect to the reliability of EAS simulation predictions, at all.

In preparing of the analyses in the light of Monte Carlo simulations in this thesis the present status of muon charge ratio studies has been reviewed with a compilation of the experiments communicated in the literature. The East-West effect displaying a difference of the muon charge ratio in both directions [86] is illustrated. Possible source of systematic uncertainties in comparing different results is the influence of the geomagnetic cutoff, but significant effects have not been observed.

In addition to the relation to the atmospheric neutrino fluxes and the view on hadronic interaction models for the GeV-TeV region, the investigation of the charge ratio of atmospheric muons displays further interesting aspects. Anticipating the correctness of the interaction model used in the EAS simulations, the average neutron to proton ratio in the mass composition of cosmic rays could be determined [87, 88] (see Apendix C). The geomagnetic field affects the trajectories of positive and negative muons differently and leads to separation effects which may give information about the production height of the muons [89]. Actually geomagnetic influences have never been systematically explored with measurement in different sky directions, which may provide interesting geophysical perspectives, especially if correlated with other geophysical observations (variations of the Earth's magnetic field and solar activities). With such perspectives of a systematic "muon charge ratio spectroscopy" the layout of the WILLI detector is forseen for a modification with a rotatable setup to be directed as a "telescope" in various azimuthal and zenithal directions [72].

BIBLIOGRAPHY

[1] G.V. Kulikov, G.B. Khristiansen, Soviet Physics JETP 358 (1959) 441.

[2] K. Boothby et al., Nucl. Phys. B, Proc. Suppl. 52B (1997) 166.

[3] H. Rebel, Proc. 15th Cracow Summer School of Cosmology "The Cosmic Ray Mass Composition", Lodz, Poland, July 15-19 1996, Ed. W. Tkaczyk, p. 91.

[4] I.M. Brâncuş, B. Vulpescu, H. Rebel, M. Duma, A.A. Chilingarian, Astropart. Phys. 7 (1997) 343.

[5] The KASCADE collaboration, Nucl. Phys. B, Proc. Suppl. 75A (1999) 234.

[6] The CASA-MIA collaboration, Nucl. Phys. B, Proc. Suppl. 75A (1999) 241.

[7] The HEGRA collaboration, Nucl. Phys. B, Proc. Suppl. 75A (1999) 244.

[8] M. Aglietta et al. (EAS-TOP), Nucl. Phys. B, Proc. Suppl. 75A (1999) 251.

[9] G. Schatz et al. (KASCADE collaboration), Nucl. Phys. B, Proc. Suppl. 60B (1998) 151.

[10] O.C. Allkofer, P.K.F. Grieder, Physics Data 25-1, 1984, Fachinformationszentrum Energie - Physik - Mathematik GmbH, Karlsruhe.

[11] J.R. Moroney, J.K. Parry, Austral. Journ. Phys. 7 (1954) 424.

[12] J. Wentz, FZKA Report 5500, Forschungszentrum Karlsruhe, 1995.

[13] R.J.R. Judge, W.F. Nash, Nuovo Cimento 35 (1965) 999.

[14] The Super - Kamiokande collaboration, Phys. Rev. Lett. 81 (1998) 3319.

[15] T.K. Gaisser, T. Stanev, G. Barr, Phys. Rev. D 38 (1988) 85.

[16] P. Lipari, Astropart. Phys. 1 (1995) 195.

[17] M. Honda, T. Kajita, K. Kasahara, S. Midorikawa, Phys. Rev. D 52 (1995) 4985.

[18] B.C. Barish, Nucl. Phys. B, Proc. Suppl. 38B (1995) 343.

[19] The Super - Kamiokande collaboration, Talk at 8th International Workshop on Neutrino Telescopes, Venice, February 23 – 26 1999.

[20] The Particle Data Group, Phys. Rev. D 50 (1994) 1173.

[21] J.A. Wheeler, Mod. Phys. 21 (1949) 133.

[22] N.C. Mukhopadhyay, Phys. Lett. C 30 (1977) 1.

[23] T. Suzuki, D.F. Measday, Phys. Rev. C 35 (1987) 2212.

[24] R.P. Kokoulin, A.A. Petrukhin, Nucl. Instr. Meth. A 263 (1988) 46.

[25] I.M. Brâncuş et al., Rom. Journ. Phys, 40 (1995) 981.

[26] I.M. Brâncuş et al., Balk. Phys. Lett. 4 (1996) 54.

[27] I.M. Brâncuş, M. Duma, B. Vulpescu, Internal Report Kernforschungszentrum Karlsruhe, 1995, unpublished.

[28] I.M. Brâncuş, M. Duma, J. Oehlschläger, B. Vulpescu, Internal Report Kernforschungszentrum Karlsruhe, 1994, unpublished; MUONLM, NEA-1475, NEA Data Bank 1995.

[29] GEANT - CERN Program Library Long Writeup W5013, 1994.

[30] O.C. Allkofer, K. Carstensen, W.D. Dau, Phys. Lett. B 36 (1971) 425.

[31] MINUIT 94.1- CERN Program Library Long Writeup D506, 1994.

[32] W. Grandegger, KfK Report 5122, Kernforschungszentrum Karlsruhe, 1993.

[33] B. Vulpescu et al., Nucl. Phys. B, Proc. Suppl. 52B (1997) 195.

[34] B. Vulpescu et al., International Research Workshop "Heavy Ion Physics at Low, Intermediate and Relativistic Energies using 4π Detectors", Poiana Braşov, Romania, Eds. M. Petrovici, A. Săndulescu, D. Pelte, H. Stocker, J. Randrup, World Scientific 1997, p. 416.

[35] B. Vulpescu et al., Nucl. Instr. and Meth. A 414 (1998) 205.

[36] A.O. Vaisenberg, Journ. Exptl. Theoret. Phys. 32 (1957) 417.

[37] O.C. Allkofer, J. Trümper, Z. Naturforschg. 19 A (1964) 1304.

[38] T.L. Asatiani et al., Proc. 18th ICRC vol. 7, Bangalore 1983, p. 47.

[39] H. Jones, Rev. Mod. Phys. 11 (1939) 235.

[40] D.F. Smart, M.A. Shea, Proc. 25th ICRC vol. 2, Durban 1997, p. 401.

[41] M. Conversi, Phys. Rev. 79 (1950) 749.

[42] B.G. Owen, J.G. Wilson, Proc. Phys. Soc. (London) A 64 (1951) 417.

[43] J.E.R. Holmes, B.G. Owen, A.L. Rodgers, Proc. Phys. Soc. (London) 78 (1961) 505.

[44] S. Fukui, Journ. Phys. Soc. Jap. 10 (1955) 735.

[45] P.J. Hayman, A.W. Wolfendale, Nature 195 (1962) 166.

[46] C.A. Ayre et al., Proc. 13th ICRC vol. 3, Denver 1973, p. 1754.

[47] D.W. Coates, W.F. Nash, Austral. Journ. Phys. 15 (1962) 420.

[48] B.C. Rastin, S.R. Baber, R.M. Bull, W.F. Nash, Proc. 9th ICRC vol. 2, London 1965, p. 931.

[49] S.R. Baber, W.F. Nash, B.C. Rastin, Nucl. Phys. B 4 (1968) 549.

[50] I.C. Appleton, M.T. Hogue, B.C. Rastin, Nucl. Phys. B 26 (1971) 365.

[51] B.C. Rastin, Journ. Phys. G 10 (1984) 1629.

[52] S. Kawaguchi, T. Sakai, H. Oda, H. Ueno, Y. Kamiya, Proc. 9th ICRC vol. 2, London 1965, p. 941.

[53] N.S. Palmer, W.F. Nash, Canad. Journ. Phys. 46 (1968) S313.

[54] H. Kasha, C.J.B. Hawkins, R.J. Stefanski, Canad. Journ. Phys. 46 (1968) S306.

[55] O.C. Allkofer, R.D. Andresen, Nuovo Cimento B 51 (1967) 329.

[56] O.C. Allkofer, R.D. Andresen, W.D. Dau, Canad. Journ. Phys. 46 (1968) S301.

[57] O.C. Allkofer, K. Clausen, Acta. Phys. Acad. Scien. Hun. 29 Suppl. 2 (1970) 689.

[58] O.C. Allkofer, W.D. Dau, Phys. Lett B 38 (1972) 439.

[59] T.H. Burnett et al., Phys. Rev. Lett. 30 (1973) 937.

[60] B.J. Bateman, N.M. Duller, P.J. Green, A.V. Jelinek, Proc. 13th ICRC vol. 3, Denver 1973, p. 1816.

[61] M.S. Abdel-Monem, J.R. Benbrook, A.R. Osborne, W.R. Sheldon, Proc. 13th ICRC vol. 3, Denver 1973, p. 1811.

[62] C.A. Ayre et al., Proc. 13th ICRC vol. 3, Denver 1973, p. 1822.

[63] K.P. Singhal, Proc. 18th ICRC vol. 7, Bangalore 1983, p. 27.

[64] S.A. Stephens, R.L. Golden, Proc. 20th ICRC vol. 6, Moscow 1987, p. 173.

[65] M. Yamada et al., Phys. Rev. D 44 (1991) 617.

[66] M.P. De Pascale et al., Journ. Geophys. Res. A 98 (1993) 3501.

[67] E. Schneider et al., Proc. 24th ICRC vol. 1, Rome 1995, p. 690.

[68] G. Tarlé et al., Proc. 25th ICRC vol. 6, Durban 1997, p. 321.

[69] J.F. Krizmanic et al., Proc. 24th ICRC vol. 1, Rome 1995, p. 593.

[70] G. Basini et al., Proc. 24th ICRC vol. 1, Rome 1995, p. 585.

[71] T.E. Jannakos, FZKA Report 5520, Forschungszentrum Karlsruhe, 1995.

[72] S. Tsuji et al., Journ. Phys. G 24 (1998) 1805.

[73] D. Heck et al., FZKA Report 6019, Forschungszentrum Karlsruhe, 1998.

[74] GHEISHA: H. Fesefeldt, Report PITHA 85/02, RWTH Aachen, Germany (1985).

[75] VENUS: K. Werner, Phys. Rep. 232 (1993) 87.

[76] J.J. Engelmann et al., Astron. Astrophys. 233 (1990) 96.

[77] G. Barbiellini et al., Proc. 25th ICRC vol. 3, Durban 1997, p. 369.

[78] W. Menn et al., Proc. 25th ICRC vol. 3, Durban 1997, p. 409.

[79] E.S. Seo et al., Nucl. Tracks Radiat. Meas. 20 (1992) 431.

[80] O.C. Allkofer, K. Clausen, W.D. Dau, Nuovo Cimento 12 (1975) 107.

[81] O.C. Allkofer et al., Acta. Phys. Acad. Scien. Hun. 29 Suppl. 4 (1970) 13.

[82] A. Ferrari, P.R. Sala, ATLAS Internal Note, PHYS-No-086, 6 June 1996.

[83] J. Knapp, D. Heck, CORSIKA: A User's Guide (Version 5.61 from April 21, 1998), Forschungszentrum Karlsruhe, Institut für Kernphysik, Germany.

[84] O.G. Ryazhakaya, Nuovo Cimento C 19 (1996) 655; Y. Hirata et al., Phys. Lett. B 335 (1994) 237.

[85] Y. Fukada et al., Phys. Rev. Lett. 81 (1998) 1158.

[86] O.C. Allkofer et al., Journ. Geophys. Res. 90 (1985) 3537.

[87] T.K. Gaisser, Cosmic Rays and Particle Physics, Cambridge University Press 1992, p. 74

[88] O.C. Allkofer et al., Lett. Nuovo Cimento 41 (1984) 373; R.K. Adair, H. Kasha, R.G. Kellog, L.B. Leipuner, R.C. Larsen, Phys. Rev. Lett. 39 (1977) 112.

[89] K.J. Oxford, K.E. Turver, A.B. Walton, Canad. Journ. Phys. 46 (1968) S119.

[90] J.L. Morrison, J.W. Elbert, Proc. 13th ICRC vol. 3, Denver 1973, p. 1833.

[91] A. Goned, M. Shalaby, A.M. Salem, M. Roushdy, Proc. 19th ICRC vol. 8, La Jolla 1985, p. 192.

[92] H.M. Portella, F.M.O. Castro, N. Amato, R.H.C. Maldonado, A. Gomes, Proc. 23rd ICRC vol. 4, Calgary 1993, p. 464.

[93] T.K. Gaisser, T. Stanev, G. Barr, Proc. 20th ICRC vol. 6, Moscow 1987, p. 169.

[94] CERNLIB - CERN Program Library Short Writeups, 1996.

[95] T.H. Burnett et al., Proc. 13th ICRC vol. 3, Denver 1973, p. 1764.

APPENDIX

A. EXAMPLES OF EVENT PATTERNS

The off-line analysis code builds event patterns and different spectra from the raw data and uses a "windows" environment for various operations. This is done by including in a C code a graphical library from the Forms Library V0.86 for Linux platform (SuSE 5.3).

The "FILTER" button eliminates events from displaying which do not fulfil the selection criteria, e.g. figures A.1 to A.8. When the "LOG" button is activated, more information about the ADC and MTDC event structure is presented in a text window (the zero suppressed raw MTDC data). The buttons numbered from 1 to 8 belong to the version of the program adapted for the WILLI-99 experiment and select 1 of 8 time windows displayed at a time (new electronics provides 1024 time channels instead of 256 in the case of WILLI-97 and WILLI-98).

The output of the off-line analysis is organised in the *Hbook* CERN-Library format of *Ntuple* objects for further analysis. For each selected event, information is saved as follows:

- muon stopping layer (1 to 14)
- event class (1 to 8)
- decay time (in channels, 1 to 256)
- information on anti-counters, for further investigation of the background suppression
- event sequential number in the raw data
- date: year, month, day, hour, minute, second (from the local system time of the acquisition computer)
- the ADC values of the 40 anode signals (in channels, 1 to 4096)

The next figures show the single event display window with a discussion of various patterns of detected events. When comparing with similar cases from simulations, a difference is that the Monte-Carlo "detector" gives only one value of the energy deposited in the scintillator, while the real detector combines the two anode signals from the two probes in order to get the deposited energy (the left-right coincidence). Therefore, the missing efficiency of only one of the two probes corresponding to one active module is not implemented in the simulations. Another aspect of the acquisition system is the finite time window sampling the anode pulse in the AMPLITUDE UNIT (see Fig. 3.4 and 3.5 in section 3). This is seen in Fig. A.5 where the secondary particle produces no anode signals as it is delayed out of the ADC sampling period. For the calibration procedure described in section 3.2 and the determination of the thresholds only events in the first part of the decay curve have been considered.

Events shown in figures A.1 to A.8 are eliminated from the analysis, as they do not obey the established criteria. The event patterns in Fig. A.2 and Fig. A.5, although found in simulations too as small electromagnetic showers induced by the decay electron, could be included in the analysis only after a better understanding of the muon "total capture" delayed particles, as discussed in section 2.2. Classes "higher" than 8 have a low contribution to the data set and cannot significantly influence the result. The event in Fig. A.7 could be identified as triggered by muons from an atmospheric shower (approximately parallel tracks). Nevertheless, a better estimation of the incoming direction is necessary to make such a statement. The comment on Fig. A.8 is based on the average position of a minimum ionising particle (MIP) signal in the ADC scale, about 200 channels from 4096 total number of channels. All 4 anti-counters give signal, indicating the lateral extension of the particles.

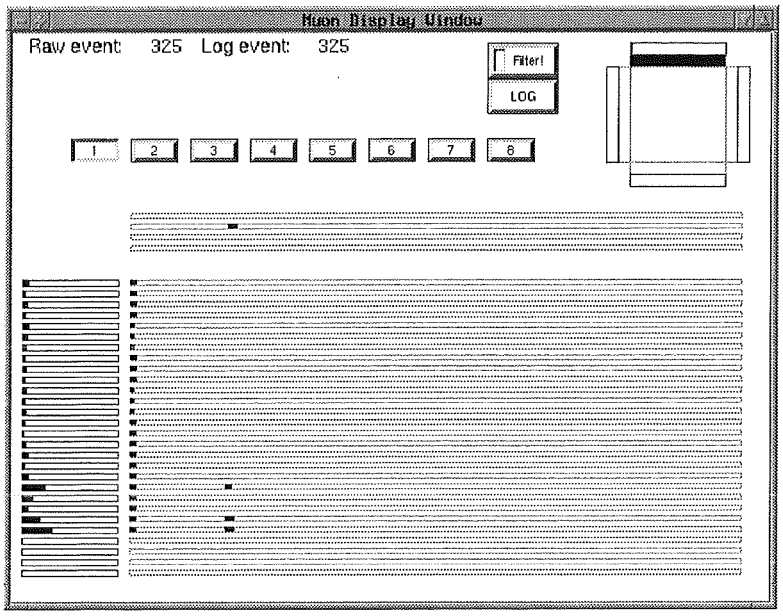

Fig. A.1: The muon track is detected with full efficiency down to the stopping layer, but the electron track is discontinuous and it coincides in time with a signal in one of the anti-coincidence detectors.

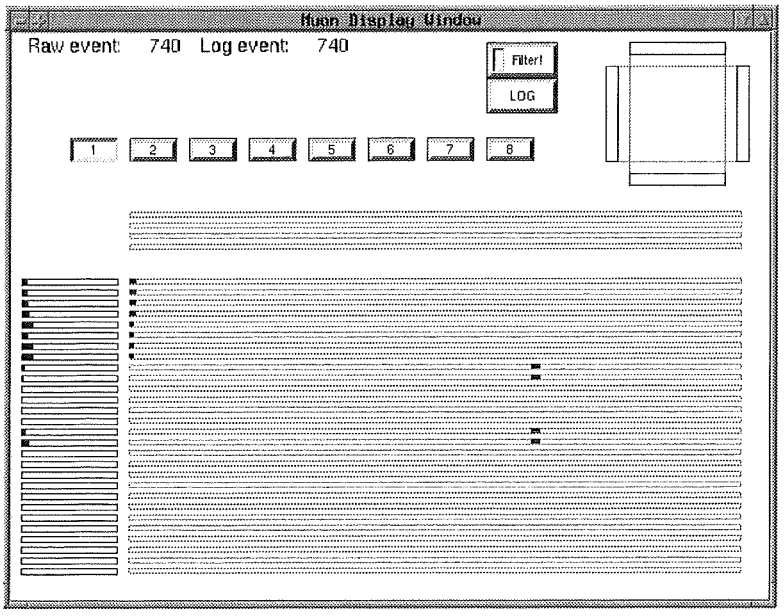

Fig. A.2: The electron track is detected with left-right coincidence in two layers, but there are "empty" layers in between. There is no VETO signal, nevertheless the event is rejected.

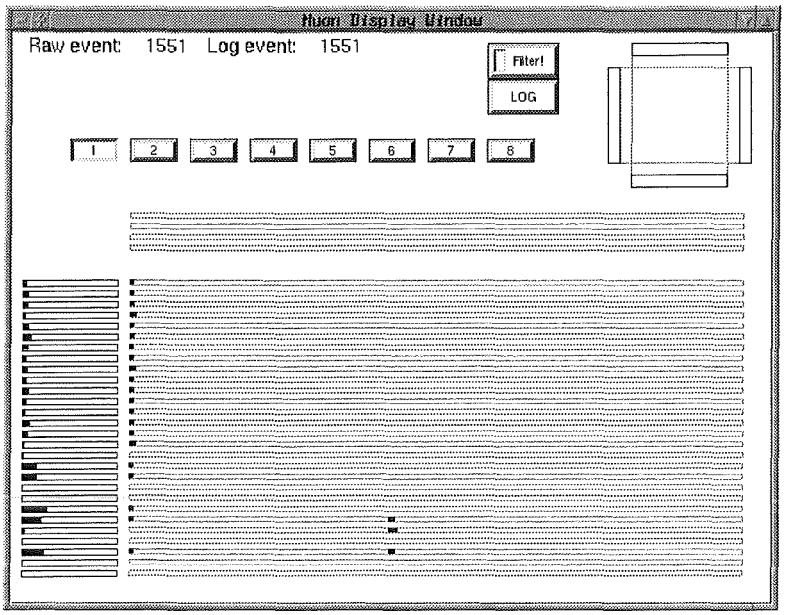

Fig. A.3: No VETO signal; both muon and electron track are discontinuous, most probable a case of missing efficiency.

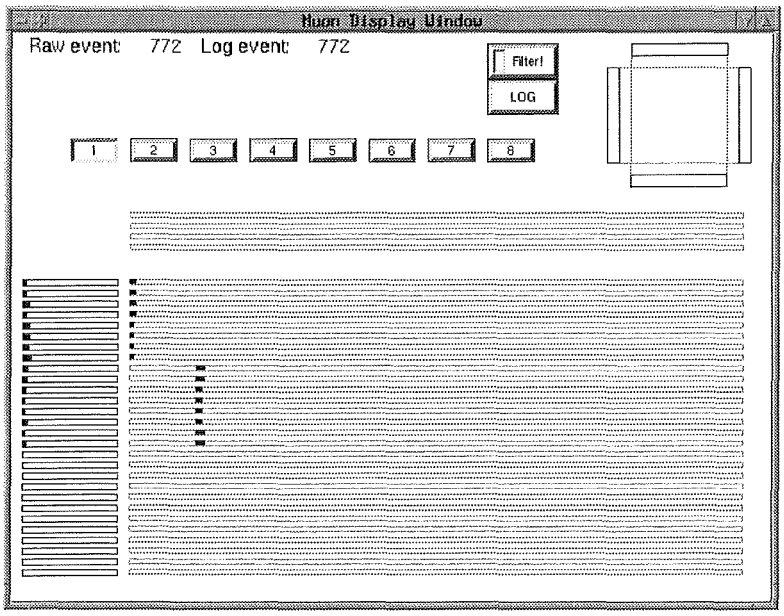

Fig. A.4: Event selected according to the established rules, but not belonging to the most frequent 8 classes considered (the electron track is seen in 4 layers).

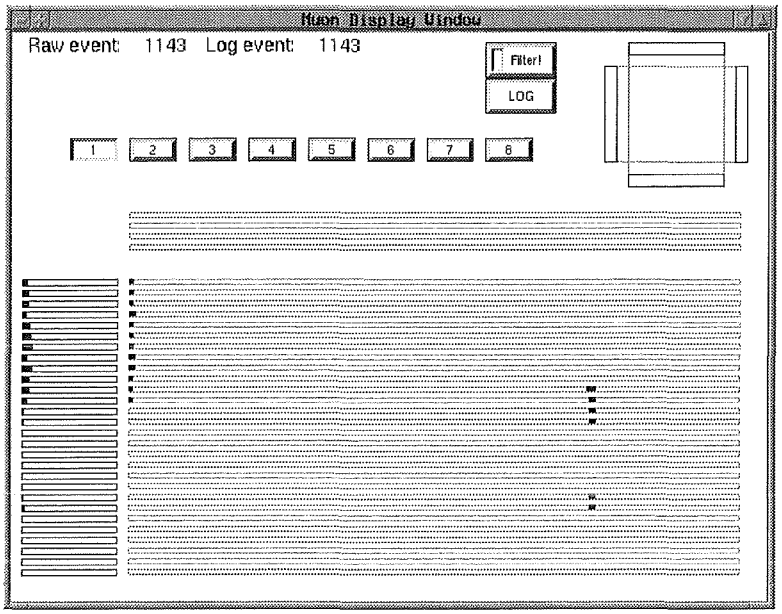

Fig. A.5: A long "electron" track (across 6 layers) can appear from γ- conversion or other products following the muon total capture (section 2.2). Missing efficiency in 3 subsequent layers is less probable.

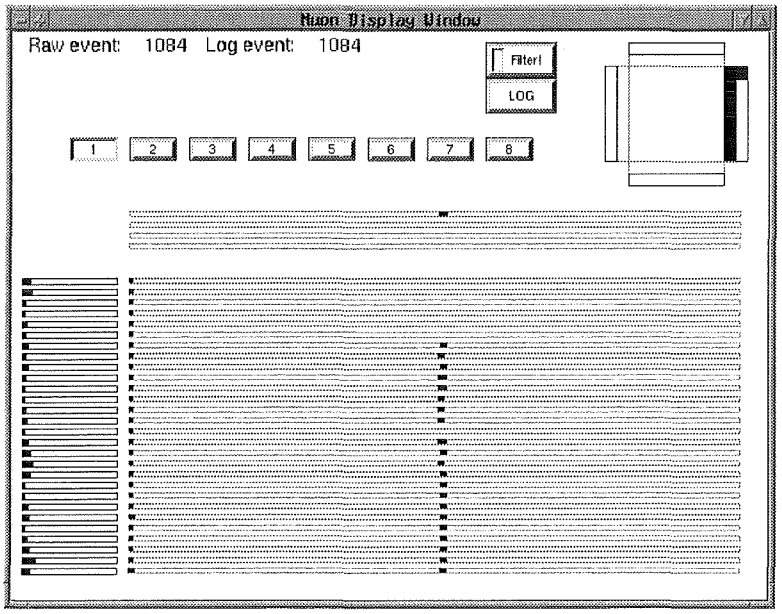

Fig. A.6: The muon triggering the event crosses all 14 layers and a second one penetrates the detector from one side.

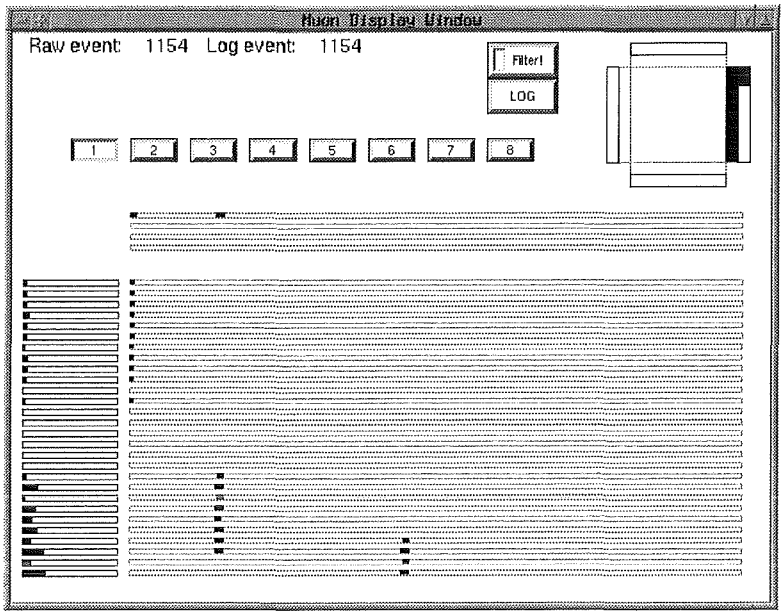

Fig. A.7: Triple coincidence of particles coming from the same direction (two of them cross the same VETO counter), probably muons from a small inclined shower.

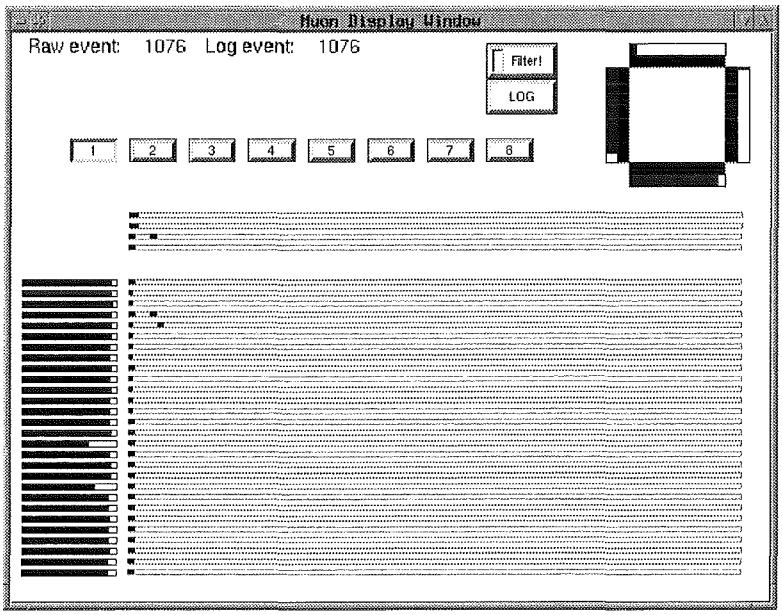

Fig. A.8: Saturation of the ADC signals indicate more than 20 MIP's equivalent, indication of an electromagnetic shower.

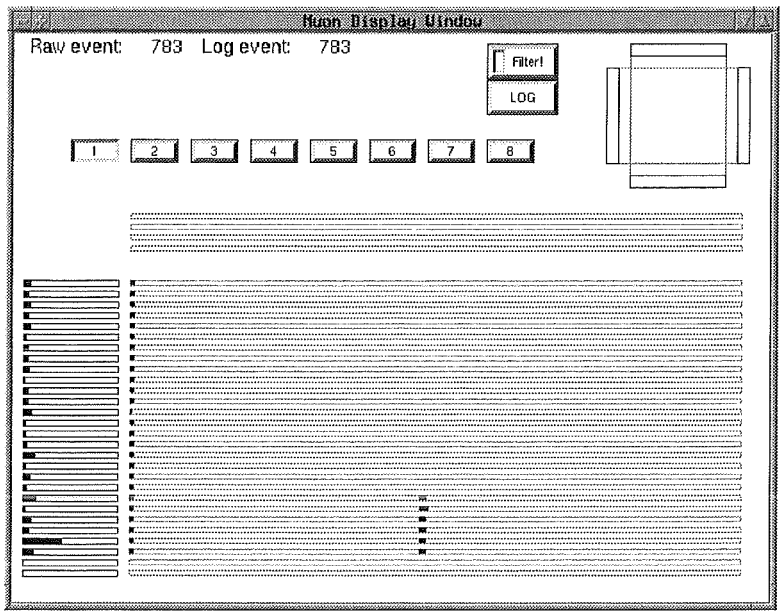

Fig. A.9: Class 6 event. Except a small probability of back-scattering, the electron is emitted upwards.

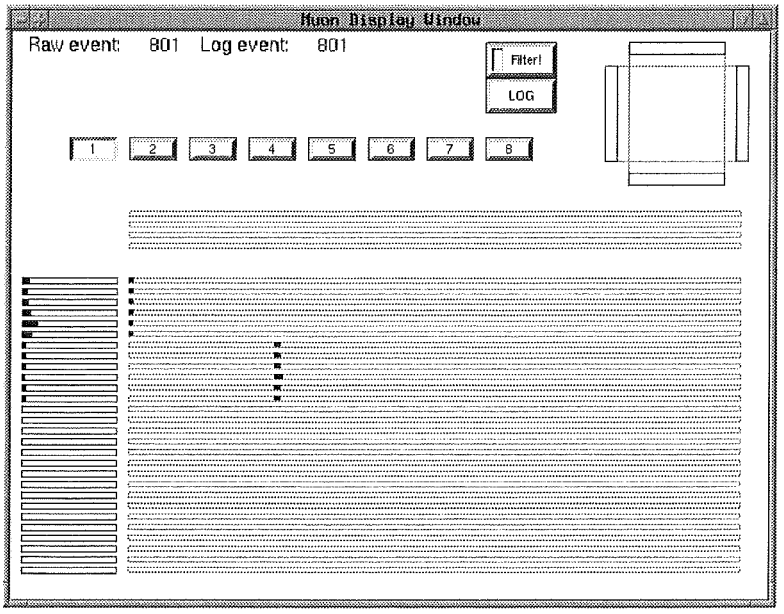

Fig. A.10: Class 8 event where the electron is most probably emitted downwards.

B. COMPILATION OF EXPERIMENTAL RESULTS OF CHARGE RATIO MEASUREMENTS

The tables in this appendix compile the experimental results used in chapter 3.5 to illustrate the actual knowledge on the muon charge ratio. Measurements at mean momentum value below 20 GeV/c have been selected. When only momentum or energy range was specified, the mean momentum value was calculated using the same spectrum as in the detector simulations (see section 3.2). The method is indicated in order to distinguish "delayed coincidences" from magnetic spectrometer experiments.

The geomagnetic cut-off (R_c (for vertical incidence) is calculated by interpolating a two-dimensional grid (latitude and longitude) for the geographical location of the particular experiment [40], except when it was mentioned in the literature source.

Tab. B.1: Measurements of the muon charge ratio R(μ^+/μ^-) in vertical direction at momenta below 20 GeV/c. Method: A - by observing the change in the mean lifetime of negative muons stopped in matter, B - with magnetic spectrometer. R_c is the geomagnetic cutoff at the location of the experiment.

Author Year/Ref.	p_μ [GeV/c]	R (μ^+/μ^-)	Method	R_c [GV]
Conversi 1947/[41]	0.4	1.24 ±0.05	A	6.4
Conversi 1949/[41]	0.35	1.24 ±0.15	A	1.9
Owen 1951/[42]	1.15	1.172±0.019	B	2.9
	1.90	1.241±0.018		
	2.75	1.251±0.018		
	4.90	1.263±0.019		
	6.76	1.240±0.023		
	11.48	1.229±0.036		
Moroney 1954/[11]	0.6	1.14 ±0.07	B	3.0
	1.6	1.20 ±0.07		
	1.7	1.16 ±0.10		
	2.6	1.39 ±0.12		
	3.4	1.28 ±0.08		
	4.3	1.36 ±0.12		
	9.0	1.38 ±0.12		
Fukui 1955/[44]	0.85	0.88 ±0.13	B	12.2
	1.71	1.03 ±0.11		
	3.72	1.27 ±0.14		
	10.	1.27 ±0.15		
Holmes 1961/[43]	6.7	1.39 ±0.08	B	2.9
	11.	1.35 ±0.08		
	18.	1.29 ±0.08		
Hayman 1962/[45]	6.7	1.229±0.049	B	2.1
	10.4	1.223±0.038		
	17.5	1.233±0.037		
Coates 1962/[47]	4.32	1.33 ±0.10	B	2.6
Rastin 1965/[48]	4.3	1.217±0.033	B	2.6

(Continued)

Author Year/Ref.	p_μ [GeV/c]	R (μ^+/μ^-)	Method	R_c [GV]
Allkofer 1968/[56]	0.325	0.98 ±0.13	B	14.1
	0.515	1.25 ±0.13		
	0.71	1.46 ±0.20		
	0.995	1.50 ±0.13		
	1.4	1.20 ±0.12		
	2.42	1.64 ±0.12		
	5.4	1.32 ±0.12		
	13.	0.95 ±0.14		
	19.	1.07 ±0.18		
Baber 1968/[49]	4.0	1.22 ±0.04	B	2.6
	6.1	1.27 ±0.04		
	9.2	1.26 ±0.06		
	12.4	1.25 ±0.08		
	17.1	1.27 ±0.09		
Allkofer 1970/[57]	0.5	1.337±0.098	B	2.3
	1.34	1.469±0.087		
	2.67	1.606±0.130		
	4.57	1.364±0.131		
	8.31	1.275±0.140		
Appleton 1971/[50]	3.8	1.249±0.024	B	2.6
	6.	1.229±0.020		
	9.2	1.256±0.027		
	12.7	1.312±0.039		
	17.2	1.263±0.038		
Allkofer 1972/[58]	0.46	1.17 ±0.11	B	14.1
	0.90	1.43 ±0.10		
	1.60	1.51 ±0.10		
	2.40	1.71 ±0.14		
	3.80	1.36 ±0.10		
	11.40	1.06 ±0.07		
	0.46	1.37 ±0.14		2.3
	0.90	1.41 ±0.10		
	1.60	1.51 ±0.12		
	2.40	1.66 ±0.16		
	3.80	1.53 ±0.14		
	11.40	1.22 ±0.10		

(Continued)

Author Year/Ref.	p_μ [GeV/c]	R (μ^+/μ^-)	Method	R_c [GV]
Abdel-Monem 1973/[61]	3.	1.20 ±0.06	B	4.8
	5.3	1.24 ±0.07		
	8.4	1.26 ±0.11		
	12.1	1.24 ±0.12		
	18.8	1.24 ±0.15		
Ayre 1973/[62]	9.7	1.277±0.008	B	2.1
	11.9	1.252±0.017		
	12.4	1.295±0.007		
	13.6	1.284±0.014		
	13.9	1.286±0.003		
	16.1	1.281±0.016		
	19.6	1.288±0.015		
Burnett 1973/[59]	14.4	1.32 ±0.05	B	5.8
	17.4	1.25 ±0.05		
Singhal 1983/[63]	0.23	1.02 ±0.17	A	15.6
	0.31	1.24 ±0.23		
	0.52	0.99 ±0.17		
	0.74	1.46 ±0.24		
Rastin 1984/[51]	4.48	1.361±0.034	B	2.6
	4.96	1.336±0.026		
	5.37	1.322±0.025		
	5.67	1.336±0.031		
	5.91	1.320±0.028		
	6.18	1.308±0.026		
	6.49	1.302±0.024		
	6.84	1.310±0.023		
	7.24	1.231±0.020		
	7.70	1.271±0.020		
	8.25	1.257±0.019		
	8.91	1.257±0.018		
	9.70	1.249±0.017		
	10.69	1.239±0.016		
	11.94	1.247±0.016		
	13.58	1.251±0.016		
	15.81	1.285±0.016		
	19.05	1.263±0.016		

(Continued)

Author Year/Ref.	p_μ [GeV/c]	R (μ^+/μ^-)	Method	R_c [GV]
Stephens 1987/[64]	0.8	0.97 ±0.06	B	4.9
	0.9	0.95 ±0.05		
	1.0	1.04 ±0.04		
	2.0	1.12 ±0.03		
	3.0	1.18 ±0.03		
	8.0	1.27 ±0.03		
	10.	1.44 ±0.07		
	11.2	1.26 ±0.07		
	13.0	1.17 ±0.06		
	15.3	1.23 ±0.05		
	18.1	1.14 ±0.04		
De Pascale 1993/[66]	0.320	1.207 ±0.130	B	0.7
	0.479	1.233 ±0.088		
	0.643	1.192 ±0.081		
	0.865	1.258 ±0.068		
	1.228	1.218 ±0.057		
	1.948	1.192 ±0.049		
	3.568	1.237 ±0.046		
	8.008	1.185 ±0.047		
Grandegger 1993/[32]	5.1	1.32 ±0.04	A	2.9
Jannakos 1995/[71]	5.1	1.28 ±0.02	A	2.9
Basini 1995/[70]	0.49	1.08 ±0.24	B	4.3
	0.82	1.22 ±0.26		
	1.24	1.13 ±0.18		
Krizmanic 1995/[69]	0.44	1.12 ±0.27	B	0.4
Schneider 1995/[67]	0.59	1.17 ±0.04	B	4.3
Tarlé 1997/[68]	0.59	1.081±0.054	B	0.4
WILLI-97 [35]	0.86	1.30±0.05	A	5.6
WILLI-98 this work	0.52	1.27±0.01	A	5.6

Tab. B.2: Measurements of the muon charge ratio at different zenith angles in the EAST-WEST and NORTH-SOUTH plane.

Author Year/Ref.	θ^o [deg]	p_μ [GeV/c]	R (μ^+/μ^-)	R_c [GV]
Moroney 1954/[11]	30 EAST	0.6	0.93±0.15	3.0
		1.6	1.39±0.22	
		1.7	1.14±0.13	
		2.6	1.09±0.12	
		3.4	1.27±0.19	
		4.3	1.18±0.13	
		9.0	1.40±0.13	
	30 WEST	0.6	1.61±0.25	
		1.6	1.40±0.20	
		1.7	1.44±0.23	
		2.6	1.39±0.20	
		3.4	1.25±0.17	
		4.3	1.19±0.18	
		9.0	1.50±0.21	
	60 EAST	0.6	0.60±0.11	
		1.6	0.97±0.13	
		1.7	0.78±0.13	
		2.6	0.80±0.11	
		3.4	1.12±0.12	
		4.3	0.83±0.10	
		9.0	1.23±0.10	
	60 WEST	0.6	1.90±0.23	
		1.6	1.65±0.18	
		1.7	2.20±0.35	
		2.6	1.70±0.23	
		3.4	1.51±0.12	
		4.3	1.34±0.15	
		9.0	1.29±0.10	

(Continued)

Author Year/Ref.	θ^o [deg]	p_μ [GeV/c]	R (μ^+/μ^-)	R_c [GV]
Judge 1965/[13]	30 EAST	0.84	1.12±0.22	2.6
		1.46	1.08±0.16	
		2.46	1.13±0.22	
		3.87	1.21±0.18	
		5.90	1.29±0.26	
		8.69	1.16±0.24	
		13.51	0.98±0.29	
	45 EAST	0.84	1.05±0.16	
		1.46	1.26±0.16	
		2.46	1.51±0.21	
		3.87	1.22±0.17	
		5.90	1.33±0.25	
		8.69	1.65±0.28	
		13.51	1.32±0.31	
	60 EAST	0.84	1.02±0.18	
		1.46	1.08±0.17	
		2.46	1.28±0.19	
		3.87	1.42±0.18	
		5.90	1.44±0.23	
		8.69	1.26±0.28	
		13.51	1.48±0.27	
Allkofer 1967/[55]	45 EAST	0.3	0.76±0.16	2.3
		0.6	0.82±0.10	
		1.2	0.95±0.09	
		2.4	1.09±0.09	
		6.5	1.14±0.08	
		15.0	1.28±0.18	
	45 WEST	0.3	1.48±0.27	
		0.6	1.51±0.25	
		1.2	1.46±0.16	
		2.4	1.38±0.13	
		6.5	1.20±0.11	
		15.0	1.22±0.21	

(Continued)

Author Year/Ref.	θ^o [deg]	p_μ [GeV/c]	R (μ^+/μ^-)	R_c [GV]
Allkofer 1970/[57]	60 EAST	0.5	0.966±0.147	2.3
		1.34	1.024±0.111	
		2.67	1.233±0.124	
		4.57	1.165±0.114	
		8.31	1.305±0.137	
	60 WEST	0.5	1.718±0.200	
		1.34	1.883±0.159	
		2.67	1.823±0.166	
		4.57	1.843±0.172	
		8.31	1.392±0.153	
Bateman 1973/[60]	65 WEST	2–5	1.43±0.29	4.8
	72.5		3.13±0.63	
	77.5		3.2±0.9	
	82.5		7.7±4.4	
	65	5–10	1.27±0.20	
	72.5		1.38±0.27	
	77.5		2.63±0.51	
	82.5		5.0±1.8	
	65	10–15	1.29±0.12	
	72.5		1.50±0.27	
	77.5		1.55±0.22	
	82.5		2.34±0.47	
	65	15–20	1.18±0.14	
	72.5		1.29±0.30	
	77.5		1.70±0.26	
	82.5		1.95±0.43	
Kawaguchi 1965/[52]	78 NORTH	7.4	1.284±0.094	12.0
		10.6	1.249±0.076	
		15.3	1.312±0.068	
Palmer 1968/[53]	80 NORTH	3.3	1.151±0.078	2.6
		5.2	1.250±0.073	
		7.8	1.203±0.067	
		11.7	1.195±0.063	
		16.5	1.211±0.072	

(Continued)

Author Year/Ref.	θ^o [deg]	p_μ [GeV/c]	R (μ^+/μ^-)	R_c [GV]
Kasha 1968/[54]	75 NORTH	2.0	1.35±0.15	2.1
		6.0	1.29±0.10	
		10.0	1.18±0.11	
		14.2	1.23±0.12	
		18.1	1.12±0.13	

Author Year/Ref.	θ^o [deg]	ϕ^o [deg]	p_μ [GeV/c]	R (μ^+/μ^-)	R_c [GV]
Tsuji 1998/[72]	40	0 SOUTH	2.5–3.5	1.141±0.053	12.1
		45		1.294±0.076	
		90 WEST		1.263±0.075	
		135		1.148±0.067	
		180 NORTH		1.060±0.060	
		225		1.094±0.068	
		270 EAST		1.104±0.067	
		315		1.181±0.072	

C. THE SENSITIVITY OF THE MUON CHARGE RATIO TO THE PRIMARY COSMIC RAY MASS COMPOSITION

Protons and neutrons of the primary radiation interact in the atmosphere producing pions with different charge excess. Therefore a different muon charge ratio results at the ground level. Neutrons in the primary radiation are bound in nuclei, while protons exist as primary flux and bound in nuclei.

Analytical calculations based on solving diffusion equations of particle fluxes in the atmosphere can mathematically illustrate the sensitivity of the muon charge ratio to the neutron fraction in the primary flux [16, 87]. The main ingredients of such a procedure are the spectrum weighted moments of the inclusive cross sections (see [87] p.65) and the mean free path for nucleons, pions and kaons. The boundary condition of a power law primary spectrum of nucleons is considered. The inclusive cross sections and their moments are global quantities that depend on extrapolations and interpolations in regions where no data exist, and they are subject to continuous improvements by new measurements in accelerator experiments. Nevertheless, the mathematical result obtained in the frame of some approximations ([87])

$$\frac{\mu^+}{\mu^-} = \frac{1 + \delta_0 AB}{1 - \delta_0 AB} \tag{C.1}$$

shows the muon charge ratio depending on the relative proton excess on the top of the atmosphere

$$\delta_0 = \frac{p_0 - n_0}{p_0 + n_0} \tag{C.2}$$

and on A and B, which are expressions of the spectrum weighted moments of the inclusive cross sections (p,p), (p,n), (p,π^+) and (p,π^-) – if accounting

muons only from decaying pions:

$$A \equiv (Z_{p\pi^+} - Z_{p\pi^-})/(Z_{p\pi^+} + Z_{p\pi^-})$$

$$B \equiv (1 - Z_{pp} - Z_{pn})/(1 - Z_{pp} + Z_{pn}).$$

For instance, with a power law primary spectrum having an index -2.7 (below the "knee") the moments calculated in [87] are

Z_{pp}	Z_{pn}	$Z_{p\pi^+}$	$Z_{p\pi^-}$
0.263	0.035	0.046	0.033

and the charge ratio of muons is determined only by the fraction of neutrons in the primary radiation. Conversely, if values of 1.27 and 1.30 are considered for the muon charge ratio, relative proton excesses $\delta_0 = 0.80$ and $\delta_0 = 0.87$ are obtained, respectively. In the primary energy range from 10 GeV to 100 GeV

The Monte Carlo calculations of chapter 4 assume a complete superposition and only protons and neutrons are simulated as primary particles. Heavier nuclei (α, C, N, O) are considered as superposition of corresponding contributions of protons and neutrons, according to their abundance in the primary flux. Therefore, the global proton to neutron ratio can be as signature of the mass composition and is directly related to the muon charge ratio. On this basis, Fig. C.1 displays results from CORSIKA simulations (using GHEISHA and VENUS as hadronic interaction models) for the muon charge ratio separately for pure proton primary flux, for alpha flux and for all nuclei considered in the simulations. In the energy range of the simulated primary particles, the relative proton excess, deduced from the direct measured spectra, is $\delta_0 = 0.77$ (see chapter 4).

At higher muon energies (> 100 GeV), the change in the primary mass composition, from proton dominated to an enrichment by heavier nuclei, could be in principle observed. In the primary energy range relevant for this study, the muon charge ratio is a tool for tuning the models of inferring particle fluxes from a primary mass composition known from direct measurements.

Although improved calculations on basis of a more realistic hadronic interaction model are required, the simulation calculations demonstrate that there is a sensitivity of the muon charge ratio to the global neutron to proton ratio in the primary cosmic radiation.

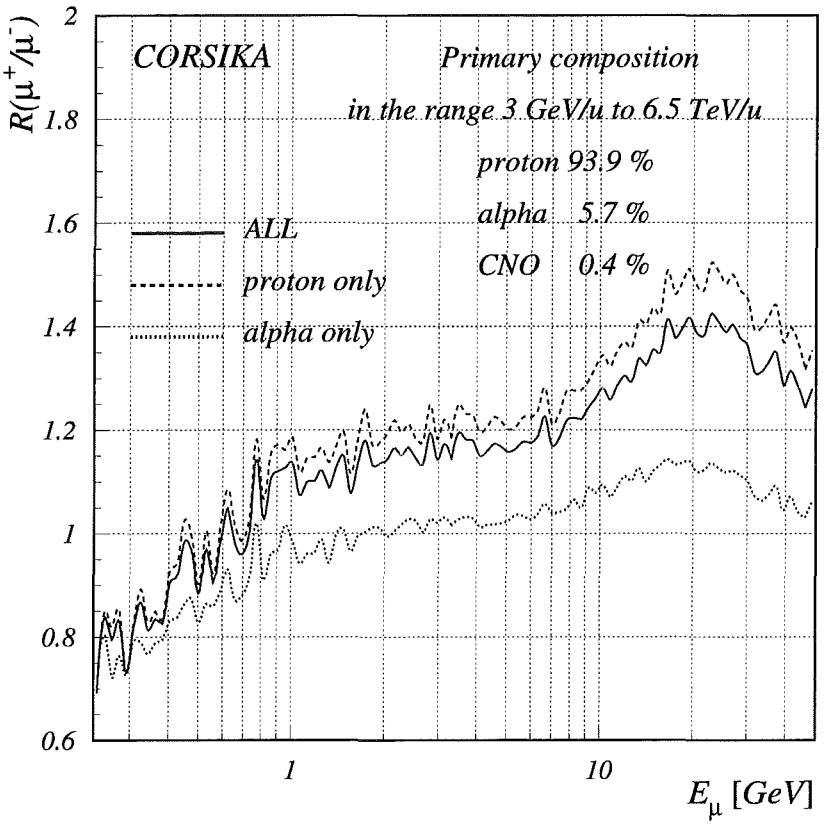

Fig. C.1: Simulation results from CORSIKA (GHEISHA + VENUS) with pure proton primary flux, pure alpha and of the 5 most abundant nuclei (proton, alpha, carbon, nitrogen and oxygen, see chapter 4). The contribution to the primary flux is shown in percent of nuclei and is calculated from the spectra in Fig. 5.1, chapter 4. Carbon, nitrogen and oxygen nuclei have equal numbers of protons and neutrons, therefore the muon charge ratio results with the same value as for alpha particles (as superposition is assumed, thus in the absence of nuclear effects).

Acknowledgements

The experimental basis of these studies has been worked out in the frame of a collaboration of the cosmic ray research groups of NIPNE-HH Bucharest, Romania, and of Institut für Kernphysik III of Forschungszentrum Karlsruhe, Germany. I would like to express my sincere thanks to the leaders of these groups, to Dr. Iliana M. Brâncuş, who kept the dynamics of the Bucharest research group around the WILLI calorimeter, and to Prof. Dr. Heinigerd Rebel for guiding the presented scientific studies along the actual necessities and steering the collaboration project. It is a pleasure to acknowledge particularly the great merits of Dr. Jürgen Wentz in all aspects of the research topic. The setting up of the experimental apparatus and its operation have been done in common work of both groups. I thank DP Florin Badea, Eng. Horia Bozdog, DM Marin Duma, Dr. Andreas Haungs, Dr. Hermann-Josef Mathes and Eng. Mirel Petcu for their expert engagement.

I am grateful to Prof. Dr. Dorin Poenaru for his useful advice in supervising my PhD work, to Prof. Dr. Gerd Schatz for the kind hospitality during various periods as guest scientist in Institut für Kernphysik of Forschungszentrum Karlsruhe. I remember thankfully the encouragement of the late Dr. Valeriu Zoran, former director of NIPNE-HH, who suggested to me to join the field of astrophysical research.

The work has been essentially supported by a WTZ-Project (RUM-14-97), by a grant of the Volkswagenstiftung and by Forschungszentrum Karlsruhe with providing necessary equipment for the WILLI detector.

Finally I thank my wife Laura and my parents for patience and understanding.

Primo vere

Veris leta facies
mundo propinatur,
hiemalis acies
victa iam fugatur.

(Carl Orff - Carmina Burana, Cantiones Profanae)

Spring

The merry face of spring
turns to the world,
sharp winter
now flees, vanquished.